

Information Content of Projections and Reconstruction of Objects in Discrete Tomography

Doctoral Thesis

by

László Varga

Supervisors

Péter Balázs

Antal Nagy

PhD School in Computer Science

Department of Image Processing and Computer Graphics

University of Szeged, Szeged, Hungary

2013

Acknowledgement

I would like to address the first of my acknowledgement to my supervisors, Antal Nagy and Péter Balázs. They did not only help me and guide my research with their advice, but became mentors and friends of mine, to whom I can rely on. I am thankful to László G. Nyúl for our work together and all the thoughts and experience he shared me, and Prof. Dr. Joost Batenburg for his hospitality during my stay at the Centrum Wiskunde & Informatica in Amsterdam. Also, I would like to express my gratitude to Gábor Németh for helping me while I followed his footsteps, and Kálmán Palágyi for always patiently listening to my questions, and answering them. In addition, I would like to thank István Lazányi, Erika Griechisch and László G. Nyúl for proof reading the manuscript, and carefully checking all the comic typos I made.

The research was carried out at the Department of Image Processing and Computer Graphics of the University of Szeged. The work was in part supported by the TÁMOP 4.2.1/B-09/1/KONV-2010-0005 and TÁMOP-4.2.2/B-10/1-2010-0012 projects of the European Union co funded by the European Social Fund, and the OTKA PD100950 grant of the National Scientific Research Fund.

László Varga, May 2013.

Notation and Abbreviation

A, B, C, L	Bold upper case letters: matrices with $a_{i,j}$, $b_{i,j}$, $c_{i,j}$ and $l_{i,j}$ elements
b, x, y	Bold lower case letters: column vectors with b_i , x_i , y_i elements
e	Bold lower case letter e: Vector with all e_i elements equal to 1
0	Bold digit zero: vector with all elements equal to 0
\cdot^T	Transpose of a matrix or vector
$\langle \cdot, \cdot \rangle$	Inner product of two vectors
$\ \cdot \ _2$	Euclidean norm of a vector
$Rank(\mathbf{A})$	Rank of the matrix A
$\lambda_{max}(\mathbf{A})$	Maximal eigenvalue of the matrix A
\mathbb{Z}_{180}	Set of integers modulo 180
$\Phi = \{\phi_0, \phi_1, \dots, \phi_c\}$	Set of pixel intensities with an ordering $\phi_0 < \phi_1 < \dots < \phi_c$
$r_{\mathbf{x}, \mathbf{y}}$	Pearson's correlation coefficient between x and y
$H(z)$	Entropy of the z random variable
$\mathcal{T}_\Phi(\mathbf{x})$	Thresholding of the elements of x vector into the Φ intensity set (see (1.9))
$Random(\Omega)$	Random element of the Ω set with uniform distribution
$S(p, \alpha)$	Equiangular angle set, with p projection count, and α starting angle (see (2.2))
$RME(\mathbf{x}^*, \hat{\mathbf{x}})$	Relative Mean Error [36, 41, 43] of the $\hat{\mathbf{x}}$ reconstruction with the \mathbf{x}^* expected ideal result
$N_4(i)$	4-neighbourhood of the pixel with i index

ARM	Algebraic Reconstruction Method [70, 71]
SIRT	Simultaneous Iterative Reconstruction Technique [70, 71]
TSIRT	Thresholded Simultaneous Iterative Reconstruction Technique
DART	Discrete Algebraic Reconstruction Technique [11, 12]
DC	Reconstruction algorithm based on D.C. programming [55]
SA	Simulated Annealing [50]

List of Figures

1.1	Parameters of a projection line.	6
1.2	Projection of an object.	6
1.3	Illustration of the discretized, pixel-based projection geometry. . . .	8
2.1	Different projection directions with low projection numbers.	17
2.2	Illustration of the equiangular direction sets.	19
2.3	Steps of the <i>Greedy</i> projection selection strategy.	19
2.4	A step of the <i>AltAng</i> angle selection algorithm.	22
2.5	Highlighted phantoms used for testing the direction-dependency. . .	22
2.6	Direction-dependency values of some phantoms with increasing projection numbers.	25
2.7	Minimal and maximal <i>RME</i> values of reconstructions with increasing projection numbers.	26
2.8	Reconstructions of two phantoms from different equiangular sets of their projections.	27
2.9	<i>RME</i> values of reconstructions changing with the starting angle of the projection set.	28
2.10	Accuracy of reconstructions with the four different angle selection strategies.	30
2.11	Reconstructions of a phantom from different equiangular and non-equangular sets of its projections.	31
2.12	Direction-dependency characteristics of a phantom when reconstructed with different reconstruction algorithms.	32
2.13	Correlation between the <i>RME</i> values of reconstructions with different reconstruction algorithms.	34
2.14	Direction-dependency characteristics of an object with different levels of projection noise.	35
2.15	Correlation between the <i>RME</i> values of reconstructions with different reconstruction algorithms.	37
2.16	Altered software phantoms used for testing the direction-dependency.	38
2.17	Direction-dependency characteristics with slightly altered phantoms.	39

2.18	Correspondence between the RME values of reconstructions of the original, and the slightly modified phantom.	39
2.19	Rotation invariant phantom.	40
2.20	Direction-dependency of the rotation invariant phantom.	41
3.1	Illustration of the $g_p(z)$ discretization term of the MLEM algorithm.	47
3.2	Highlighted software phantoms used for testing the MLEM algorithm.	50
3.3	Accuracy diagrams of the DC, DART, and MLEM algorithms.	51
3.4	Binary results of the DC, DART, and MLEM reconstruction algorithms.	53
3.5	Multivalued reconstructions from the DART and MLEM algorithms.	54
3.6	Continuous results of the MLEM algorithm, without the final thresholding.	55
3.7	Accuracy diagrams of the DC, DART, and MLEM algorithms from projections corrupted by random noise.	56
4.1	Highlighted software phantoms used for testing the uncertainty measure.	65
4.2	Probability map examples.	67
4.3	Uncertainty map examples.	68
4.4	Plots of the uncertainty measure and the accuracy of reconstructions with changing projection directions.	71
4.5	Results of the Binary Uncertainty aided DART.	75
4.6	Example of a reconstruction and its uncertainty map.	75
C.1	Binary phantom images (part 1).	87
C.2	Binary phantom images (part 2).	88
C.3	Binary phantom images (part 3).	89
C.4	Multivalued phantom images.	89

List of Tables

2.1	Reconstruction errors from the projection sets of the four angle selection algorithms.	29
2.2	Correlation between the direction-dependencies of the reconstruction algorithms.	33
2.3	Correlation between the direction-dependencies with different distortions of the data.	36
3.1	Reconstruction error and computation time of the DC, DART and MLEM reconstruction algorithms.	52
4.1	Average pixel difference between the probability- and uncertainty-maps given by the two uncertainty measurement methods.	69
4.2	Correlation between the global uncertainty measure and the accuracy of reconstructions.	73
A.1	The connection between the thesis points and the Author's publications.	81
B.1.	A tézispontok és a Szerző publikációinak kapcsolata.	85

Contents

Acknowledgement	iii
Notation and Abbreviation	v
Introduction	1
1 Preliminaries	5
1.1 Formulation of the discrete reconstruction task	5
1.2 Reconstruction algorithms for tomography	9
1.2.1 Discrete Algebraic Reconstruction Technique	10
1.2.2 Simultaneous Iterative Reconstruction Technique	11
1.2.3 Binary reconstruction by energy minimization with D.C. pro- gramming	12
1.3 Tools used for evaluating results	13
1.3.1 Measuring the error of reconstructions	14
1.3.2 Pearson’s correlation coefficient	15
1.4 Modelling measurement errors in the reconstructions	15
2 Direction-Dependency in Discrete Tomography	17
2.1 Introduction	17
2.2 Angle selection strategies	18
2.2.1 Equiangular projection sets	18
2.2.2 Angle insertion by greedy angle testing	19
2.2.3 Altering angles by simulated annealing	20
2.3 Test environment	22
2.3.1 Reconstruction algorithms and parameters	22
2.3.2 Noise on the projection data	23
2.3.3 Implementation	23
2.4 Results	23
2.4.1 Equiangular projection sets	24
2.4.2 Non-equangular projection sets	28
2.4.3 Different reconstruction algorithms	31

2.4.4	Distortion of the projection data	33
2.4.5	Small distortions of the reconstructed objects	38
2.4.6	Rotation invariant images	40
2.5	Possible applications	41
2.6	Summary	43
3	An Energy Minimization Reconstruction Algorithm for Multivalued Discrete Tomography	45
3.1	Introduction	45
3.2	The proposed method	46
3.2.1	The energy function	46
3.2.2	The optimization process	47
3.3	Experimental results	50
3.4	Summary	57
4	Local and Global Uncertainty in Binary Reconstructions	59
4.1	Introduction	59
4.2	The uncertainty problem	59
4.3	Approximating local uncertainty in binary reconstructions	61
4.4	Validation of the results	63
4.4.1	Stochastic approximation of pixel uncertainties	63
4.4.2	Test environment	65
4.5	Results for local uncertainties	66
4.6	Measuring global uncertainty of binary reconstructions	69
4.6.1	Compared reconstruction algorithms	70
4.6.2	Test data	70
4.6.3	Results	71
4.7	Possible applications	72
4.7.1	Using the local uncertainty map in DART reconstructions	72
4.7.2	Verifying the results of reconstructions	74
4.7.3	Blueprint-based projection selection	75
4.8	Summary	76
5	Final Conclusions	77
	Appendices	79
	Appendix A Summary in English	79
	Appendix B Summary in Hungarian	83
	Appendix C Full database of the phantom images	87

Introduction

Tomography is a technique for discovering (or reconstructing) the inner structure of objects from their *projections*, without the destruction of the objects themselves. It is a widely used tool in various applications, like medical diagnostics [36, 43], crystallography [1], non-destructive testing of materials [16, 20, 40], geology, etc. [26].

In *transmission tomography* [33, 39] a *projection* is taken by exposing the object of study to some penetrating radiation on one side, and measuring the energy of the transmitted beams at different points on the other side. In this way, one can calculate the attenuation of the energy of the radiation, and deduce the absorption properties of the object on the paths of the beams. If the projections are gathered from a sufficient number of directions (which might mean hundreds of projections), one can reconstruct the material properties at different parts of the object.

Discrete Tomography [34, 35] is a special case, where we assume that the examined object consists of only a few materials with known absorption coefficients. This extra information can be used to drastically reduce the number of projections required for the reconstructions, and by this to minimize the cost or unwanted effects of the projection acquisition process. Moreover, in *Binary Tomography* we assume that the object is made of a single homogeneous material.

This thesis is a summary of the Author's research in the field of discrete tomography. The central concept of this work was to examine the information content of projections, and to study what kind of information is stored in the projection data and how this information determines the reconstruction of objects. This examination of the information content of projections is useful for developing more reliable and robust methods for discrete tomography, and can lead to entirely new approaches to the reconstruction problem.

The structure of the dissertation is as follows. First, Chapter 1 gives some preliminary knowledge that will later be needed for the description of the results. This chapter does not contain any new contribution, but summarizes the previous results of the field, describes the formulation later used in the thesis, and provides some mathematical tools which will be essential for the evaluation of the results.

Then, Chapters 2, 3 and 4 give a detailed description of the results. Each

chapter will hold findings of one thesis point of the dissertation. Although the results are connected, the chapters are written to be self contained, therefore, each of them is understandable without the other thesis points. In case of the dependence, a summary of the most important knowledge and a reference to the other chapters will be given.

Starting the sequence of the new contributions, Chapter 2 examines the direction-dependency problem arising in the field of Binary Tomography. In a previous work [52], it was briefly shown that the accuracy of the reconstruction can rely on the directions to take projections with, when only a few projections are available. For a more exhaustive investigation of the phenomena, we implemented an experimental test environment, and examined various aspects of this problem. We found that projections of an object taken from different directions can carry entirely different information content. This phenomenon also affects the accuracy of the reconstructions, and some projection sets can lead to much better reconstructions than others. Furthermore, we showed that one can improve the accuracy of the reconstruction only by choosing better directions for the projection acquisition and proposed new projection selection strategies, which can be used in practical applications of Non-Destructive Testing of industrial parts, when a blueprint of the examined object is also available.

Building the test environment for the direction-dependency problem required the examination and implementation of various reconstruction algorithms. Based on this experience, we developed a new reconstruction algorithm that is described in Chapter 3. This algorithm performs the reconstruction as an energy minimization task. An energy function was designed, that formulates the discrete reconstruction problem, and a deterministic energy minimization process was developed, that is capable of giving a good approximation of the optimal solution of the energy function. The method was validated in a set of experimental tests by comparing its performance to other reconstruction algorithms from the literature.

Also, based on previous experience we noticed that in many cases of discrete tomography, some parts of the reconstructions are highly accurate, while reconstruction algorithms tend to miss other parts. This indicated, that the information contained in the projections determines the different areas of the object to different levels. Some parts are well determined by the projections, and can be reliably reconstructed, while other areas are more uncertain due to the lack of information. In Chapter 4, we give a new description of this phenomena in binary tomography, and based on the algorithm of Chapter 3, we propose a method that can approximate the local uncertainties of the reconstructions, i.e., it can reveal how reliable each part of the reconstruction will be based on the projection data. In addition, we provide a formula for combining the local uncertainties into a global measure,

that can describe and grade the information content of the whole projection set. This method was validated in set of experimental tests as well. Finally, we give some possible applications, where the usage of the uncertainty measures can help to determine the reliability of a reconstruction, to improve the projection acquisition process, or to improve the performance of certain reconstruction algorithms.

Chapter 1

Preliminaries

1.1 Formulation of the discrete reconstruction task

In the dissertation, the described methods and results will be presented for the two-dimensional case of discrete tomography. However, the methodology can be extended to higher dimensions in a simple and straightforward way.

Assume, that there is a given object with an unknown interior structure to reconstruct. The attenuation coefficients of the material in a two-dimensional cross-section of this unknown object are represented by the $f : \mathbb{R}^2 \mapsto \mathbb{R}$ function. The projections of the unknown f are given by the *Radon-transform* as line integrals of f

$$[\mathcal{R}f](\alpha, t) = \int_{-\infty}^{\infty} f(t \cos(\alpha) - q \sin(\alpha), t \sin(\alpha) + q \cos(\alpha)) dq . \quad (1.1)$$

In (1.1), an (α, t) pair determines a line in the two dimensional space, by giving its direction and distance from the origin respectively, and q is the parameter for positioning on the line. The parameters of the projection lines are illustrated in Figure 1.1. We use a parallel beam projection geometry, where a projection is defined by a set of line integrals taken with the same α angle. An example of a projection is given in Figure 1.2.

With the above formalism, the mathematical description of the reconstruction problem can be defined as follows.

Problem: RECONSTRUCTION

Input: A set $\Theta \subseteq ([0^\circ, 180^\circ) \times \mathbb{R})$ of parameters determining projection lines, and $[\mathcal{R}f](\alpha, t)$ projection values for each $(\alpha, t) \in \Theta$.

Task: Find an $f' : \mathbb{R}^2 \mapsto \mathbb{R}$ such that $[\mathcal{R}f'](\alpha, t) = [\mathcal{R}f](\alpha, t)$ for each $(\alpha, t) \in \Theta$.

Conversely, given a set of measured projection values, the task is to find a function that has the desired projections. Mathematically, this problem has a

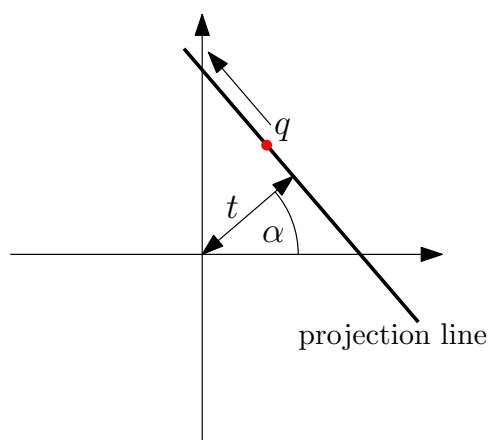


Figure 1.1: Illustration of the parameters of a projection line.

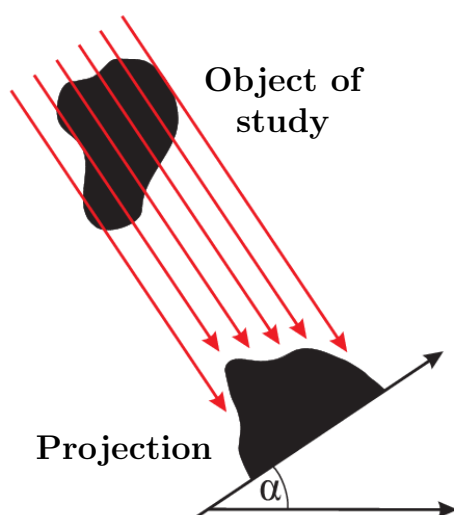


Figure 1.2: Illustration of a projection of an object.

unique solution, and the Radon-transform of any f function is invertible if all the possible projection values are available, i.e., $\Theta = ([0^\circ, 180^\circ) \times \mathbb{R})$ [69].

However, in practice one cannot apply the theoretical inversion formula directly, and in a computerized context a simplification of the model is necessary. We will use a discretized, grid based model for reconstructing finitely many values which can be handled computationally. Also, one can only gain a limited number of projection values to reconstruct the object from.

In the sequel, we will assume that the function f has a bounded support, i.e.,

$$f(u, v) = 0, \quad (u, v) \notin \left[-\frac{n}{2}, \frac{n}{2}\right)^2 \quad (1.2)$$

for a proper n constant. We will also assume, that f takes a constant value on each unit square-shaped area determined by the two-dimensional integer lattice, that is

$$f(u + a, v + b) = f(u + c, v + d), \quad \forall u, v \in \mathbb{Z}, \quad \forall a, b, c, d \in [0, 1). \quad (1.3)$$

This way, the problem is transformed to the reconstruction of an n by n sized image. Note, that with this definition the pixels cover the whole $n \times n$ sized reconstructed area without overlapping.

In addition, we will also assume that the projections consist of a finite set of parallel projection lines placed at uniform distances from each other, and from any direction the whole width of the image is covered by the projection lines. Using (1.1), this is maintained by the choice

$$t \in \left\{ k + 1/2 \mid k \in \mathbb{Z}, \quad \frac{-n}{\sqrt{2}} \leq (k + 1/2) < \frac{n}{\sqrt{2}} \right\}. \quad (1.4)$$

This way one can maintain a projection geometry, where all the pixels are covered by projection lines from any possible directions, and there are no projection lines which run at borders of neighbouring pixels.

Using this finite grid-based model given with all the above restrictions, the reconstruction problem can be reformulated as a system of linear equations

$$\mathbf{Ax} = \mathbf{b}, \quad \mathbf{A} \in \mathbb{R}^{m \times n^2}, \quad \mathbf{x} \in \mathbb{R}^{n^2}, \quad \mathbf{b} \in \mathbb{R}^m, \quad (1.5)$$

where

- \mathbf{x} is the vector of all n^2 unknown image pixels,
- \mathbf{b} is the vector of all m measured projection values,
- \mathbf{A} describes the projection geometry with all $a_{j,i}$ elements giving the length of the line segment of the j -th projection line through the i -th pixel

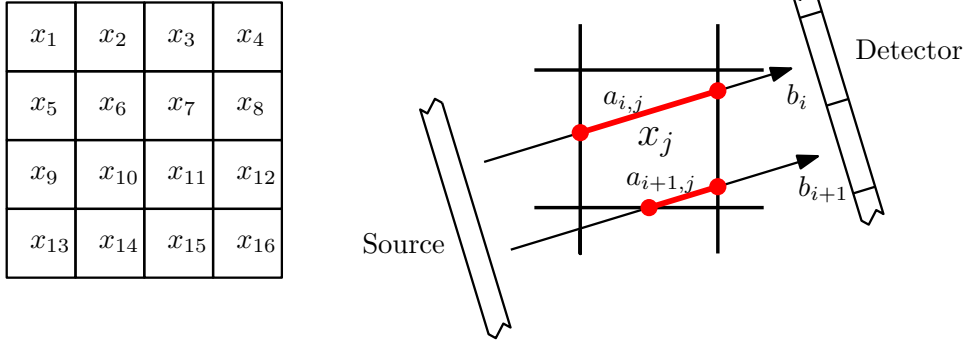


Figure 1.3: Representation of the ordering of the pixels and the parallel beam geometry.

as illustrated in Figure 1.3. From this reformulation, a new grid based version of the reconstruction problem can be defined, that will be referred to as CONTINUOUS RECONSTRUCTION.

Problem: CONTINUOUS RECONSTRUCTION

Input: $\mathbf{A} \in \mathbb{R}^{m \times n^2}$ projection coefficient matrix, and $\mathbf{b} \in \mathbb{R}^m$ vector of projection values.

Task: Find an $\mathbf{x} \in \mathbb{R}^{n^2}$ reconstruction such that $\mathbf{Ax} = \mathbf{b}$.

In case of discrete tomography a new restriction can be made, and we can assume that the reconstructed pixels can only take values from a $\Phi = \{\phi_0, \dots, \phi_c\}$ finite set of intensities.

Problem: DISCRETE RECONSTRUCTION

Input: $\mathbf{A} \in \mathcal{R}^{m \times n^2}$ projection coefficient matrix, $\mathbf{b} \in \mathcal{R}^m$ vector of projection values, and $\Phi = \{\phi_0, \dots, \phi_c\}$.

Task: Find an $\mathbf{x} \in \Phi^{n^2}$ discrete reconstruction such that $\mathbf{Ax} = \mathbf{b}$.

In the DISCRETE RECONSTRUCTION problem, we will also assume that there is an ordering between elements of the Φ set of intensities, and $\phi_0 < \phi_1 < \dots < \phi_c$. Also, without the loss of generality, we can make the restriction that the possible intensities are between 0, and 1, i.e.,

$$\phi_i \in [0, 1], \quad \forall i \in \{0, \dots, c\}. \quad (1.6)$$

and their range is stretched to fill the whole $[0, 1]$ interval

$$\phi_0 = 0, \quad \phi_c = 1. \quad (1.7)$$

Finally, note that as a special case, with the $\Phi = \{0, 1\}$ choice, we arrive to the problem of BINARY RECONSTRUCTION.

Problem: BINARY RECONSTRUCTION

Input: $\mathbf{A} \in \mathcal{R}^{m \times n^2}$ projection coefficient matrix, and $\mathbf{b} \in \mathcal{R}^m$ vector of projection values.

Task: Find an $\mathbf{x} \in \{0, 1\}^{n^2}$ binary reconstruction such that $\mathbf{Ax} = \mathbf{b}$.

1.2 Reconstruction algorithms for tomography

With the above formalism, a computerized reconstruction method has to solve the CONTINUOUS RECONSTRUCTION or the DISCRETE RECONSTRUCTION problem. Various techniques have been proposed for such purposes.

Theoretically, the CONTINUOUS RECONSTRUCTION problem has a unique solution if and only if

$$\text{Rank}(\mathbf{A}) = n^2 = m, \quad (1.8)$$

i.e., if the equation system is consistent, and the \mathbf{A} matrix is invertible. Unfortunately, in many applications this is not the case. It is possible, that the conditions of the projection acquisition process do not allow us to make enough projections that determine the result. In this case, there will be a continuum number of solutions on a hyperplane of $(n^2 - \text{Rank}(\mathbf{A}))$ dimensions.

On the other hand, most projection acquisition methods are not perfect, and the measured projection values can be distorted by measurement errors, which can lead to an inconsistent equation system. In this case, there might not be any feasible solutions at all, or even if there is a solution, it might not be the desired picture of the examined object.

Finally, if we try to solve the equation system (1.5) we will notice, that it has a huge extension since it holds as much variables as the number of pixels on the reconstructed image. Although the \mathbf{A} matrix is extremely sparse, and can be computationally handled, its inverse is likely to hold too many entries to be stored in a reasonably-sized memory. Therefore, direct equation system solvers are mostly not applicable.

Various techniques have been proposed to overcome the above problems, most of which apply iterative processes for approximating the solution of the equation system [3, 37, 57, 58, 70, 71]. These methods can cope with the large number of equations and variables, and can maintain a solution even if it is not unique, or approximate an auxiliary result if the system of equations is inconsistent.

On the other hand, the DISCRETE RECONSTRUCTION problem – and many subclasses as well – is proved to be NP hard if the number of projections is more than two [29]. Also, because of the large size of the problem one cannot hope to gain exact solutions with efficient algorithms.

To overcome the complexity problem different approaches have been examined in the field. Some of them study non-NP-hard subclasses of the reconstruction problem, and provide efficient methods for these special cases [4, 18, 23, 24, 42]. Another area of research concentrates on designing heuristic methods for giving approximate solutions of the general DISCRETE RECONSTRUCTION problem, with different approaches. Some techniques introduce post-processing steps for the discretization of the result of a continuous reconstruction algorithm [13, 14, 15]. Other approaches introduce steering mechanisms into the process of continuous reconstruction methods to gain discrete results [11, 12, 19, 32, 48], or reformulate the problem as an energy minimization task, and approximate the solution with some stochastic [6, 7, 8, 16, 30, 41, 51, 52, 68], or deterministic [44, 45, 55, 56, 67, 68] optimization strategy.

Moreover, the difficulties described at the CONTINUOUS RECONSTRUCTION problem – i.e., the possible inconsistency of the projections, and the non-uniqueness of the results – can still be present in the discrete case, which makes an even bigger need for approximate solutions capable of handling inconsistent and incomplete projection data. In the following, we will describe some of these reconstruction algorithms, which will be used for validation and comparison purposes later in Chapters 2, 3, and 4.

In the algorithms, the *Thresholding* operation [31] of an \mathbf{x} vector of image pixels, to the $\Phi = \{\phi_0, \dots, \phi_c\}$ intensity set will be defined as

$$(\mathcal{T}_\Phi(\mathbf{x}))_i = \begin{cases} \phi_0, & \text{if } x_i < (\phi_0 + \phi_1)/2, \\ \phi_j, & \text{if } (\phi_{j-1} + \phi_j)/2 \leq x_i < (\phi_j + \phi_{j+1})/2, \quad j \in \{2, \dots, c-1\} \\ \phi_c, & \text{if } (\phi_{c-1} + \phi_c)/2 \leq x_i. \end{cases} \quad (1.9)$$

1.2.1 Discrete Algebraic Reconstruction Technique

The Discrete Algebraic Reconstruction Technique (DART) [11], is a method for the general case of the DISCRETE RECONSTRUCTION problem, that is based on an iterated thresholding of continuous reconstructions. This algorithm starts out by producing a continuous reconstruction using an algebraic reconstruction method [70, 71]. Then, in each iteration it applies a thresholding on the continuous result, and proceeds with another continuous reconstruction, performed only on the boundary pixels of the thresholded image. In this way, the process gains a fast but not highly accurate initial solution with a thresholding of a continuous reconstruction, and slowly transforms the object boundary to reach a highly accurate result. The formal description of the algorithm is given in Algorithm 1.

Note, that the algebraic reconstruction method used for obtaining the con-

Algorithm 1 Discrete Algebraic Reconstruction Technique

Input: \mathbf{A} projection matrix; \mathbf{b} expected projection values; $\mathbf{x}^{(0)}$ initial solution; Φ set of possible intensities; k_Δ iteration window size of the stopping criteria; k_{max} maximal iteration count

- 1: Compute a starting reconstruction $\mathbf{x}^{(0)}$ using an algebraic reconstruction method
- 2: $k \leftarrow 0$
- 3: **repeat**
- 4: $k \leftarrow k + 1$
- 5: Compute a segmented image $\mathbf{s}^{(k)} = \mathcal{T}_\Phi(\mathbf{x}^{(k-1)})$ by thresholding $\mathbf{x}^{(k-1)}$
- 6: Compute $I^{(k)}$ set of non-boundary pixels of $\mathbf{s}^{(k)}$
- 7: **for all** $i \in 1, \dots, n^2$ **do**
- 8: $y_i^{(k)} \leftarrow \begin{cases} s_i^{(k)}, & \text{if } i \in I^{(k)} , \\ x_i^{(k-1)}, & \text{otherwise .} \end{cases}$
- 9: **end for**
- 10: Using $\mathbf{y}^{(k)}$ as starting solution, compute a continuous reconstruction $\mathbf{x}^{(k)}$ while keeping the pixels in $I^{(k)}$ fixed
- 11: Apply a smoothing operation to the pixels that are not in $I^{(k)}$
- 12: **until** $\mathbf{s}^{(k)} = \mathbf{s}^{(k-k_\Delta)}$ or $k > k_{max}$
- 13: **return** the segmented image $\mathcal{T}_\Phi(\mathbf{x}^{(k)})$

tinuous reconstructions, and the smoothing operation between the iterations are parameters of the algorithm, which will be defined later with the context of usage.

1.2.2 Simultaneous Iterative Reconstruction Technique

As mentioned above there is a wide range of *Algebraic Reconstruction Methods* (ARM) [3, 70, 71] for continuous reconstruction. One such algorithm is the Simultaneous Iterative Reconstruction Technique (SIRT) [57, 70, 71]. It is an iterative process for solving the linear equation system formulating the CONTINUOUS RECONSTRUCTION problem. Basically, the process of the SIRT starts with an initial starting guess. Then, iteratively in each step it produces the projections of the current intermediate solution, calculates their difference from the expected projections, and updates the pixel values based on the back-projected errors of the projections. With the notation of Section 1.1, the formal description of this method is given in Algorithm 2.

We will also use the thresholded variant of this method that is Algorithm 2 followed by a thresholding, and call this as Thresholded Simultaneous Iterative Reconstruction Technique (TSIRT).

Algorithm 2 Simultaneous Iterative Reconstruction Technique

Input: \mathbf{A} projection matrix; \mathbf{b} expected projection values; $\mathbf{x}^{(0)}$ initial solution; ϵ step size bound; k_{max} maximal iteration count

```

1:  $k \leftarrow 0$ 
2: repeat
3:    $\mathbf{v}^{(k)} \leftarrow (\mathbf{A}\mathbf{x}^{(k)} - \mathbf{b})$ 
4:   for all  $i \in 1, \dots, n^2$  do
5:      $x_i^{(k+1)} \leftarrow x_i^{(k)} - \frac{1}{\sum_{j=1}^m a_{ji}} \sum_{j=1}^m \frac{a_{ji}v_j^{(k)}}{\sum_{l=1}^n a_{jl}}$ 
6:   end for
7:    $k \leftarrow k + 1$ 
8: until  $\|\mathbf{x}^{(k+1)} - \mathbf{x}^{(k)}\|_2^2 < \epsilon$  or  $k > k_{max}$ 
9: return  $\mathbf{x}^{(k)}$ 

```

1.2.3 Binary reconstruction by energy minimization with D.C. programming

The algorithm described in [55] performs the binary reconstruction by reformulating the task into an optimization problem. It is based on minimizing an energy function of the form

$$\mathcal{J}_{\gamma, \mu}(\mathbf{x}) = \frac{1}{2} \|\mathbf{Ax} - \mathbf{b}\|_2^2 + \frac{\gamma}{2} \sum_{i=1}^{n^2} \sum_{j \in N_4(i)} (x_i - x_j)^2 - \mu \frac{1}{2} \langle \mathbf{x}, \mathbf{x} - \mathbf{e} \rangle, \quad \mathbf{x} \in [0, 1]^{n^2}, \quad (1.10)$$

that is a formulation of the DISCRETE RECONSTRUCTION problem.

This function is constructed of three terms. The first $\|\mathbf{Ax} - \mathbf{b}\|_2^2$ term of (1.10) is a so called *projection correctness term*, and takes its minima at the reconstructions satisfying the projections. If the equation system is consistent, the $\|\mathbf{Ax} - \mathbf{b}\|_2^2$ will take a value of 0 at the correct solutions. If the consistency is not maintained due to some measurement errors, then solutions providing the smallest square error will give minimal values.

The second term, with $N_4(i)$ denoting the set of pixels 4-adjacent to the i -th pixel, is a smoothness prior aimed to steer the reconstructions to somewhat smooth results containing compact regions. It is multiplied with a constant γ that can be used to set the weight of this smoothness prior.

The third term stands for forcing binary results, and takes its minima at binary values of $\mathbf{x} \in \{0, 1\}^{n^2}$. It is also weighted with a μ parameter that controls the strength of the binarity prior. With the right μ weight, the $\mathcal{J}_{\gamma, \mu}(\mathbf{x})$ function gives a faithful formalization of the DISCRETE RECONSTRUCTION problem. It can be proved that for each \mathbf{A} , \mathbf{b} , and γ values there exists a μ^* bound such that

minimizing the energy function (1.10) with a $\mu \geq \mu^*$, is equivalent to minimizing

$$\mathcal{K}(\mathbf{x}) := \frac{1}{2} \|\mathbf{A}\mathbf{x} - \mathbf{b}\|_2^2 + \frac{\gamma}{2} \sum_{i=1}^{n^2} \sum_{j \in N_4(i)} (x_i - x_j)^2, \quad \mathbf{x} \in \{0, 1\}^{n^2}, \quad (1.11)$$

that is the DISCRETE RECONSTRUCTION problem in the $\Phi = \{0, 1\}$ binary case, with an additional smoothness prior.

The reconstruction algorithm in [55] applies D.C. programming [38] (a method for minimizing the difference of convex functions) to find an approximate solution of (1.10). We will refer to this algorithm as DC.

Informally, the concept of this algorithm is as follows. At the beginning of the optimization process, the discretizing term is disabled by setting the parameter $\mu = 0$. In that way, we get to a convex (moreover quadratic) optimization problem, that can easily be solved with a subgradient method [17, 22]. After finding the first initial continuous solution, we iteratively start to increase the μ weight and in each iteration we find an approximate solution of the resulting energy function starting from the result of the previous iteration step. At the end – when the strength of the discretizing term reaches the $\mu \geq \mu^*$ limit – we arrive to a discrete result, that is an approximate solution of the original problem.

In the formal description of this algorithm, we will change the form of the smoothness term, and define a matrix \mathbf{L} , such that

$$\mathbf{x}^T \mathbf{L} \mathbf{x} = \sum_{i=1}^{n^2} \sum_{j \in N_4(i)} (x_i - x_j)^2. \quad (1.12)$$

Furthermore, $\lambda_{max}(\mathbf{A}^T \mathbf{A} + \gamma \mathbf{L})$ denotes an upper bound of the $(\mathbf{A}^T \mathbf{A} + \gamma \mathbf{L})$ matrix. The pseudo-code of the process is given in Algorithm 3.

1.3 Tools used for evaluating results

In this section, we will describe some numerical tools which will be used later in the thesis for evaluating the robustness of reconstruction algorithms, and comparing the different methods.

A common approach of evaluating the accuracy of an algorithm is to perform reconstructions of objects with known ground truth expected result. An easy way to do this is to take a set of software phantoms, simulate their projections computationally, and perform reconstructions from the simulated projection sets. For such evaluations one needs a set of software phantoms and a numeric measurement of the reconstruction error.

Algorithm 3 Reconstruction by D.C. programming.

Input: \mathbf{A} projection matrix; \mathbf{b} expected projection values; $\mathbf{x}^{(0)}$ initial state; μ_Δ strengthening step of the binarizing term; γ weight of the smoothness term; ϵ_{in} , ϵ_{out} stopping criteria

```

1:  $\mu \leftarrow 0$ 
2:  $\lambda \leftarrow \lambda_{max}(\mathbf{A}^T \mathbf{A} + \gamma \mathbf{L})$ 
3: repeat
4:   repeat
5:      $\hat{\mathbf{x}} = \mathbf{x}$ 
6:      $\mathbf{y} \leftarrow [(\lambda + \mu)\mathbf{I} - (\mathbf{A}^T \mathbf{A} + \gamma \mathbf{L})]\mathbf{x} - (\frac{1}{2}\mu\mathbf{e} - \mathbf{A}^T \mathbf{b})$ 
7:      $x_i \leftarrow \begin{cases} 0, & \text{if } y_i < 0, \\ y_i, & \text{if } 0 \leq y_i \leq 1, \\ 1, & \text{if } 1 < y_i. \end{cases}$ 
8:   until  $\|\hat{\mathbf{x}} - \mathbf{x}\|_2^2 < \epsilon_{in}$ 
9:    $\mu \leftarrow \mu + \mu_\Delta$ 
10: until  $\max_{i \in \{1, \dots, n^2\}} (\min(x_i, 1 - x_i)) < \epsilon_{out}$ 

```

We gathered such a phantom database, by collecting test images from various sources. Some phantoms were used for testing reconstruction algorithms in previous studies [11, 68], and some come from the 2-D image database of the IAPR Technical Committee on DISCRETE GEOMETRY (TC18) [73]. All of the images had the same size of 256 by 256 pixels. The test images are collected in Appendix C.

For the evaluation of the data, we used two types of numerical measures, which are given below.

1.3.1 Measuring the error of reconstructions

Assume, that we have a software phantom, with a known \mathbf{x}^* vector of pixel values. Also assume, that we produced the \mathbf{b} projections of \mathbf{x}^* , and performed a reconstruction algorithm that resulted in an $\hat{\mathbf{x}}$ output.

The *Relative Mean Error* (*RME*) measurement defines the error of the reconstruction with the formula

$$RME(\mathbf{x}^*, \hat{\mathbf{x}}) = \frac{\sum_i |x_i^* - \hat{x}_i|}{\sum_i \lceil x_i^* \rceil}. \quad (1.13)$$

The *RME* value describes a reconstruction by giving the difference of the reconstructed pixels, compared to a predefined expected result. It is also normalized by the $\sum_i \lceil x_i^* \rceil$ value, which – with our assumption of Section 1.1, that is, $\phi_j \in [0, 1]$ for all elements of the $\Phi = \{\phi_0, \dots, \phi_c\}$ – gives the number of non-zero pixels of the image, to scale the error measurement. The final value is a number that gives the ratio of the amount of error compared to the area of the object to be reconstructed. Values of 0 will correspond to perfect reconstructions, and higher values

denote higher error. With an *RME* of 1 the error of the reconstruction equals to the size of the object.

Although, normalizing with the object area instead of the size of the reconstructed volume can lead to *RME* values greater than 1, this way the error measurement of the reconstruction will not be sensitive to scaling, or zero padding of the reconstructed volume, which gives a good ground for comparison.

1.3.2 Pearson's correlation coefficient

In the evaluation of the methods in Chapter 3 and Chapter 4 we will also need a tool for comparing the correlation between values in measurement vectors. For this purpose we used the *Pearson's correlation coefficient* [54]. Assuming that there are two vectors \mathbf{x} and \mathbf{y} of observations to compare, the correlation coefficient is calculated with the formula

$$r_{\mathbf{x},\mathbf{y}} = \frac{\sum_{i=1}^{n^2} (x_i - \bar{\mathbf{x}})(y_i - \bar{\mathbf{y}})}{\sqrt{\sum_{i=1}^{n^2} (x_i - \bar{\mathbf{x}})^2} \sqrt{\sum_{i=1}^{n^2} (y_i - \bar{\mathbf{y}})^2}}, \quad (1.14)$$

where $\bar{\mathbf{x}}$ and $\bar{\mathbf{y}}$ are the expected values in the vectors \mathbf{x} and \mathbf{y} .

This coefficient is capable of measuring linear correspondence between the elements of two data vectors. It takes a value close to 1 or -1 if there is a strict linear correspondence between the same position of \mathbf{x} and \mathbf{y} , and shifts towards 0 if the correlation of the data is weaker. If there is no linear correspondence at all $r_{\mathbf{x},\mathbf{y}}$ will take a value of 0.

The $r_{\mathbf{x},\mathbf{y}}$ expression will be useful for measuring the correlation between sequences of observations such as reconstructions performed under the same conditions.

1.4 Modelling measurement errors in the reconstructions

In practical applications, the projection data is usually corrupted by some type of distortion of the projection values, or random noise. For modelling this phenomenon in the tests, we used additive Gaussian noise for the distortion of the data. This was done by taking the projection values, and adding a random number to them from a Gaussian distribution with a 0 mean and a specified σ standard deviation. With the different settings of σ , we could introduce noise of different level to the projection data.

Although, the projection acquisition techniques used for transmission tomog-

raphy are usually affected by Poisson-, rather than additive Gaussian noise, we still used the latter one for several reasons. In real-world applications the level of projection noise relies on many conditions, such as the characteristics of the radiation used for the projection acquisition, the beam strength, the properties of the material in the object, background noise, etc., most of which is dealt with in preprocessing steps [16, 27, 40, 49]. Unfortunately, this makes the lifelike modelling of the noise extremely complicated, and highly application specific. For this reason, we have chosen to use an additive Gaussian noise model instead, which is a common technique for modelling distortions of the projections in transmission tomography [20, 27, 49, 68]. This way we could keep the formulation simpler, and did not lose the generality of the results because of adjusting them to one specific field of application.

Chapter 2

Direction-Dependency in Discrete Tomography

2.1 Introduction

With discrete tomography one can reconstruct the inner structure of an image from only a few (say, up to 2-10) projections. In this case, the low number of projections give a great freedom in choosing the projection directions to work with (see, Figure 2.1 for an illustration).

In a previous work [52], the authors briefly showed, that this freedom on the choice of projections can influence the accuracy of the reconstruction, and one can get different results from different projection sets. In this chapter we will give an extension of the previous experiments, that was aimed to discover deeper explanation of this *direction-dependency* of reconstructions. The aim was to determine if a better choice of projections can yield a significant improvement of the reconstructed results, and if there are regularities which make this phenomenon predictable and exploitable.

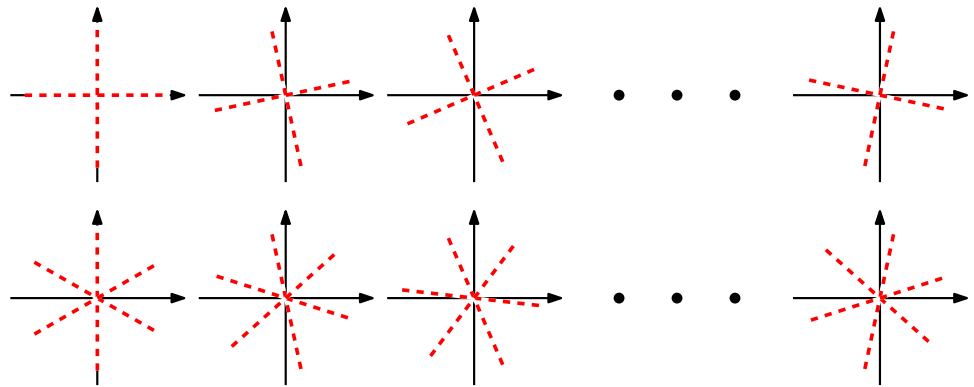


Figure 2.1: Some possible projection directions with low projection numbers. (Red dashed lines indicate the directions of the projection beams.)

Such studies are motivated by practical applications. In many fields using discrete and binary tomography, there are limitations on the number of projections, because the projection acquisition can have a high cost, or can damage the object of study. In these cases, we could benefit from lowering the number of required projections, or increasing the accuracy of the reconstructions by only improving the projection acquisition with some smart projection selection strategies.

2.2 Angle selection strategies

The direction-dependency problem was examined experimentally. We have set up a test frame-set, in which we could perform a large number of reconstructions. For the tests, we took the 22 binary phantoms of Appendix C, produced their projection sets containing the same numbers of projections, but different projection directions, and performed reconstructions from these simulated data sets to see if the choice of projection directions itself can influence the accuracy of the reconstructions, and if we could improve the reconstruction only by finding better directions.

The applied projection selection strategies are described below. The methods rely on the ground truth reconstruction and try to improve the projections using the original image as a basis. In the sequel, a projection set will be determined by a set of angles

$$S = \{\alpha_1, \alpha_2, \dots, \alpha_p\}, \quad (2.1)$$

giving the direction of the projection lines in (1.1).

2.2.1 Equiangular projection sets

First of all, we used equiangular projection sets, which are determined by a special set of angles. Such sets are generated by dividing the half circle into equal partitions and placing a p number of projection angles on it. With this, an equiangular projection angle set has basically two parameters, a p number of projections, and an α_0 starting angle. Formally, the set of $S(p, \alpha_0)$ projection angles can be given in the form

$$S(p, \alpha_0) = \left\{ \alpha_0 + i \frac{180^\circ}{p} \mid i = 0, \dots, p-1 \right\}. \quad (2.2)$$

An illustration of the projection angles is shown in Figure 2.2.

Furthermore, we will use group of equiangular projection angle sets determined by integer starting angles as

$$S(p) = \left\{ S(p, \alpha_0) \mid \alpha_0 \in \left\{ 0^\circ, \dots, \left\lceil \frac{180^\circ}{p} - 1^\circ \right\rceil \right\} \right\}. \quad (2.3)$$

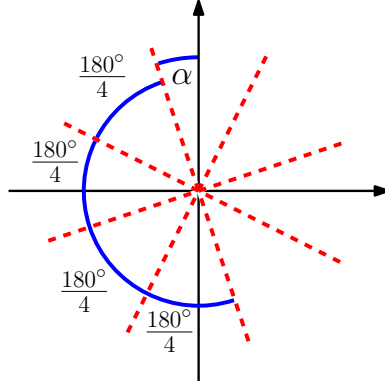


Figure 2.2: Example of the equiangular projection angle sets (angle set $S(4, \alpha)$).

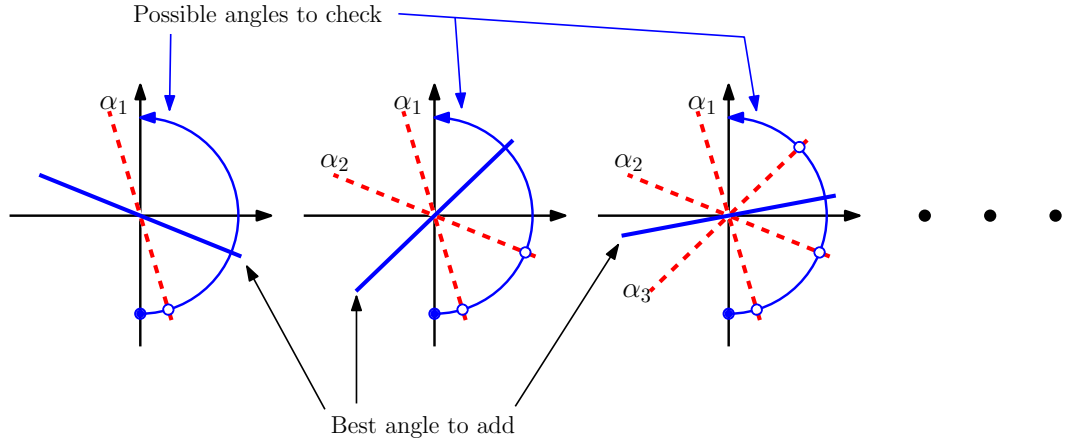


Figure 2.3: Steps of the *Greedy* projection selection strategy.

The $S(p)$ gives a well-defined series of projection angles on which we could examine the effects of the rotation of the object in the scanner. In the sequel, we will also highlight two elements of these sets, and for each image and p projection count, we will refer to the element of $S(p)$ leading to the best and worst reconstruction as *EquiAng-B*, and *EquiAng-W*, respectively.

2.2.2 Angle insertion by greedy angle testing

The second angle selection strategy uses a heuristic approach for building up good non-equiaangular projection sets. The method starts from an empty set of projections. Then, the process iteratively tests a set of possible next projections, to determine which projection causes the biggest improvement in the reconstruction if added to the projection set. This best projection is then added to the current set of projections. The formal description of this angle selection strategy is given in Algorithm 4, and the process is illustrated in Figure 2.3. This angle selection algorithm will later be referred to as *Greedy*.

As a result, we get an increasing list of projections each element adding the

Algorithm 4 Greedy angle selection (*Greedy*)**Input:** \mathbf{x}^* vector of image pixel values, $p \geq 2$ maximal number of angles;**Output:** S set of projection angles.

```

1:  $S \leftarrow \emptyset$ 
2:  $k \leftarrow 0$ 
3: repeat
4:    $\eta \leftarrow \infty$ 
5:   for each  $\alpha \in \{0, 1, \dots, 180\} \setminus S$  do
6:     Let  $\hat{\mathbf{x}}$  be the reconstruction from the projection set with  $(S \cup \{\alpha\})$  angles
7:     if  $RME(\mathbf{x}^*, \hat{\mathbf{x}}) < \eta$  then
8:        $\alpha^* \leftarrow \alpha$ 
9:        $\eta \leftarrow RME(\mathbf{x}^*, \hat{\mathbf{x}})$ 
10:    end if
11:     $S \leftarrow S \cup \{\alpha^*\}$ 
12:  end for
13:   $k \leftarrow k + 1$ 
14: until  $k = p$ 
15: return  $S$ 

```

locally best choice to the previous ones. The reconstructions from the projection sets provided by this algorithm can then be compared to the results of the equiangular reconstructions, to see how much improvement can be reached when non-equiangular projection sets are also allowed.

2.2.3 Altering angles by simulated annealing

Another method for choosing non-equiangular angle sets was based on the optimization of the error of the reconstruction by Simulated Annealing (SA) [50]. SA is a stochastic optimization technique, that starts with an arbitrary initial solution of an optimization problem, and iteratively improves the results by making small changes of the current guess, and accepts the modification based on the change of the optimized energy function. It is capable of finding the optimal solution of any optimization problem with a probability of 1, if the proper parameter setting is used. If we define the search space on the possible projection angle sets and the energy function as the RME values of the corresponding reconstructions, we get a method, that seeks the optimal projection angle set by improving an initial guess.

For each p projection number, our SA based angle selection process starts with an equiangular projection set. Then, it iteratively chooses a projection with an α angle, and it exchanges this projection with another one. The angle of the new projection will be taken from the

$$\mathcal{N}_\beta(\alpha) = \{\delta \mid \delta \in \mathbb{Z}_{180}, |\delta - \alpha| \leq \beta\} \quad (2.4)$$

range of integer angles differing at most in β degrees from the original α . If the resulting projection set leads to a better reconstruction, then we accept it. If the reconstruction from the new projection set is worse, then we accept or reject the change with a probability based on the change of accuracy.

The formal description of this method is given in Algorithm 5, and an illustration can be seen in Figure 2.4. The algorithm uses the $Random(\Omega)$ notation for a function that returns a random element of the Ω set, with a uniform distribution. We will refer to this angle selection strategy as *AltAng*, in the sequel.

Algorithm 5 SA angle selection (*AltAng*)

Input: \mathbf{x}^* vector of image pixel values; $p \geq 2$ number of projections; β angle neighborhood; T_0 starting temperature; $0 < h < 1$ temperature cooling factor; k_{max} maximal iteration count

Output: S set of projection angles.

```

1:  $S \leftarrow S(p, 0^\circ)$ 
2:  $T \leftarrow T_0$ 
3:  $\hat{\mathbf{x}} \leftarrow$  reconstruction from the  $S$  set
4:  $k \leftarrow 0$ 
5: repeat
6:    $\alpha \leftarrow Random(S)$  {choose a random elemnt of the angle set}
7:    $\alpha' \leftarrow Random(N_\beta(\alpha) \setminus S)$ 
8:    $S' \leftarrow S \setminus \{\alpha\} \cup \{\alpha'\}$ 
9:    $\mathbf{x}' \leftarrow$  reconstruction from the  $S'$  set
10:   $\Delta RME \leftarrow RME(\mathbf{x}^*, \mathbf{x}') - RME(\mathbf{x}^*, \hat{\mathbf{x}})$ 
11:   $\xi \leftarrow Random([0, 1])$ 
12:  if  $\xi > \exp(-\frac{\Delta RME}{T})$  then
13:     $S \leftarrow S'$ 
14:     $\hat{\mathbf{x}} \leftarrow \mathbf{x}'$ 
15:  end if
16:   $T \leftarrow T \cdot h$ 
17:   $k \leftarrow k + 1$ 
18: until  $k = k_{max}$ 
19: return  $S$ 

```

If the parameters of this process are properly set, one can find – or at least approximate – the optimal projection set. In this work, we have fine-tuned the parameters of the algorithm empirically, and used the values $T_0 = 0.02$, $h = 0.95$, $\beta = (180^\circ/p - 5^\circ)$, and $k_{max} = 200$. The final angle set for each image, and projection number was selected as the best of five consecutive runs of the process. With these parameters the algorithm is not guaranteed to give optimal solutions, but provides acceptably results in reasonable time.

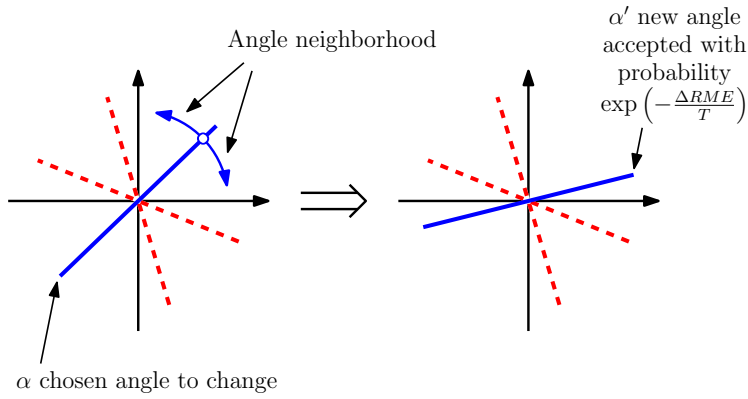


Figure 2.4: A step of the *AltAng* angle selection algorithm.

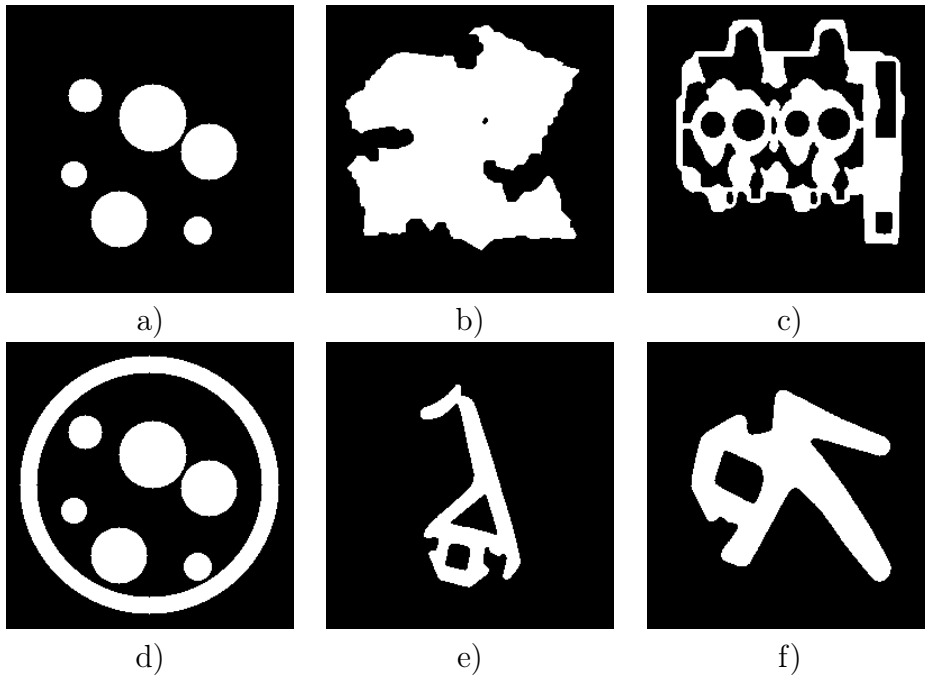


Figure 2.5: Sample of the software phantoms used for testing the direction-dependency.

2.3 Test environment

In the tests, we used the 22 binary phantom images of the image database in Appendix C, and reconstructed them from different sets of their projections. For a later reference, some highlighted images are provided in Figure 2.5. The reconstructions were performed by three reconstruction algorithms under different conditions, i.e., varying projection counts, distortions of the projection data, etc..

2.3.1 Reconstruction algorithms and parameters

We performed reconstructions from each projection set with the TSIRT, DC and DART reconstruction algorithms that were described in detail in Section 1.2. The

parameters of the reconstruction algorithms were set empirically, tuned to gain the best reconstructions possible.

In case of the TSIRT algorithm, the parameters were set as $\epsilon = 0.01$ and $k_{max} = 1000$. With the DART algorithm, the continuous reconstructions were performed by 10 iterations of the SIRT, and the smoothing operation between the consecutive steps were calculated with a convolution [31] operation. The smoothing kernel was defined as

$$K = \begin{bmatrix} 1/16 & 1/16 & 1/16 \\ 1/16 & 1/2 & 1/16 \\ 1/16 & 1/16 & 1/16 \end{bmatrix}.$$

The stopping criteria of the algorithm was defined by using the parameters $k_{\Delta} = 10$, and $k_{max} = 500$. In case of the DC algorithm, we used the parameters $\mu_{\Delta} = 0.1$, $\gamma = 0.25$, $\epsilon_{in} = 0.1$ and $\epsilon_{out} = 0.01$.

2.3.2 Noise on the projection data

We performed reconstructions both from perfect, noiseless projections and data corrupted with three different levels of Gaussian random noise described in Section 1.4. The levels of the noise was set to three different $\sigma \in \{0.5; 1.5; 5.0\}$ standard deviations. Given that an average projection value of the test images were about 40, the magnitude of the noise compared to the data was about 1.25%, 3.75% and 12.55%.

2.3.3 Implementation

We had to perform a large number of reconstructions for a valid experimental analysis, which required highly efficient implementation of the reconstruction algorithms. Previous studies indicated that the mentioned reconstruction algorithms are suitable for highly parallel implementation [47], therefore we developed the code in C++ with GPU acceleration using the Nvidia CUDA SDK [72]. With this implementation, we performed more than 200 000 reconstructions in about 200 hours on a single PC containing an Intel Q9500 CPU, and an Nvidia Geforce 250 GPU.

2.4 Results

This section summarizes the most important findings of our experiments on the direction-dependency of reconstructions.

2.4.1 Equiangular projection sets

First, we wanted to determine if the reconstructions could be improved by finding better projection angles. In the first set of software tests we used only the DC reconstruction algorithm and the equiangular projection sets. In this way, we could determine if the reconstruction depends on the orientation of the object of study in the scanner.

We produced different equiangular projection sets of the phantoms with projection numbers ranging from 2 to 16. With each projection number, projection sets were taken with different starting angles. The starting angles were integer numbers in degrees ranging from 0° to $\left\lceil \frac{180^\circ}{p} - 1^\circ \right\rceil$. This gave a total number of 431 projection sets for each phantom.

For the evaluation of the data, we computed the *RME* value of each reconstruction and compared the results belonging to the same phantom image and projection number, but taken from different projection angle sets, that is, we compared the results belonging to the $S(p)$ projection direction sets for each image. We also defined a measurement of the rotation-dependency, that can describe how dependent an object is to the choice of the α starting angle.

Let $\mathbf{R}_{\text{Alg}}(\mathbf{x}^*, p, \alpha)$ denote the reconstruction of the \mathbf{x}^* expected image from the projection set determined by the angles of $S(p, \alpha)$, reconstructed by a given *Alg* reconstruction algorithm (such as the ones described in Section 1.2). For example $\mathbf{R}_{\text{DC}}(\mathbf{x}^*, 4, 0^\circ)$ denotes the reconstruction of an \mathbf{x}^* phantom performed with the DC algorithm using the projection set containing 4 equiangular projections with a 0° starting angle. Let

$$\mathbf{R}_{\text{Alg}}(\mathbf{x}^*, p) = \left\{ \mathbf{R}_{\text{Alg}}(\mathbf{x}^*, p, \alpha) \mid \alpha \in \left\{ 0^\circ, \dots, \left\lceil \frac{180^\circ}{p} - 1^\circ \right\rceil \right\} \right\} \quad (2.5)$$

be the set of all reconstructions of the same phantom, performed with the same *Alg* reconstruction algorithm, from the same p number of projections but with all possible integer starting angles.

With the previous notation the direction-dependency measurement can be given as

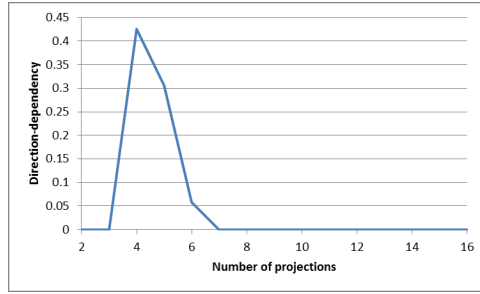
$$D_{\text{Alg}}^\sigma(\mathbf{x}^*, p) = (E_{\text{Alg}}^{\max}(\mathbf{x}^*, p) - E_{\text{Alg}}^{\min}(\mathbf{x}^*, p)) \cdot \exp \left(-\frac{(E_{\text{Alg}}^{\min}(\mathbf{x}^*, p))^2}{\sigma^2} \right) , \quad (2.6)$$

where

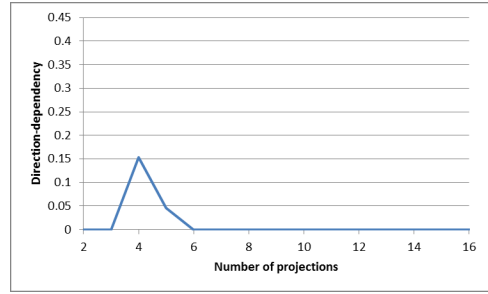
$$E_{\text{Alg}}^{\min}(\mathbf{x}^*, p) = \min \{ RME(\mathbf{x}^*, \mathbf{y}) \mid \mathbf{y} \in \mathbf{R}_{\text{Alg}}(\mathbf{x}^*, p) \} , \quad (2.7)$$

and

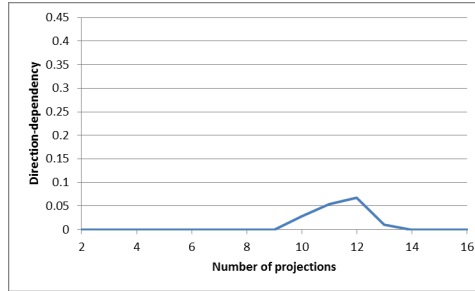
$$E_{\text{Alg}}^{\max}(\mathbf{x}^*, p) = \max \{ RME(\mathbf{x}^*, \mathbf{y}) \mid \mathbf{y} \in \mathbf{R}_{\text{Alg}}(\mathbf{x}^*, p) \} . \quad (2.8)$$



Results for Figure 2.5a



Results for Figure 2.5b



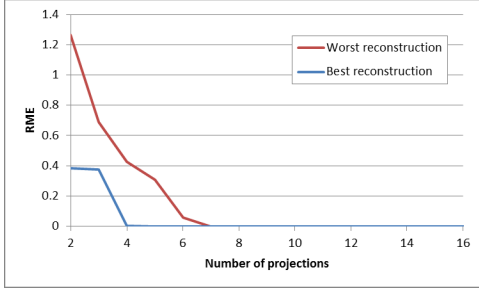
Results for Figure 2.5c

Figure 2.6: Direction-dependency graphs of three phantoms, according to the number of projections. Higher values indicate that the phantom is more dependent on the choice of projections.

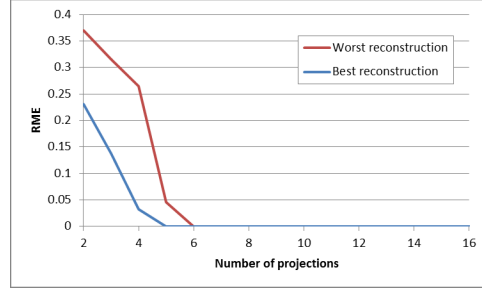
By this direction-dependency measurement, we could find projection setups (phantom image, projection number pairs) which were the most sensitive to the choice of projection angles. The $D_{Alg}^{\sigma}(\mathbf{x}^*, p)$ takes two factors into account. First of all, it measures how big the difference can be between the reconstructions of the best and worst considered projection sets. Also, it is multiplied with a constant computed from the accuracy of the best reconstruction by a Gaussian function. This will result in high direction-dependency values, if one can get good reconstructions with the right projection sets, and highly inaccurate results if the projection sets are not well chosen. On the other hand, if there is no big difference in the results or there is a relatively big difference, but both the best and worst reconstructions contain an unacceptably high amount of error – higher than the σ parameter of (2.6) – then the direction-dependency will be low.

After performing the reconstructions, we used the $D_{Alg}^{\sigma}(\mathbf{x}^*, p)$ measurement of (2.6) to find the projection setups which were the most sensitive to the rotation. For this, we set the $\sigma = 0.05$ parameter – that tolerates approximately 5 percent error in the reconstructions – and tested each $\mathbf{R}_{Alg}(\mathbf{x}^*, p)$ set of reconstructions. Some such results can be seen in Figure 2.6.

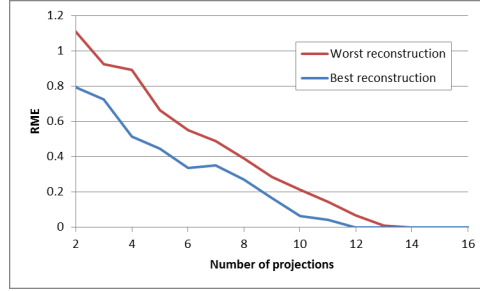
The results showed that all the phantom images – including all the binary phantoms of Appendix C – were dependent on the choice of projections, some for higher, some for lower degree. In overall, the direction-dependency curves had 2 to 3



Results for Figure 2.5a



Results for Figure 2.5b



Results for Figure 2.5c

Figure 2.7: Minimal and maximal RME values of reconstructed phantoms according to the number of projections.

peak values at each phantom, at consecutive projection numbers. This phenomena can be explained by taking a look at the minimal and maximal RME values of the best and worst reconstructions for each $\mathbf{R}_{DC}(\mathbf{x}^*, p)$ set, that are depicted in Figure 2.7.

Looking at the curves on Figure 2.7 one can note, that there is a significant gap between the accuracy of the best and worst reconstructions for most projection numbers. From the viewpoint of the direction-dependency measurement, we can see that the best reconstruction reaches an almost zero RME value from lower number of projections than the worst reconstructions. Since the direction-dependency measurement is constructed and parametrized to find such set-ups (where an almost perfect and an unacceptably useless reconstruction can either be found from projection sets containing the same numbers of projections) it takes the highest values around these projection counts.

Also, more projections usually provide more information in the reconstruction algorithm to work with, and most of the best-worst RME plots showed monotonously descending curves. This is the reason why there were adjacent peaks on the curves of the direction-dependency measure in Figure 2.6.

Finally, the high direction-dependency values, and large gaps in the best-worst RME curves show that the reconstruction can highly rely on the choice of projections, and one can improve the accuracy of the results only by finding the proper projections. This can also be seen in Figure 2.8 where we gave some examples

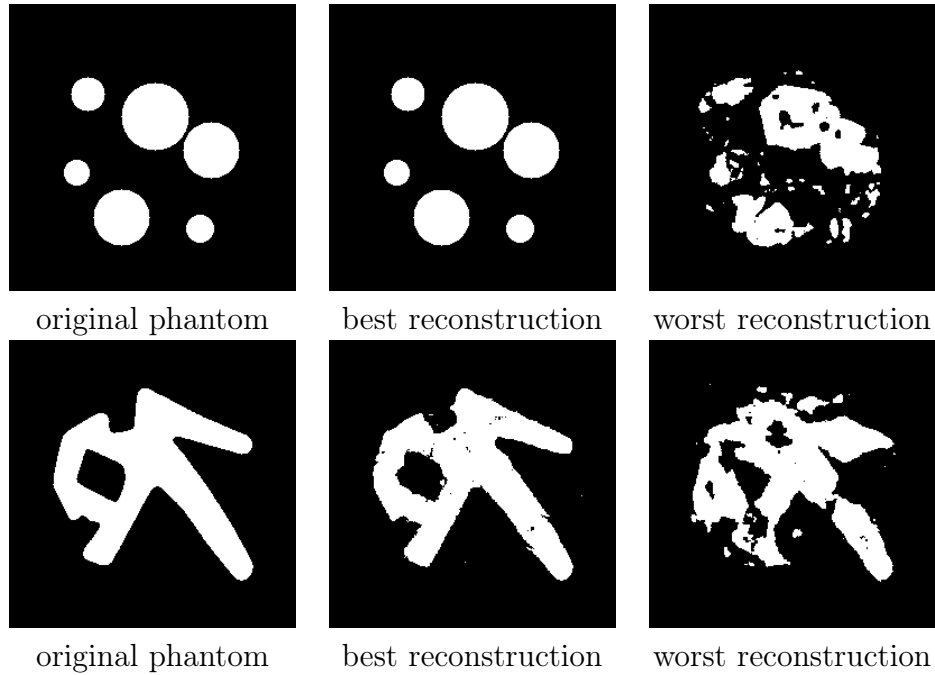


Figure 2.8: Two examples presenting the differences of the reconstructions performed from different projection sets containing four projections.

of reconstructions performed from projection sets containing the same number of projections, but taken with different starting angles.

We also plotted the RME values of each reconstruction in the $\mathbf{R}_{DC}(\mathbf{x}^*, p)$ sets according to the starting angle. By doing so, we could track the accuracy of the reconstructions when applying small changes of the directions of the projections. Such diagrams can be seen in Figure 2.9.

The first thing to notice on the diagrams of Figure 2.9 is that the curves are relatively smooth. This indicates, that projections close to each other hold similar information, and the reconstructed results will be similar in accuracy. Also, this correlates with another tendency, that by increasing the number of projections the direction-dependency of the reconstruction is decreasing. In the equiangular case, by increasing the number of projections the angle difference between consecutive projection directions becomes smaller. This way, the freedom in choosing the projections will be smaller because projections close to each other provide similar information. This also means that one should only expect a significant direction-dependency in the reconstructions, with relatively simple objects, which can be reconstructed from only few projections.

Furthermore, note that for each phantom image and projection number, the direction-dependency characteristics were different, and the best reconstructions were gained from different projection sets as well. Finally, although only a sample of the results were presented here, the conclusions described above were general in all the tests.

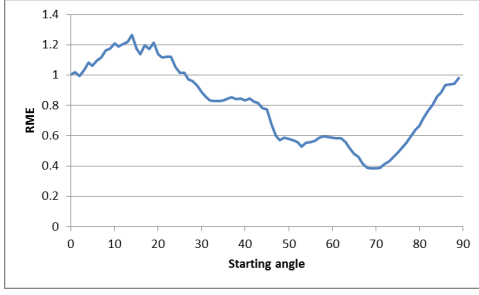
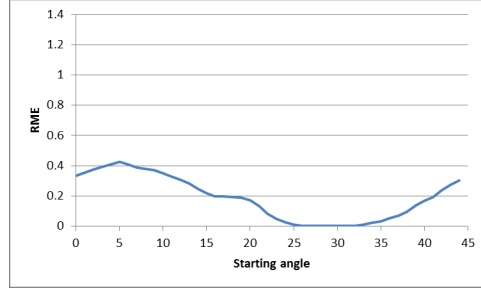
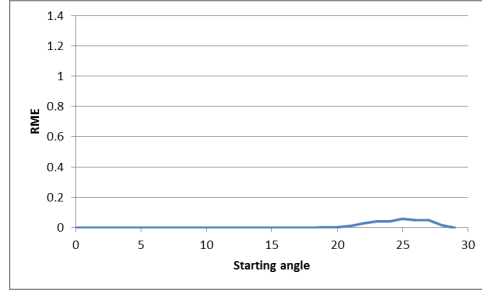
*RME* values from 2 projections*RME* values from 4 projections*RME* values from 6 projections

Figure 2.9: *RME* values of the reconstructions of the phantom of Figure 2.5a according to the starting angle, from projection sets containing different numbers of projections. The phantom was reconstructed by the DC algorithm.

2.4.2 Non-equiangular projection sets

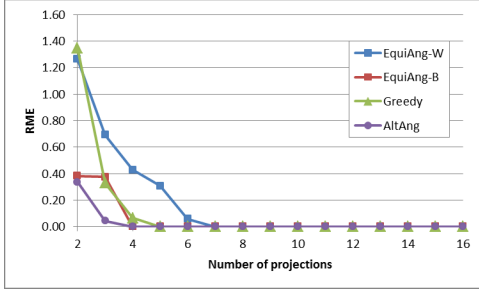
In a further test, we performed reconstructions with the *Greedy* and *AltAng* non-equiangular angle selection strategies described in Section 2.2. The main aim of this work was to determine if further improvement can be reached in the reconstructions by extending the freedom of the projection directions.

Naturally, there is a much bigger set of possibilities in this case, since we do not only choose the direction of one starting angle, but the directions of each projection. Here, even when considering only integer angles between 0° and 179° the number of angle sets is $\binom{180}{p}$ for each p projection counts. This also makes an exhaustive search impossible to carry out since, even with only 4 projections, the possible choices would define 42 296 805 projection sets. This is the reason why we used the non-equiangular projection selection strategies of Section 2.2, and we only tried to improve the results of the $S(p, 0^\circ)$ equiangular projection set by using non-equiangular projections.

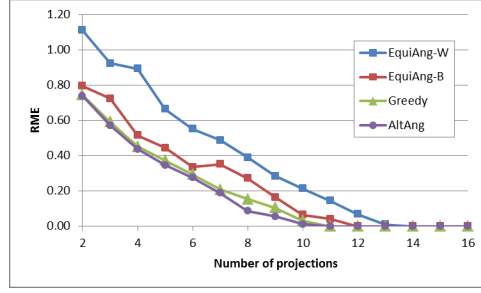
If using non-equiangular projection sets can bring further improvement to the reconstruction, then it should turn out simply by comparing the *RME* values on the reconstruction of the different phantom images. Some such results are summarized in Table 2.1. Furthermore, Figure 2.10 provides some diagrams of the performance of the projection selection strategies according to the number of projections.

Table 2.1: *RME* of the reconstructions produced from the projection sets given by the four angle selection strategies. Reconstructions were performed by the DC algorithm. Equiang-W, and EquiAng-B denotes, respectively, the result of the worst and best equiangular projection sets. The best results in each column are highlighted in bold.

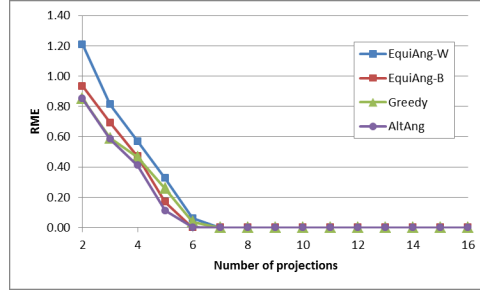
Proj.Num.	2	3	4	5	6	7	8	9	10	11
Figure 2.5a										
EquiAng-W	1.263	0.690	0.427	0.306	0.058	0	0	0	0	0
EquiAng-B	0.382	0.375	0.001	0	0	0	0	0	0	0
Greedy	1.346	0.328	0.065	0	0	0	0	0	0	0
AltAng	0.336	0.044	0.000	0	0	0	0	0	0	0
Figure 2.5b										
EquiAng-W	0.370	0.315	0.265	0.046	0.000	0	0	0	0	0
EquiAng-B	0.230	0.138	0.032	0	0	0	0	0	0	0
Greedy	0.248	0.108	0.026	0	0	0	0	0	0	0
AltAng	0.252	0.039	0.003	0	0	0	0	0	0	0
Figure 2.5c										
EquiAng-W	1.111	0.924	0.893	0.663	0.551	0.488	0.390	0.284	0.214	0.145
EquiAng-B	0.795	0.725	0.515	0.444	0.336	0.352	0.273	0.165	0.064	0.041
Greedy	0.744	0.591	0.451	0.374	0.293	0.209	0.154	0.106	0.032	0
AltAng	0.738	0.572	0.436	0.347	0.276	0.188	0.087	0.056	0.012	0
Figure 2.5d										
EquiAng-W	1.208	0.812	0.569	0.326	0.061	0.000	0	0	0	0
EquiAng-B	0.934	0.693	0.469	0.169	0.000	0	0	0	0	0
Greedy	0.852	0.591	0.466	0.258	0.038	0	0	0	0	0
AltAng	0.852	0.584	0.411	0.113	0.001	0	0	0	0	0
Figure 2.5e										
EquiAng-W	1.320	0.883	0.345	0.102	0.025	0.000	0	0	0	0
EquiAng-B	0.562	0.148	0.114	0.005	0.000	0	0	0	0	0
Greedy	0.486	0.108	0.034	0.001	0	0	0	0	0	0
AltAng	0.457	0.088	0.010	0.000	0	0	0	0	0	0
Figure 2.5f										
EquiAng-W	0.866	0.667	0.448	0.186	0.000	0.000	0	0	0	0
EquiAng-B	0.548	0.169	0.050	0.000	0	0	0	0	0	0
Greedy	0.576	0.153	0.012	0	0	0	0	0	0	0
AltAng	0.533	0.101	0.001	0	0	0	0	0	0	0



Results for Figure 2.5a



Results for Figure 2.5c



Results for Figure 2.5d

Figure 2.10: RME values of the reconstructions of three phantoms in Figure 2.5 with the angle sets provided by the four different angle selection algorithms.

Based on the results, we can draw the consequence that using non-equiangular projection sets yield further improvement in the quality of the reconstructions, in the test cases. This kind of improvement is also clearly visible on the reconstructed images (see, e.g., Figure 2.11). Like in the case of equiangular projection sets this phenomena strongly relies on the image reconstructed. For some images a great improvement was reached if the projection directions were properly chosen, for others the difference was not so significant.

In the comparison of the angle selection methods we found, that the worst results always came from the worst equiangular projection sets, which was expected, since this method was only included as a base for comparison. We could usually get much better results by fine-tuning the directions and searching for the best equiangular projections.

In case of the non-equiangular projection sets, the *Greedy* method usually produced better results than the equiangular projections, but its process included unchangeable decisions when adding projection angles, that made it likely to get stuck in a local minima. The *AltAng* method on the other hand did not have this weakness, and usually resulted in the best projection set.

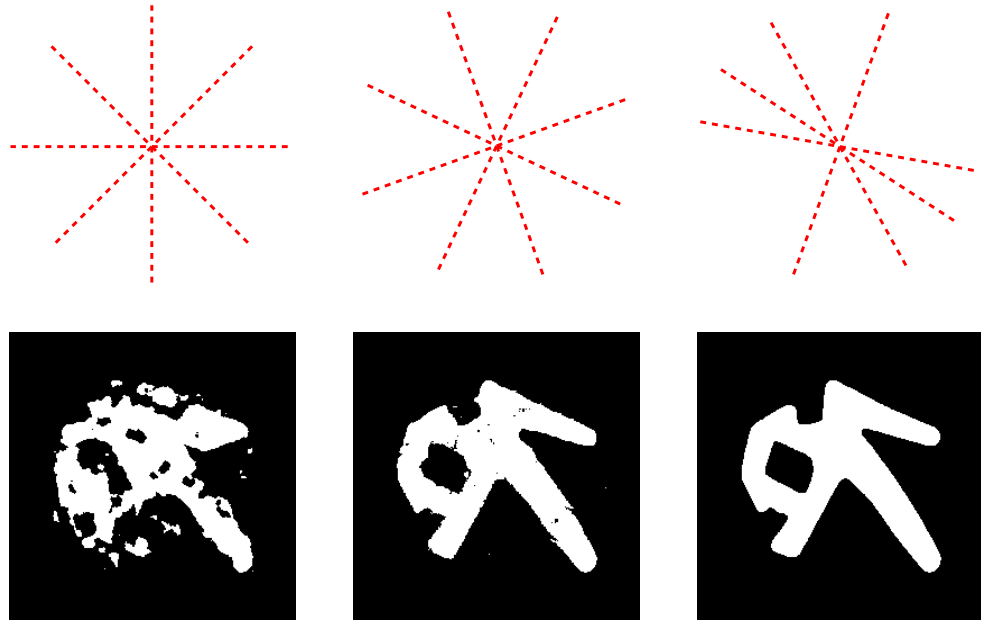


Figure 2.11: Reconstructions of the phantom in Figure 2.5f with $S(4, 0^\circ)$, $S(4, 19^\circ)$, and $S = \langle 29^\circ, 57^\circ, 80^\circ, 160^\circ \rangle$ projection sets, from left to right, respectively. Red dashed lines indicate the directions of the projections, images below are the corresponding reconstructions.

2.4.3 Different reconstruction algorithms

We also compared the results of different reconstruction algorithms, to investigate whether the direction-dependency of objects is independent from the applied reconstruction algorithm. If it is so, then the direction-dependency is likely to be a property coming from the information content of the projections themselves.

We produced different $S(p, \alpha)$ equiangular projection sets of the binary phantom images, and performed reconstructions by three different reconstruction algorithms, which were the TSIRT, DC, and DART described in Section 1.2. Again, the p number of projections in the projection sets ranged between 2 and 16 for each phantom image, and integer α starting angles were used from 0° to $\left\lceil \frac{180^\circ}{p} - 1^\circ \right\rceil$.

We first plotted the RME values belonging to each phantom and projection number according to the starting angle, and compared the diagrams belonging to the three different reconstruction algorithms. Some such diagrams can be seen in Figure 2.12. On most diagrams like those of Figure 2.12 the slopes of the curves belonging to the different reconstruction algorithms, were similar which indicates that there is a correspondence between the results of the reconstruction algorithms.

In addition, we found that the curves of the TSIRT and DC algorithms were relatively smooth. On the other hand, the curves belonging to the DART algorithm showed drastic changes of the RME values even for a 1° modifications of the projection angles. This indicates that the DART algorithm is more sensitive to the projection set-up than the other two methods. We also found that the DART

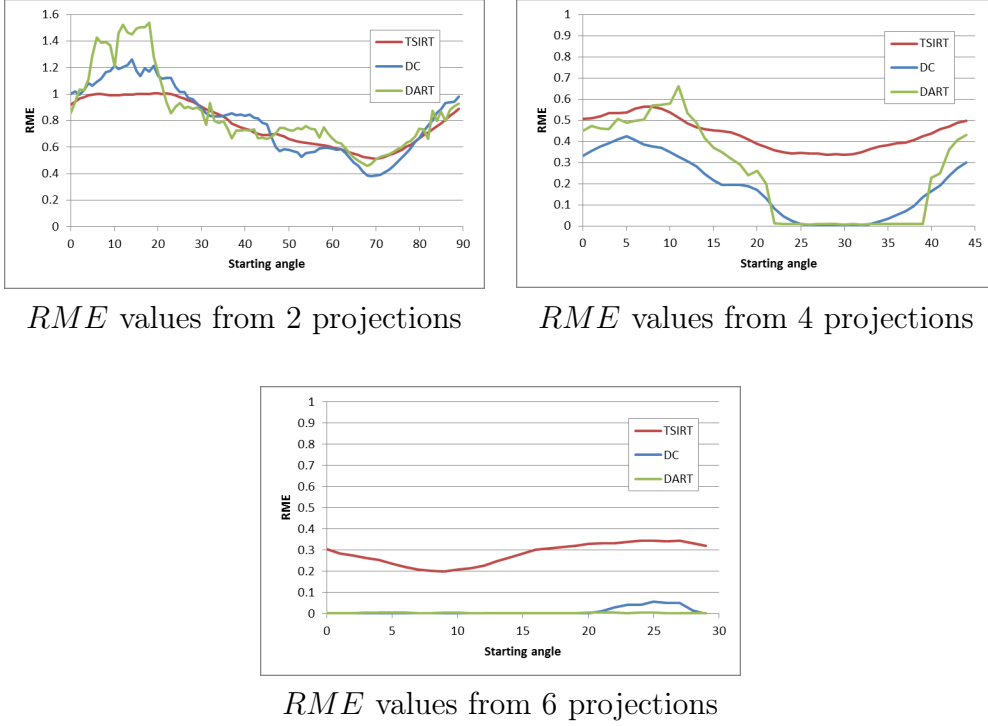


Figure 2.12: RME curves of the three reconstruction algorithms on the phantom of Figure 2.5a, with three different projection numbers.

algorithm had the biggest ranges in the corresponding RME values for most of the phantom images and most of the projection numbers. This meant that usually the DART gave the best results, when the proper projection set was found, but also for the same phantom and projection number it produced the worst results with the wrong projection sets. This indicates that, although the DART can perform better than the other algorithms, it is also more dependent on the choice of the projections.

For another evaluation of the data, we compared the RME values by the Pearson's correlation coefficient (1.14). In this case, \mathbf{x} and \mathbf{y} data vectors of the $r_{\mathbf{x},\mathbf{y}}$ correlation coefficient contained all the RME values belonging to one phantom and reconstruction algorithm (including all projection counts, and starting angles). These results are summarized in Table 2.2.

Most of the entries of Table 2.2 contain values close to one, which indicates a correspondence between the results of the reconstruction algorithms. The same consequence can be drawn if we plot the points given by the corresponding RME value pairs of the different reconstructions, as it can be seen in Figure 2.13. Most points of the diagrams are close to the diagonal, that indicates a correlation between the results of the algorithms. This indicates that the projection angle dependency is likely to be a property of the projection sets themselves, meaning that some projections hold more information than others and yield better reconstructions.

The only exception was in case of the Phantom 11 that neither the TSIRT nor

Table 2.2: Correlation between the direction-dependency characteristics of the TSIRT, DC, and DART algorithms, tested on 22 phantom images.

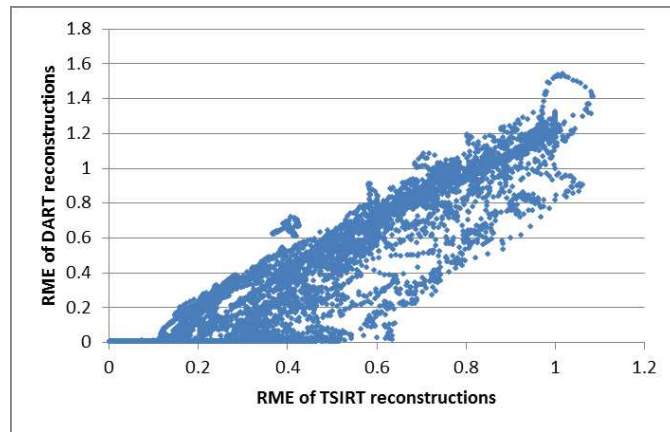
	TSIRT \leftrightarrow DC	TSIRT \leftrightarrow DART	DC \leftrightarrow DART
Phantom 1	0.94	0.95	0.98
Phantom 2	0.93	0.91	0.98
Phantom 3	0.89	0.91	0.98
Phantom 4	0.76	0.74	1.00
Phantom 5	0.85	0.86	1.00
Phantom 6	0.95	0.95	1.00
Phantom 7	0.83	0.81	0.98
Phantom 8	0.91	0.84	0.98
Phantom 9	0.87	0.79	0.98
Phantom 10	0.98	0.96	0.99
Phantom 11	n/a	n/a	n/a
Phantom 12	1.00	0.98	0.98
Phantom 13	1.00	0.98	0.98
Phantom 14	0.84	0.80	0.99
Phantom 15	0.83	0.81	0.97
Phantom 16	0.92	0.90	0.99
Phantom 17	0.83	0.80	1.00
Phantom 18	0.89	0.83	0.97
Phantom 19	0.92	0.91	0.99
Phantom 20	0.93	0.94	0.99
Phantom 21	0.96	0.93	0.98
Phantom 22	0.90	0.86	0.98

the DART algorithm could reconstruct. This image contains only small objects which the SIRT algorithm and the first continuous reconstruction of the DART could not detect at all, therefore the thresholded results were empty images. In this case the provided data was not suitable for the comparison.

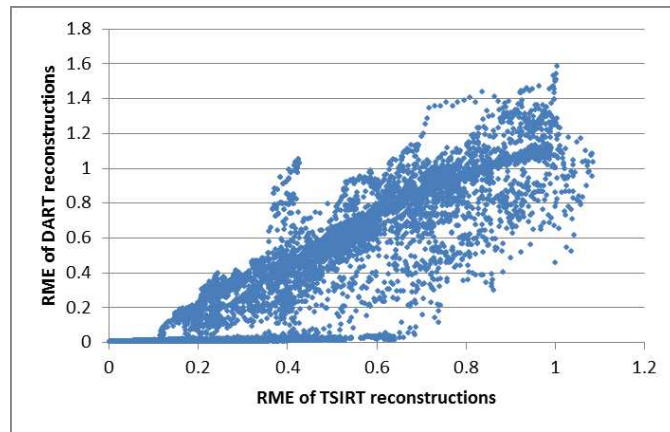
2.4.4 Distortion of the projection data

For simulating the errors of projection acquisition techniques we performed experimental tests with projection data distorted by random noise. We again used equiangular projections corrupted by additive Gaussian noise described in Section 1.4. In addition to the noise free case we added noise of three different strength to the data, which were determined by setting the σ deviance of the noise to the $\sigma \in \{0.5; 1.5; 5.0\}$ values. In this case the tests were only performed with the DC algorithm. This was sufficient since previous results indicated that the direction-dependency of different reconstruction algorithms are similar.

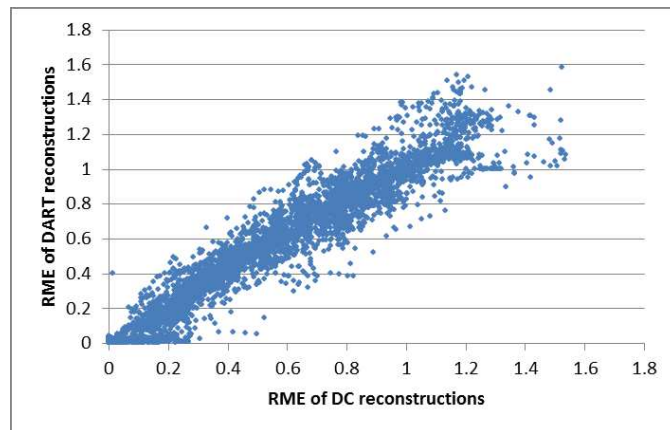
We again plotted the *RME* values of the reconstructions of each phantom image and projection number according to the starting angle. The goal was to compare



Comparison of the results of the TSIRT and DC algorithms



Comparison of the results of the TSIRT and DART algorithms



Comparison of the results of the DC and DART algorithms

Figure 2.13: Correlation between the RME values of different reconstruction algorithms on the same projection sets. Point coordinates are determined by the RME values of the results of two corresponding reconstructions. The diagrams present data for all the phantom images.

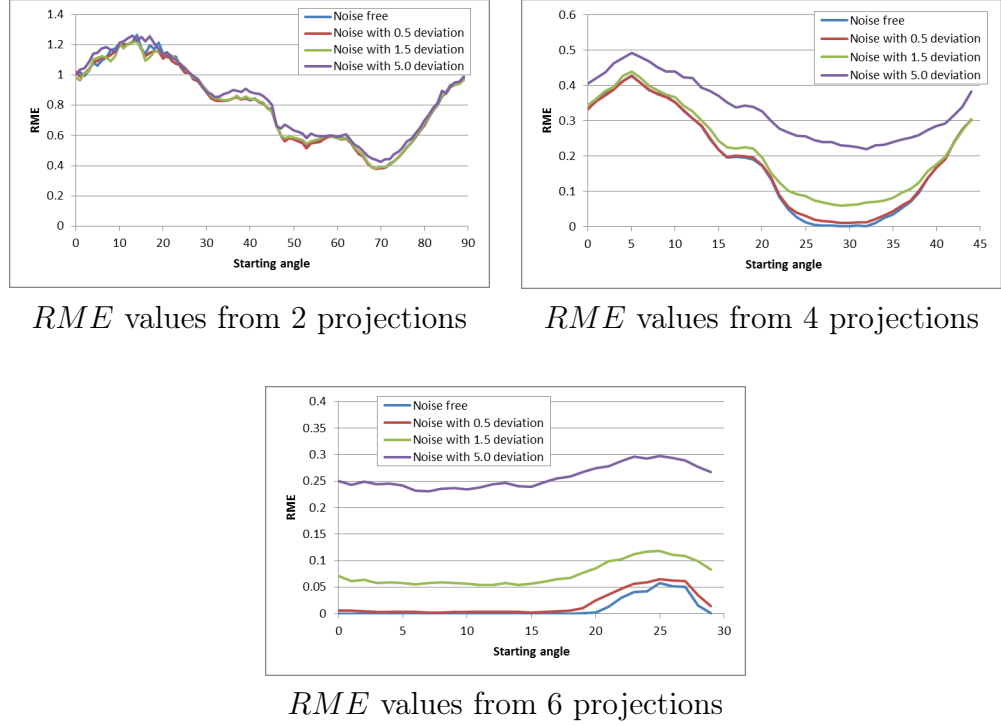


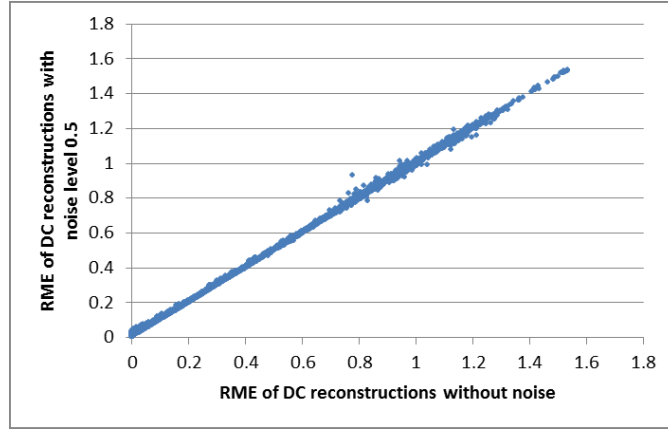
Figure 2.14: RME plots from the noisy projection data. Reconstructions of the phantom of Figure 2.5a were performed by the DC algorithm with equiangular projections sets containing 2, 4, and 6 projections.

the curves belonging to the different noise levels, and examine how the addition of noise changes the characteristics of the direction-dependency. Some such diagrams can be seen in Figure 2.14. As expected, we found that the noise in the projections resulted in reconstructions of lower accuracy. We also found, that this degradation of accuracy was uniform with all the projections belonging to the same phantom image, projection number and noise level. Compared to the noiseless case, this had the effect of shifting upwards the curves of the diagrams of Figure 2.14. Thus, we can say that the added noise in the projections did not change the direction-dependency characteristics of the phantoms in the test cases. Projection directions leading to better reconstructions than others in the noiseless case, were also found to be better when the projection values were affected by random noise.

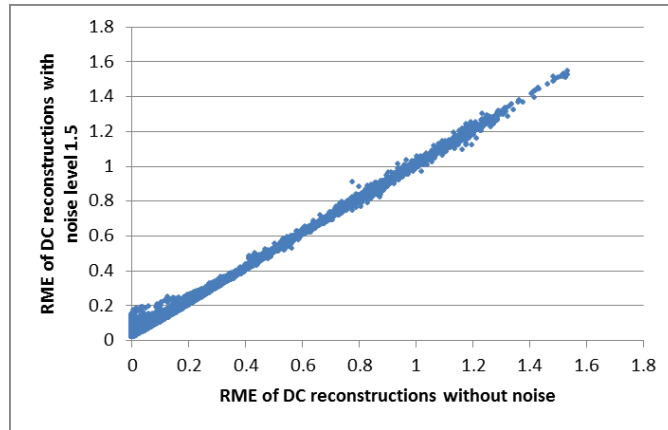
We found the same when we compared the results by the correlation coefficient. These results can be found in Table 2.3 where we calculated the correlation between the reconstructions in the noise-free case and the results coming from the noisy projections, for each phantom image separately. The point pairs examined by the correlation coefficient are plotted in Figure 2.15. All the entries of Table 2.3 are close to 1, and the points of Figure 2.15 are placed along the diagonal, which indicates a linear correspondence between the results gained from the projection sets affected by different levels of noise. Thus, the direction-dependency characteristics of objects remain similar when the projections are affected by random noise.

Table 2.3: Correlation between the direction-dependency characteristics of reconstructions with different levels of noise, and slightly modified objects, tested on 22 phantom images. The first three columns show results for the noise affected projections, the final column gives the statistics for the altered phantoms.

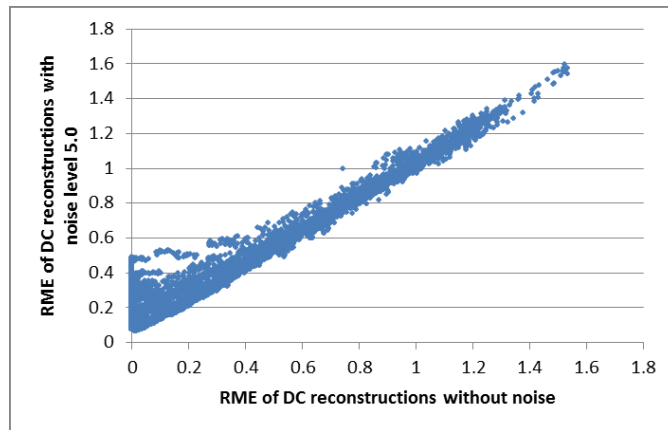
	$\sigma = 0.5$	$\sigma = 1.5$	$\sigma = 5.0$	Altered
Phantom 1	1.000	0.999	0.999	0.999
Phantom 2	1.000	1.000	1.000	0.998
Phantom 3	1.000	0.998	0.998	0.998
Phantom 4	1.000	0.999	0.999	0.988
Phantom 5	1.000	0.999	0.999	0.973
Phantom 6	1.000	1.000	1.000	0.999
Phantom 7	0.999	0.999	0.999	0.964
Phantom 8	1.000	1.000	1.000	0.991
Phantom 9	1.000	1.000	1.000	0.997
Phantom 10	1.000	0.998	0.998	0.997
Phantom 11	0.998	0.979	0.979	0.994
Phantom 12	1.000	0.999	0.999	0.997
Phantom 13	1.000	0.998	0.998	0.995
Phantom 14	1.000	0.999	0.999	0.996
Phantom 15	1.000	0.999	0.999	0.993
Phantom 16	1.000	0.999	0.999	0.999
Phantom 17	1.000	1.000	1.000	0.994
Phantom 18	1.000	0.998	0.998	0.997
Phantom 19	1.000	0.999	0.999	0.998
Phantom 20	0.999	0.999	0.999	0.997
Phantom 21	0.996	0.996	0.996	1.000
Phantom 22	1.000	0.997	0.997	0.999



Comparison of the results from the noise free projections, and projections affected by noise of 0.5 strength



Comparison of the results from the noise free projections, and projections affected by noise of 1.5 strength



Comparison of the results from the noise free projections, and projections affected by noise of 5.0 strength

Figure 2.15: Correlation between the RME values of different reconstruction algorithms on the same projection sets. Points coordinates are determined by the RME values of the results of two corresponding reconstructions. The diagrams hold data for all the phantom images.

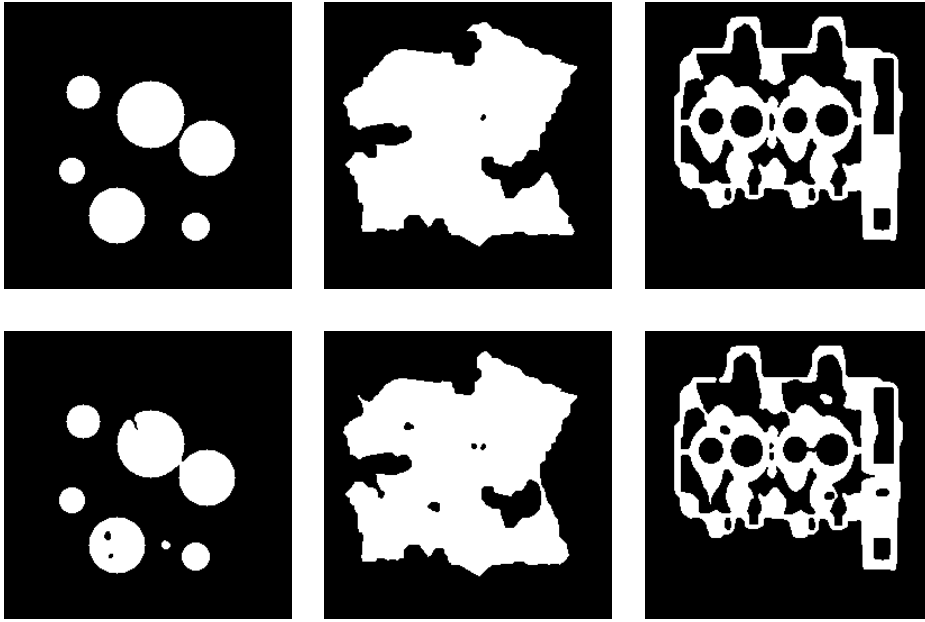


Figure 2.16: Some of the altered software phantoms used for testing. Original images can be seen in the top row, and their modified versions are in the bottom row.

2.4.5 Small distortions of the reconstructed objects

We also performed tests with slightly modified phantom images, which were intended to simulate the case when the object of study undergoes structural damage. These images were produced by introducing small, few-pixel modifications of the original phantoms, for simulating fractures and bubbles in the material. Some of these modified phantoms can be found in Figure 2.16.

First, we compared the results of the original and altered phantoms by comparing the *RME* value plots according to the starting angles of equiangular projection sets. Some of these plots are shown in Figure 2.17. Second, we paired up the *RME* values gained from projection sets taken from the same directions but the different (original and altered) versions of the phantoms, and calculated the correlation coefficient (1.14) between the resulted point sets. The results can be found in Figure 2.17, while Figure 2.18 visualises the point cloud itself.

We found that the small modifications of the object did not bring considerable changes to the direction-dependency characteristics of the objects. Direction sets leading to better reconstructions with the original phantom, lead to better results with the altered phantoms as well. This means that slightly distorted objects have the same – or at least similar – ideal projection directions as original objects, and this phenomenon can be exploited in the examination of objects by discrete tomography.

Finally, we should note that the above results were only tested for small modifications of the phantoms. In this case the extension of the changes was 4-5% of the

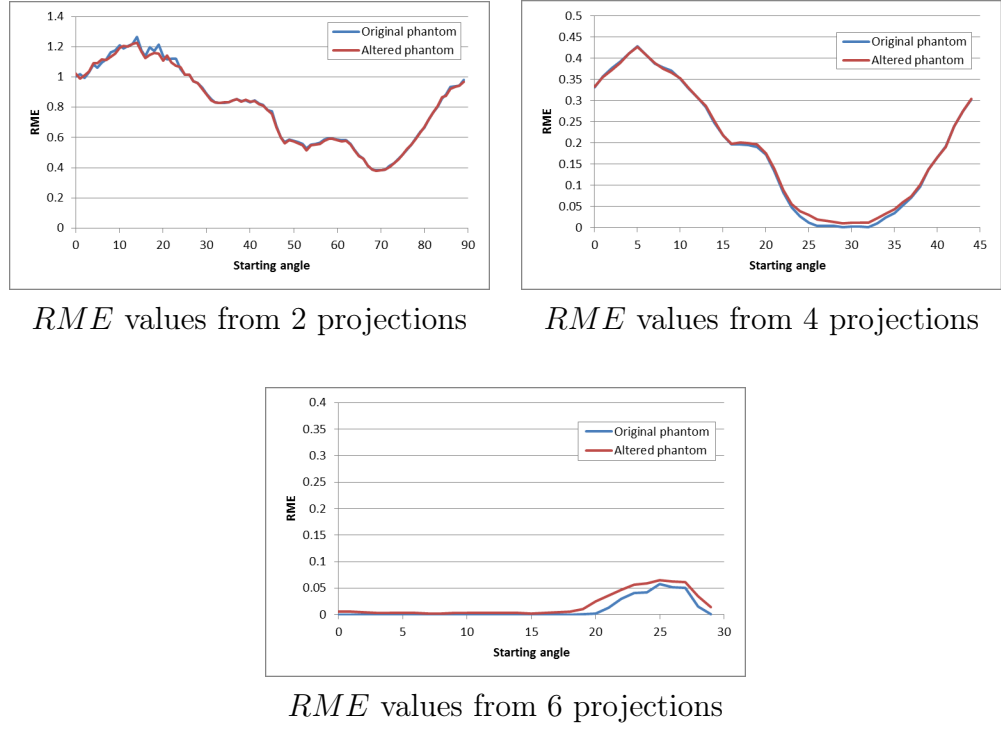


Figure 2.17: *RME* plots for the reconstruction of the altered phantoms according to the starting angle. Reconstructions of the phantom of Figure 2.5a were performed by the DC algorithm with equiangular projections sets containing 2, 4, and 6 projections.

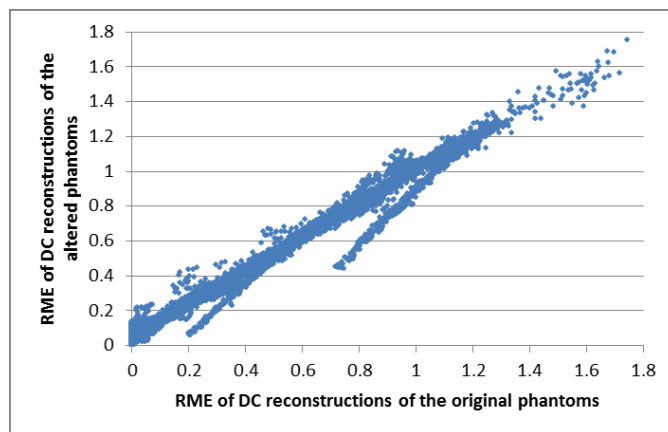


Figure 2.18: Correspondence between the *RME* values of reconstructions of the original, and the slightly modified phantoms. Points coordinates are determined by the *RME* values of the results of two corresponding reconstructions. The diagrams hold data for all the 22 binary phantom images.



Figure 2.19: Rotation invariant phantom.

size of the object. If the distortion of the object is bigger, then the change in the direction-dependency characteristic will get more significant, and after a certain point one can arrive to an entirely different object with different ideal projection directions.

2.4.6 Rotation invariant images

The test data of the above examinations also showed small regularities in the direction-dependencies, which were not caused by the shape of the objects. We found that some of the projection angles lead to slightly better results than expected, in a large number of reconstructions. For this reason, we also decided to examine the direction-dependency of an object that ought to be rotation invariant.

We constructed the phantom of Figure 2.19 that is a rasterized image of a ring with a disk inside. The centre of the disk and the ring are placed into the middle of the image. With an infinite resolution, this phantom should be rotation invariant. However, this is not the case, since we produced this image in a resolution of 256×256 pixels.

If an object is rotation invariant then all its equiangular projection sets should lead to the same results. Therefore, we produced the equiangular projection sets of the phantom of Figure 2.19, and for each number of projections simply plotted the *RME* values according to the number of projections. Two such diagrams can be seen in Figure 2.20.

Examining the curves of Figure 2.20 one can observe an interesting phenomenon. The curves show, that the reconstruction of the phantom from different directions are of different quality. It is clear, that even this phantom is for some degree dependent on the choice of projections, however it was designed to be rotation invariant.

The explanation of this can be found in the formulation of the reconstruction problem. The reconstruction algorithms assume that the object to be reconstructed

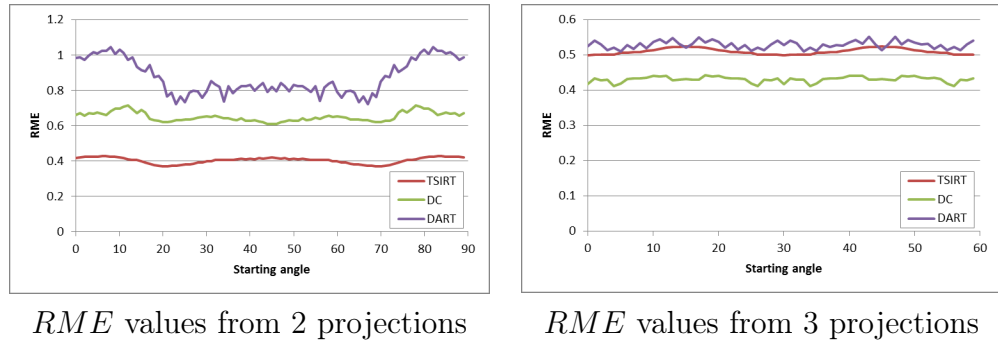


Figure 2.20: RME value plots of the rotation invariant phantom according to the starting angle.

is represented on a discrete image on the two-dimensional integer lattice. Also, the projection values are determined as the integrals of the image along straight lines. As we rotate the projection sets around the phantom images, we get different projection coefficient matrices, containing different values. These slightly different projection matrices hold different information of the projection geometry, therefore we will get different results.

In an extreme case of this discretized, grid based representation of the images one can even formulate projection geometries those make the exact reconstruction possible from only one projection. Although, the problem is not so drastic in the currently applied model, it still brings false information to the projection data due to a side effect of using a discrete model.

The strength of this phenomenon was the most notable with an extremely low number of (2 to 3) projections, but even in this case it was negligible compared to the direction-dependency of other objects that keeps the previous results valid. Later, as we increased the number of projections this effect of the discretization became more and more negligible. Still, reconstruction algorithms which minimize this effect and are not influenced by false data coming from the projection geometry used, might be of use in practical applications, and development of such methods is already present in the literature (see, e.g., [53]).

2.5 Possible applications

The direction-dependency of objects can also be taken into consideration in practical applications for implementing better, and more robust reconstruction procedures. In industry, there is often a need to get information about the interior of objects (industrial parts) in a non-destructive way, i.e., without damaging the object itself. This process is called *non-destructive testing* (*NDT*). In these applications the information about the object is usually collected by transmission tomography using X-rays or neutron rays to form the projections. Since the acquisition of such

projections can be very expensive and time-consuming, it is important to keep the number of projections as low as possible. If the object is made of homogeneous material then one approach to achieve this is to apply binary tomography for the reconstruction [1, 16, 40].

A frequent task in NDT is to determine the differences between the studied object and a given blueprint image. One places the object into the scanner, forms its projections from a few directions, and applies a (binary) reconstruction method to obtain an image from the object. Finally, the difference between the blueprint and the reconstructed image is measured according to an arbitrary similarity metric. Since the blueprint is available in advance, we can simulate its projections in arbitrary directions, and seek the ideal projection directions with the *EquiAng*, *Greedy*, or *AltAng* projection selection strategies in order to characterize the blueprint image from the viewpoint of direction-dependency. This information turns out to be essentially useful in several scenarios of NDT.

If there is a reference mark on both the benchmark and the studied object, then it is possible to place this latter one with a rotation of arbitrary known degree into the scanner. From the ideal projection angles of the blueprint, we know when the best reconstruction quality can be achieved – we simply have to seek the minimum of the *RME* values of the simulated projection sets. This determines how (i.e., in which direction) to place the test object into the scanner to have the most accurate reconstruction from the available number of projections. Since the difference between *RME* values of projection sets taken from similar angles is small, it is sufficient to place the object with only an approximately exact orientation as the minimal *RME* value suggests. Also, from the experiments of Section 2.4.4 and Section 2.4.5 we know that the noise on the projections, or the small distortions of the object will not considerably change the directions of the ideal projections.

On the other hand, if there is no mark on the studied object, then it might be placed with an unknown rotation into the scanner. Again, from the dependency function of the blueprint image we can predict how sensitive our test will be to this rotation. In addition, from the worst equiangular reconstructions of the blueprint we can deduce how many projections are needed to keep the maximal error acceptably low, i.e., to be sure that the effect of rotation will be eliminated. If it is impossible to acquire so many projections, then from the minimal error we can estimate the quality of the best reconstruction possible from the given number of projections. This information can also be used to check whether a reconstruction algorithm is suitable for the given industrial test. If the error of the best reconstruction is still high, then we might classify perfect objects as damaged ones and vice versa.

2.6 Summary

We performed a series of tests to examine the direction-dependency of binary reconstructions. In the case of using equiangular projections we revealed that the rotation of the objects of study influences the quality of reconstructed results, and one can get better reconstructions by finding the right orientation of the object. We also observed that further improvement can be reached by using non-equangular projection sets which can be aligned to the geometric properties of the objects more accurately.

Further examinations showed, that the direction-dependency is the property of the objects of study themselves, which can be taken into account when designing the observation of objects. We found that the directions of the ideal projections are independent from the reconstruction algorithm used, and the distortions of the projection data. Furthermore, similar objects have similar direction-dependency characteristics, i.e., the projections with the same directions would result in outputs of similar quality, and also projections with angles close to each other hold similar information content for the reconstruction.

All these properties described above make the direction-dependency of objects a consistent phenomenon which can be exploited in practical applications for minimizing the number of required projections, or increasing the accuracy of reconstructions is discrete tomography.

The findings of this research have been published in two conference proceedings [59, 60], and two journal papers [61, 62]. Also, based on these results, a new research direction arose in the field of discrete tomography, called *In-Situ tomography*, where the projection angles are adjusted to the object of study during the data acquisition, without a blueprint image [10]. Finally, up to date, there have been three independent references to the findings of the results [21, 28, 46].

Chapter 3

An Energy Minimization Reconstruction Algorithm for Multivalued Discrete Tomography

3.1 Introduction

Discrete reconstruction algorithms have to cope with various difficulties of tomography. The reconstruction problem commonly requires the restoration of the structure of an object from incomplete projection data, possibly affected by errors coming from the discrete formulations of the reconstruction problem and stochastic noise affecting the projection acquisition process. Also, the general case of discrete tomography is proved to be NP-hard, and efficient algorithms providing perfect results can only be defined for some special cases [2, 18, 23, 24, 25, 29].

There is a variety of different approaches to overcome these problems. Some methods provide heuristic strategies for discretizing the results of continuous reconstructions [11, 12, 48], some other techniques reformulate the task as an optimization problem that can be solved by different meta-heuristics [6, 7, 8, 44]. In this chapter we describe a reconstruction algorithm, that we developed for the general case of DT, and that can perform the reconstruction by minimizing a suitably constructed energy function.

The basic idea behind this method is based on the DC algorithm of Section 1.2.3. Unfortunately, the DC method is only capable of reconstructing binary images, and the aim was to provide a more general algorithm for multivalued discrete tomography, that is not restricted to the binary case, and can compete with the current cutting-edge reconstruction algorithms in the literature. For this, we made significant modifications to the original concept of the DC algorithm. We provided a new energy function that can handle more than two intensities in the reconstruc-

tion, and we also designed a novel optimization strategy that can approximate a reconstruction by an adaptive weighting in a gradient descend process.

3.2 The proposed method

The algorithm uses the algebraic formulation of the reconstruction problem described in Section 1.1. Here, the task is equivalent to solving a system of equations in a discrete domain

$$\mathbf{Ax} = \mathbf{b}, \quad \mathbf{A} \in \mathbb{R}^{n^2 \times m}, \quad \mathbf{x} \in \Phi^{n^2}, \quad \mathbf{b} \in \mathbb{R}^m, \quad (3.1)$$

where $\Phi = \{\phi_0, \dots, \phi_c\}$ is a set of possible intensities on the reconstruction such that $\phi_0 < \phi_1 < \dots < \phi_c$, and $\phi_0 = 0$ and $\phi_c = 1$.

Based on the equation system, we formulated the task as the minimization of an energy function which has its global minima in the correct reconstructions.

3.2.1 The energy function

Using the above notation the energy function can be written as the sum of two terms

$$\mathcal{E}(\mathbf{x}) = f(\mathbf{x}) + \mu \cdot g(\mathbf{x}), \quad \mathbf{x} \in [\phi_0, \phi_c]^{n^2}, \quad (3.2)$$

where $f(\mathbf{x})$ is a function formulating the CONTINUOUS RECONSTRUCTION problem, and $g(\mathbf{x})$ is a discreteness prior weighted with a μ constant.

In more detail, the first function has a form

$$f(\mathbf{x}) = \frac{1}{2} \cdot \|\mathbf{Ax} - \mathbf{b}\|_2^2 + \frac{\gamma}{2} \cdot \mathbf{x}^T \mathbf{Lx}, \quad (3.3)$$

with \mathbf{L} being a matrix such that

$$\mathbf{x}^T \mathbf{Lx} = \sum_{i=1}^{n^2} \sum_{j \in N_4(i)} (x_i - x_j)^2 \quad (3.4)$$

and $N_4(i)$ giving the set of pixel indexes 4-adjacent with the i -th pixel. Informally, $f(\mathbf{x})$ consists of an $\|\mathbf{Ax} - \mathbf{b}\|_2^2$ projection correctness (or data fidelity) term, and an $\mathbf{x}^T \mathbf{Lx}$ smoothness prior, that is lower if the reconstructed image contains larger homogeneous regions.

The second, $\mu \cdot g(\mathbf{x})$, term of (3.2) is a formulation of the discreteness, which propagates solutions containing values only from the Φ predefined set of intensities. Here, $\mu \geq 0$ is a constant weight that can be used to balance between the two separate parts of the energy function, and $g(\mathbf{x})$ is constructed to take its minimal

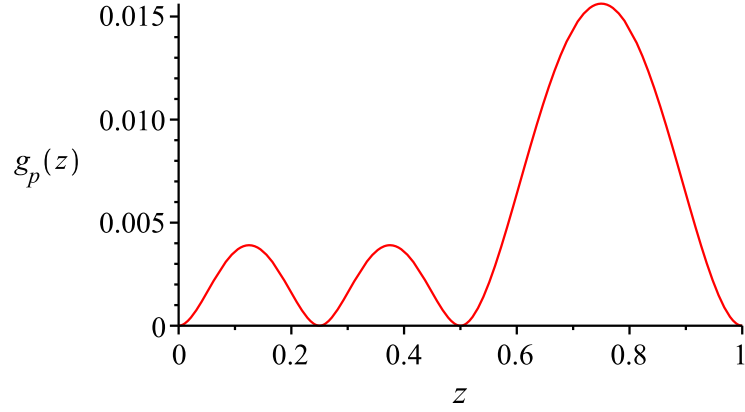


Figure 3.1: Example of the $g_p(z)$ one-variable discretization function with intensity values $\Phi = \{0, 0.25, 0.5, 1\}$.

$g(\mathbf{x}) = \mathbf{0}$ values at discrete solutions (i.e., when $\mathbf{x} \in \Phi^{n^2}$) and higher positive values otherwise. The $g(\mathbf{x})$ discretizing function is given in the form

$$g(\mathbf{x}) = \sum_{i=1}^{n^2} g_p(x_i), \quad (3.5)$$

where g_p is a one-variable function composed of a set of forth-grade polynomial functions, defined over the intervals of Φ in the way

$$g_p(z) = \begin{cases} \frac{[(z-\phi_{j-1}) \cdot (z-\phi_j)]^2}{2 \cdot (\phi_j - \phi_{j-1})^2}, & \text{if } z \in [\phi_{j-1}, \phi_j] \text{ for each } j \in \{1, \dots, c\}, \\ \text{undefined}, & \text{otherwise.} \end{cases}$$

An illustration of a g_p function can be seen in Figure 3.1. Informally, this discretization function assigns a small energy to each pixel if its value in the reconstruction is close to an element of Φ , and a higher energy (increasing with the distance) otherwise.

3.2.2 The optimization process

The optimization process in the proposed method is based on breaking the energy function (3.2) into two parts, and prioritizing between them. The first part is given by the term $f(\mathbf{x})$ defined in (3.3), i.e., the two terms responsible for projection correctness and smoothness. The other part is provided by the $\mu \cdot g(\mathbf{x})$ discretization term.

The formal description of the algorithm uses the following notations.

- \mathbf{A} , \mathbf{b} , \mathbf{x} , n , and Φ are, respectively, the projection matrix, the vector of projection values, the vector of image pixels, the number of rows and columns on the image, and the set of expected pixel intensities, as defined in Section 1.1,

- $\frac{\partial g}{\partial x_i} \Big|_{\mathbf{x}=\mathbf{x}^{(k)}}$ denotes the partial derivative of the discretization term with respect to the variable x_i , i.e., the i -th pixel of the reconstructed image, evaluated at the $\mathbf{x}^{(k)}$ position,

$$\frac{\partial g}{\partial x_i} \Big|_{\mathbf{x}=\mathbf{x}^{(k)}} = \frac{(x_i - \phi_{j-1})(x_i - \phi_j)(2 \cdot x_i - \phi_{j-1} - \phi_j)}{(\phi_j - \phi_{j-1})^2}, \text{ if } x_i \in [\phi_{j-1}, \phi_j], \quad (3.6)$$

- $G_{0,\sigma}(z)$ is an unnormalized Gaussian function with 0 mean and σ deviance, that is

$$G_{0,\sigma}(z) = e^{-\left(\frac{z^2}{2\sigma^2}\right)}, \quad (3.7)$$

- $\gamma \geq 0$, $\mu \geq 0$, and $\sigma \geq 0$ are predefined constants controlling in the energy function, respectively, the weight of the smoothness term, the weight of the discretization term, and the deviance of the Gaussian function applying the adaptive weighting of the discretization,
- λ is an upper bound of the largest eigenvalue of the matrix $(\mathbf{A}^T \mathbf{A} + \gamma \mathbf{L})$,
- \mathbf{L} is a matrix representing the smoothness prior as described in (3.4). Note, that the $\mathbf{L}\mathbf{x}$ multiplication of the \mathbf{x} vector of pixel values with the \mathbf{L} matrix is equivalent to the application of a discrete Laplace operator [31] in the image, i.e., the convolution with the kernel

$$K = \begin{bmatrix} 0 & -2 & 0 \\ -2 & 8 & -2 \\ 0 & -2 & 0 \end{bmatrix}.$$

For obtaining the result, the optimization method uses an adaptive and automatic pixel-based weighting of the discretization term. The detailed description of the algorithm is given in Algorithm 6. This algorithm will be referred to as MLEM.

The optimization process establishes a connection between the two parts of the energy function (i.e., the formulation of the continuous reconstruction problem, and the discretization term), and assumes that the first part has a higher priority. The first consideration will be to find a reconstruction that satisfies the projections, while keeping in mind to look for a discrete result, if possible.

Structurally, the algorithm is based on optimizing the energy function with a projected subgradient method, while applying an automatic weighting between the two terms of the energy function. In each iteration step of the optimization process, one can calculate the gradient of the $\|\mathbf{A}\mathbf{x}^{(k)} - \mathbf{b}\|_2^2$ projection correctness term in the energy function by computing the $\mathbf{A}^T(\mathbf{A}\mathbf{x}^{(k)} - \mathbf{b})$ vector. For each pixel, this vector explicitly contains an estimation of correctness of the pixel in the current

Algorithm 6 MultiLevel Energy-Minimization algorithm for DT

Input: \mathbf{A} projection matrix; \mathbf{b} expected projection values; $\mathbf{x}^{(0)}$ initial state; $\gamma, \mu, \sigma \geq 0$ predefined constants; Φ list of expected intensities; ϵ step size bound; k_{max} maximal iteration count.

- 1: $\lambda \leftarrow \lambda_{max}(\mathbf{A}^T \mathbf{A} + \alpha \cdot \mathbf{L})$
 {calculate an upper bound for the eigenvalues of $(\mathbf{A}^T \mathbf{A} + \alpha \cdot \mathbf{L})$ }
- 2: $k \leftarrow 0$
- 3: **repeat**
- 4: $\mathbf{v} \leftarrow \mathbf{A}^T(\mathbf{A}\mathbf{x}^{(k)} - \mathbf{b})$
 {calculate the gradient of the projection correctness term}
- 5: $\mathbf{w} \leftarrow \mathbf{L}\mathbf{x}^{(k)}$ {calculate the gradient of the smoothness term}
- 6: **for** each $i \in \{1, 2, \dots, n^2\}$ **do**
- 7: $y_i^{(k+1)} \leftarrow x_i^{(k)} - \frac{v_i + \gamma \cdot w_i + \mu \cdot G_{0,\sigma}(v_i) \cdot \frac{\partial g}{\partial x_i} \big|_{\mathbf{x}=\mathbf{x}^{(k)}}}{\lambda + \mu}$
- 8: $x_i^{(k+1)} \leftarrow \begin{cases} \theta_0, & \text{if } y_i^{(k+1)} < \phi_0, \\ y_i^{(k+1)}, & \text{if } \phi_0 \leq y_i^{(k+1)} \leq \phi_c, \\ \theta_c, & \text{if } \phi_c < y_i^{(k+1)}. \end{cases}$
- 9: **end for**
- 10: $k \leftarrow k + 1$
- 11: **until** $\|\mathbf{x}^{(k+1)} - \mathbf{x}^{(k)}\|_2^2 < \epsilon$ or $k > k_{max}$
- 12: Apply a thresholding and output $\mathcal{T}_\Phi(\mathbf{x}^{(k)})$ to gain fully discrete results.

state according to the projections (the greater this value is the more responsible the pixel is for causing incorrect projections). By applying a Gaussian function on these values we can get a weight, that is smaller when the corresponding pixel needs further adjustments, and greater if the projection rays connected to that specific pixel are more or less satisfied. Weighting the discretization with this value calculated from the gradient of the projection correctness, leads to an automatic adjustment of the discretizing term for each pixel, omitting it when the projections are not satisfied, and slowly increasing its effect as the pixel values get closer to an acceptable reconstruction.

In practice, this means that the method starts with an arbitrary initial state, and first approximates a continuous reconstruction based on the given set of projections. Later, as the projections of the intermediate image get closer to the described vectors, the automatic weighting of the discretizing term begins to increase for each pixel. Thus, the pixels will be slowly steered towards discrete values of Φ . The maximal strength of the discretizing term, and the speed at which the discretizing term gets strengthened during the process, are controlled by the μ and σ parameters, respectively.

Note, that it is possible that the process will get stuck in a local minimum of the energy function. In this case the iteration will stop in a semi-continuous solution, where some pixels are properly discretized, and the rest of them are left

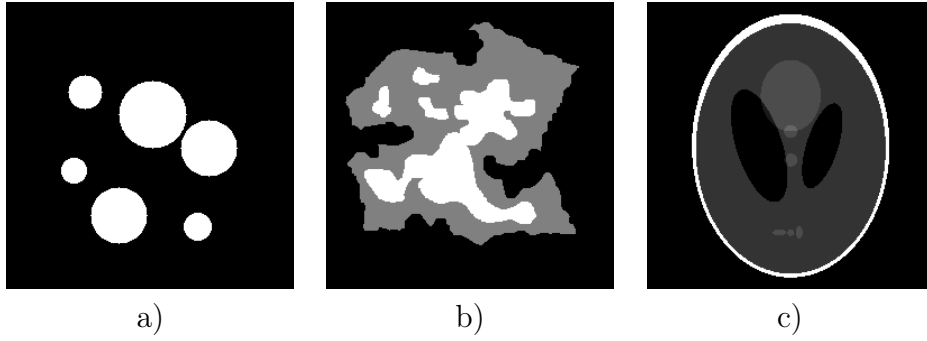


Figure 3.2: Some of the software phantoms used for testing. a) a binary image; b) a multivalued image from [11]; c) the well-known Shepp-Logan head phantom (see, e.g., page 53 of [39]).

continuous because the projection correctness did not allow a full discretization. Thus, after the optimization process, the discretization is completed by applying a segmentation to the final iteration state $\mathbf{x}^{(k)}$, to gain a fully discrete reconstruction result. This is done by simply using the $\mathcal{T}_{\Phi}(\mathbf{x}^{(k)})$ thresholding operation (1.9).

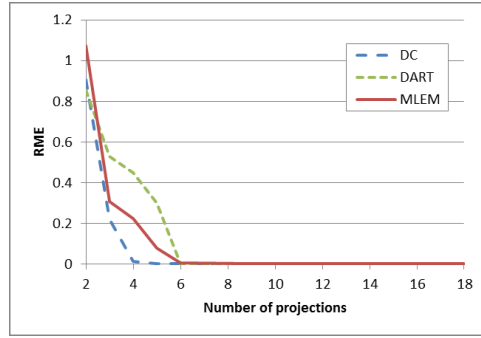
3.3 Experimental results

We conducted experiments to compare the proposed method to other reconstruction algorithms defined in Section 1.2. On one hand, on binary images, we performed experiments with the DC algorithm, to see how the performance of the original and the new algorithms are related to each other. Unfortunately, due to the limitations of the DC algorithm (as it is not suited for multivalued discrete tomography), we could only do this evaluation for binary images. Also, we ran tests with the DART in order to compare the reconstruction of multivalued images with.

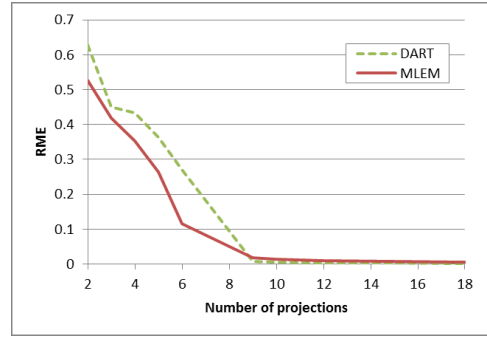
We performed the evaluations by using the 25 phantom images of Appendix C. Three highlighted phantoms can be seen in Figure 3.2. The reconstructions were performed from projection sets containing 2 to 18 projections, distributed equiangularly on the half circle. Assuming that the projection with 0° angle corresponds to the vertical rays, these equiangular projection sets (in accordance with the notation of (2.2)) can be defined for each p number of projections with the angle set

$$S(p, 0^\circ) = \left\{ 0^\circ + i \cdot \frac{180^\circ}{p} \mid i = 0, \dots, p-1 \right\}. \quad (3.8)$$

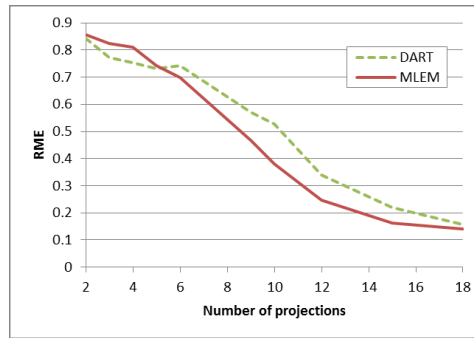
In the tests, the parameters of the DART and DC algorithms were mostly set from the literature, with slight adjustments to assure the best performance of all the methods. The parameters of the DC algorithm were $\mu_{\Delta} = 0.1$, $\gamma = 2.5$, $\epsilon_{in} = 0.1$ and $\epsilon_{out} = 0.01$.



Results for Figure 3.2a



Results for Figure 3.2b



Results for Figure 3.2c

Figure 3.3: *RME* values of the compared DC, DART, and MLEM reconstruction algorithms, plotted according to the number of projections.

With the DART, 10 iterations of the SIRT were used for producing the continuous reconstructions, we applied the same smoothing kernel as described in Section 2.3, and used the stopping criteria $k_{\Delta} = 10$, and $k_{max} = 500$.

For the MLEM method, $\gamma = 2.5$, $\mu = 20$, $\sigma = 1$, $\epsilon = 0.001$, $k_{max} = 5000$ values were used and in the \mathbf{x}^0 initial solution all the x_i^0 positions were set to the same value in the middle of the range of possible intensities (i.e., $x_i^0 = (\phi_c - \phi_0)/2$, for all $i \in \{1, \dots, n^2\}$). With these parameter settings we experimentally found the algorithm to be convergent in all the test cases.

We implemented all three algorithms in C++ with GPU acceleration using the Nvidia CUDA C sdk. The computation was performed on a PC, with an Intel Q9500 CPU, and an Nvidia Geforce GTS250 GPU.

The reconstructed results were compared visually, and by using the Relative Mean Error (*RME*) measurement defined in (1.13). Also, we measured the computation times of the algorithms in each case. Some of the numerical results can be seen in Table 3.1, while Figure 3.3 shows the same data graphically in diagrams, and Figure 3.4 and Figure 3.5 give some examples of the reconstructed results. The given data is only a representative sample from the tests, but the findings are general for all the results.

Based on the results, we deduced the following. In case of using very few pro-

Table 3.1: Reconstruction error and computation time of the compared algorithms, reconstructing the phantoms of Figure 3.2. The error measurement is calculated by the RME value, and the computational time is given in seconds. Reconstructions of the DC algorithm could only be performed on binary test images. In each row, the best result is highlighted in bold.

Figure 3.2a						
	DC		DART		MLEM	
P. Num.	RME	Time (s)	RME	Time (s)	RME	Time (s)
2	0.907	12.1	0.856	6.6	1.074	10.1
3	0.220	12.4	0.529	5.4	0.308	11.2
4	0.012	13.6	0.449	8.0	0.224	11.8
5	0.003	12.5	0.299	9.5	0.079	12.7
6	0.002	8.1	0.002	2.7	0.008	7.6
9	0.002	6.5	0.000	0.8	0.003	4.6
12	0.000	7.2	0.000	0.9	0.001	4.8
15	0.000	8.7	0.000	1.2	0.001	5.8
18	0.000	8.7	0.000	0.9	0.001	5.8

Figure 3.2b						
	DC		DART		MLEM	
P. Num.	RME	Time (s)	RME	Time (s)	RME	Time (s)
2	-	-	0.629	6.7	0.527	10.4
3	-	-	0.451	8.0	0.419	11.4
4	-	-	0.434	8.6	0.354	12.2
5	-	-	0.364	9.4	0.264	13.2
6	-	-	0.270	10.2	0.116	13.8
9	-	-	0.007	4.5	0.019	15.6
12	-	-	0.004	14.9	0.010	11.6
15	-	-	0.003	2.3	0.008	11.6
18	-	-	0.001	21.3	0.006	10.9

Figure 3.2c						
	DC		DART		MLEM	
P. Num.	RME	Time (s)	RME	Time (s)	RME	Time (s)
2	-	-	0.844	6.7	0.857	9.3
3	-	-	0.773	8.2	0.825	6.0
4	-	-	0.753	8.8	0.810	8.0
5	-	-	0.733	9.7	0.742	10.2
6	-	-	0.741	10.2	0.700	12.7
9	-	-	0.570	12.6	0.468	14.7
12	-	-	0.339	14.5	0.248	11.4
15	-	-	0.220	18.0	0.163	8.6
18	-	-	0.157	20.8	0.140	8.0

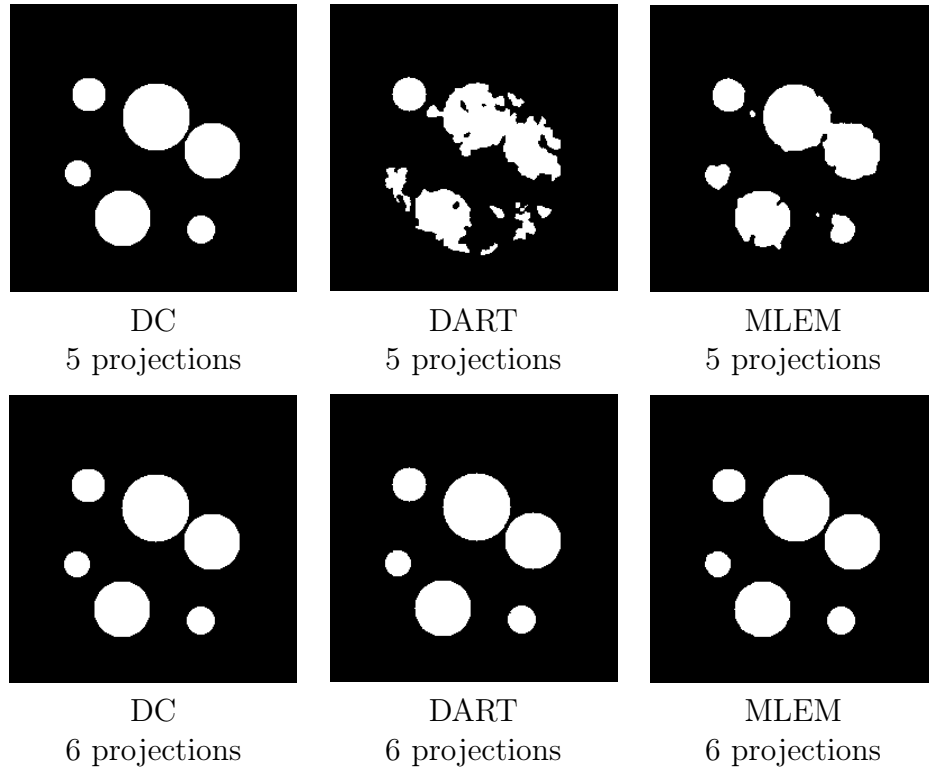


Figure 3.4: Reconstructions of a binary phantom (Figure 3.2a), produced by the DC, DART, and MLEM algorithms, from projection sets containing different numbers of projections.

jections (i.e., 2-3 projections for simple images like the phantoms of Figure 3.2a-b, and up to 5-6 projections for more complex ones like Figure 3.2c), there was obviously not enough information for accurate reconstructions. Usually, the DART produced the best results, but this seems to be irrelevant since the reconstruction error is unacceptably high.

When increasing the number of projections, the amount of information in the data was also increasing and the results provided by the algorithms began to improve as well. The results of the optimization based algorithms (DC and MLEM) improved faster with an increasing number of projections. Therefore, these two algorithms gave accurate reconstructions from fewer projections than the DART (see, Table 3.1). Later, when there were even more projections with more than sufficient information for an accurate reconstruction, again the DART provided the best results, by performing slightly better than the other two methods.

Comparing the energy minimization based methods, on binary images the DC algorithm worked better than the MLEM. The DC algorithm is specialized for binary tomography, and aims a full binarization in the optimization process. The drawback is that the original DC algorithm is not capable of performing multivalued discrete tomography at all.

On the other hand, the proposed method needs a different approach for having


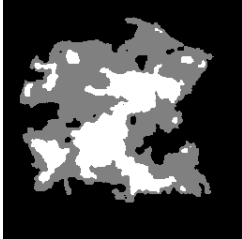



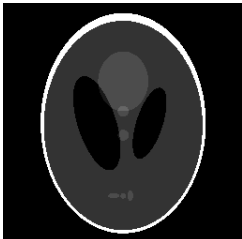

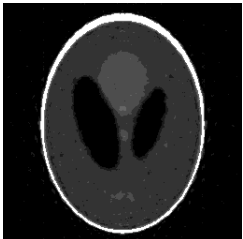
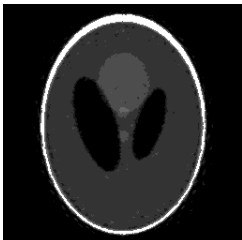

Original phantom	# projections	DART	MLEM
	6		
			
	9		
	15		
	18		

Figure 3.5: Reconstructions of multivalued phantoms (Figure 3.2b-c) produced by the DART and MLEM algorithms, from projection sets containing different numbers of projections.

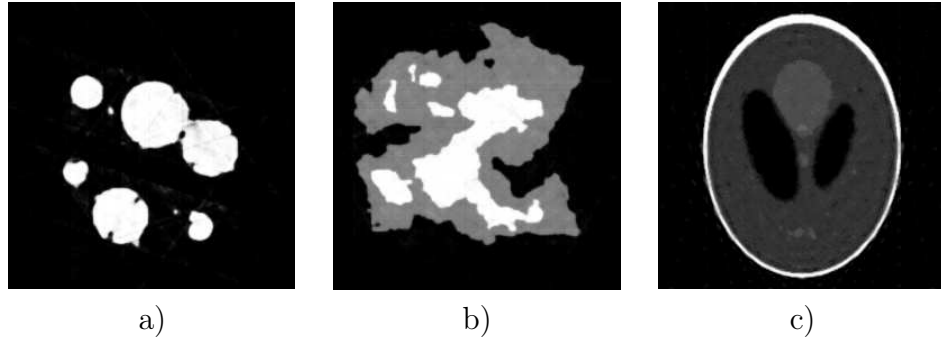
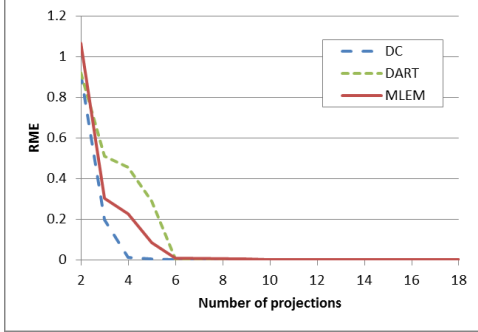


Figure 3.6: Continuous results of the MLEM algorithm, without the final thresholding. The images a), b) and c) were reconstructed from 5, 6, and 15 projections, respectively.

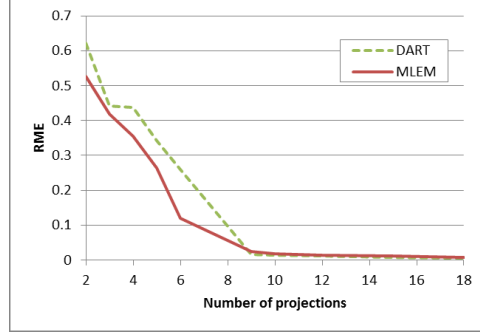
the generality to be able to reconstruct multivalued images, and it only makes an approximate discretization. This means that in a later state of the energy minimization process – without the final thresholding – the output is a semi-discrete, semi-continuous result. This intermediate result is produced by taking into account that we are looking for a discrete solution, but it still contains some uncertainty of the values (some of the examples of such results can be seen in Figure 3.6). This kind of soft discretization is necessary for the multivalued reconstruction in our method, but it reduces the accuracy of the algorithm on binary images.

In addition, we also performed tests by distorting the projection data with the additive Gaussian random noise described in Section 1.4. As before, we applied the noise levels set by $\sigma \in \{0.5, 1.5, 5.0\}$ values which meant 1.25%, 3.75% and 12.5% noise strengths compared to the projection data. We compared the results of the three reconstruction algorithms by plotting the *RME* values according to the number of projections. The MLEM reconstruction method proved to be robust in the tests against noise-affected projection data. In case of low projection counts, with an increasing strength of noise we found that the MLEM algorithm provided much better results than the other two methods. The robustness might be explained by the proposed optimization process and discretizing function. As mentioned above, the MLEM performs a soft discretization and at the end of the optimization process the pixel values are allowed to take continuous results. This soft discretization allows the pixel values to absorb a small degree of noise and thus projection errors do not have to accumulate in falsely classified pixels. Also, at the end of the process the pixel values are thresholded, and the absorbed noise will not show up in the final reconstruction. A sample of the resulted diagrams can be seen in Figure 3.7.

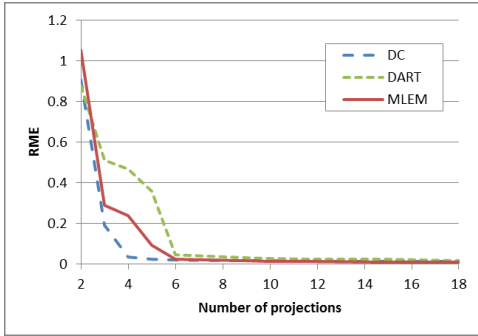
Although, with a high projection count (which meant much more projections than it was necessary for an accurate reconstruction) the optimization-based algorithms – the DC and the MLEM – gave slightly worse results, while the DART



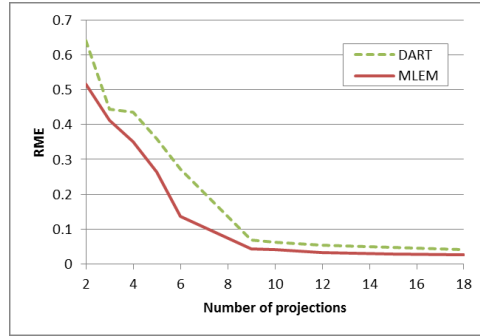
Results of Figure 3.2a
with noise level $\sigma = 0.5$



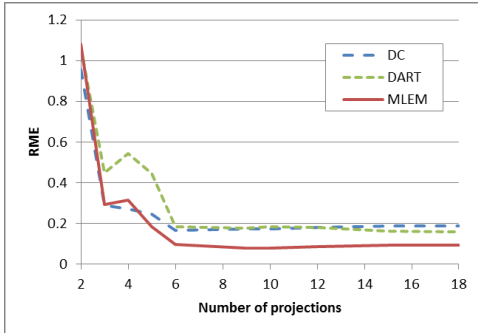
Results for Figure 3.2b
with noise level $\sigma = 0.5$



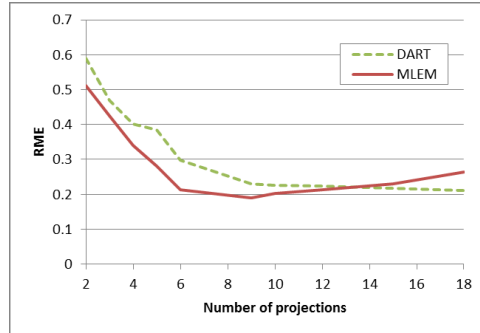
Results of Figure 3.2a
with noise level $\sigma = 1.5$



Results for Figure 3.2b
with noise level $\sigma = 1.5$



Results of Figure 3.2a
with noise level $\sigma = 5.0$



Results for Figure 3.2b
with noise level $\sigma = 5.0$

Figure 3.7: RME values of reconstruction algorithms from projection data affected by noise, plotted according to the number of projections.

could reach further small improvements of the quality.

Finally, regarding the computational time of the algorithms, we found that depending on the conditions of the reconstruction and the image processed, one or another algorithm gave results faster than the other ones. Still, in general, the time requirements showed to be similar.

In summary, the performance of the algorithms were similar in the tests. All three methods can yield highly accurate reconstructions. Nevertheless, we found that the DC and MLEM methods gave slightly better results when the reconstructions were performed from a low number of projections, and the proposed MLEM method proved to be highly robust against noise in the projections. On the other hand, the results of DART were better in case of using a higher number of projections. This diversity makes all the algorithms valuable.

3.4 Summary

We proposed a new algorithm for multivalued discrete tomography, that is based on the minimization of a suitably constructed energy function. We compared this method to two existing reconstruction algorithms from the literature by performing experimental tests on a set of software phantoms. The results show that, in the case of multivalued discrete tomography, the proposed method finds an accurate result from less projections than the other tested algorithms, and it is highly robust when the projection data is affected by a random noise. Therefore, it should be considered as a useful reconstruction technique.

Also note, that the proposed optimization process did not exploit the fact that the energy function is constructed for discrete reconstruction problems, and it could be used as a meta-heuristic in different cases of optimization.

The results of this chapter were published in two conference proceedings [63, 64].

Chapter 4

Local and Global Uncertainty in Binary Reconstructions

4.1 Introduction

In many cases of binary tomography, the amount of projection data can be insufficient for an accurate reconstruction. This kind of incomplete information makes it essential to have methods capable of assessing and evaluating the projection data from the viewpoint of completeness and reliability. In [9] the authors gave an upper bound on the variability of binary reconstructions from a given projection set, that determines a bound for the expected accuracy of the reconstructed results.

Here, we give a probabilistic description of the uncertainty problem in the field of binary tomography, and provide a method that can approximate the local uncertainty map in binary reconstructions. By this method, one can gain information on how the projection data determines each part of the reconstructed image separately, and estimate the expected accuracy of the reconstructed parts. This measurement is currently unique in the literature, as to the best of our knowledge related work only exist for measuring the overall reliability of reconstructions.

We also introduce a formula to summarize the local uncertainties into a global measure, that describes the overall information content of a projection set. Finally, we provide an experimental validation of the described methods, and give some possible applications.

4.2 The uncertainty problem

As before, we will use the algebraic formulation of the BINARY RECONSTRUCTION problem defined in Section 1.1, and assume that the object to be reconstructed is represented on an $n \times n$ sized image, and the task can be represented by a system

of equations

$$\mathbf{Ax} = \mathbf{b}, \quad \mathbf{A} \in \mathbb{R}^{n^2 \times m}, \quad \mathbf{x} \in \{0, 1\}^{n^2}, \quad \mathbf{b} \in \mathbb{R}^m. \quad (4.1)$$

From a mathematical point of view, the above formulation of the BINARY RECONSTRUCTION problem defines a search space of n^2 dimensions (a dimensionality that equals to the number of pixels). In this search space, the correct reconstructions lie in the intersection of an \mathcal{H} hyperplane determined by the $\mathbf{Ax} = \mathbf{b}$ equation system, and a $\mathcal{B} = \{0, 1\}^{n^2}$ set of binary points.

Assume, that only the – yet unknown – original image of the object of study is accepted as a correct solution. If the projections do not determine a unique reconstruction, then the correct result can be regarded as a random element of the set of reconstructions with the correct projections. In this way, each binary point of $\mathbf{x} \in \mathcal{B}$ can be assigned a

$$P(\mathbf{x} | \mathbf{A}, \mathbf{b}) \quad (4.2)$$

probability of that reconstruction being the correct one. Furthermore, it is possible to calculate for each i -th pixel, the probability of that pixel taking a value 1 or 0 in the correct solution, as

$$P(x_i = 1 | \mathbf{A}, \mathbf{b}) = \sum_{\substack{\mathbf{y} \in \mathcal{B} \\ y_i = 1}} P(\mathbf{y} | \mathbf{A}, \mathbf{b}), \quad (4.3)$$

and

$$P(x_i = 0 | \mathbf{A}, \mathbf{b}) = 1 - P(x_i = 1 | \mathbf{A}, \mathbf{b}). \quad (4.4)$$

Also, the entropy on each pixel can be determined as

$$\begin{aligned} H(x_i) = & -P(x_i = 0 | \mathbf{A}, \mathbf{b}) \cdot \log_2(P(x_i = 0 | \mathbf{A}, \mathbf{b})) - \\ & -P(x_i = 1 | \mathbf{A}, \mathbf{b}) \cdot \log_2(P(x_i = 1 | \mathbf{A}, \mathbf{b})), \end{aligned} \quad (4.5)$$

which will be regarded as the measurement of the uncertainty of the pixel. This measure is independent from the object of study itself and it only corresponds to the information content in the projections. The pixels with a high entropy are ambiguous, and their values cannot be determined for certain, based on the projections.

The above measures can be calculated for all the pixels of the whole reconstructed image as well. The probabilities of (4.3) give a *probability map* showing for each pixel the likelihood of that pixel to take a value of 1, and the values of (4.5) provide an *uncertainty map* describing the local uncertainty of the reconstruction.

In the ideal case, the calculation of the probability-, and uncertainty-maps would be straightforward. The elements of the $(\mathcal{H} \cap \mathcal{B})$ intersection should have a $P(\mathbf{x} | \mathbf{A}, \mathbf{b})$ probability inversely proportional to the size of $(\mathcal{H} \cap \mathcal{B})$ – i.e., the

number of binary reconstructions satisfying the projections – and all other elements of $(\mathcal{B} \setminus \mathcal{H})$ have a probability of 0, that is,

$$P(\mathbf{x} | \mathbf{A}, \mathbf{b}) = \begin{cases} \frac{1}{|\mathcal{H} \cap \mathcal{B}|}, & \text{if } \mathbf{x} \in (\mathcal{H} \cap \mathcal{B}), \\ 0, & \text{otherwise.} \end{cases} \quad (4.6)$$

In this case, the probability and uncertainty maps could be determined by directly applying (4.3), (4.4), and (4.5). Unfortunately, the exponential size of the \mathcal{B} binary search space makes a direct approach impossible.

In practice, the task is even more complex. Binary reconstructions are performed by heuristic algorithms which only approximate one element of the set of solutions. This means that they can output results, which are placed only close to the \mathcal{H} hyperplane. Naturally, the closer a solution is to \mathcal{H} (i.e., the better it satisfies the projections) the higher its probability should be. Therefore, $P(\mathbf{x} | \mathbf{A}, \mathbf{b})$ should correspond to the chance for the reconstruction algorithms to find a specific \mathbf{x} solution.

This task is still too complex to be solved. However, it is possible to use a heuristic method to estimate the likelihood, that an algorithm should assign a 0 or 1 value to a pixel, and thus to approximate the uncertainty map. In the next section we will provide one such algorithm for approximating the probabilities of (4.3), and by this to approximate the local uncertainties of reconstructions.

4.3 Approximating local uncertainty in binary reconstructions

In Chapter 3, we described an algorithm for discrete tomography, that is capable of reconstructing images by minimizing an energy function. With some minor modifications, this method is also capable of approximating the pixel uncertainties of binary reconstructions, by producing a “least binary” result.

This modified algorithm minimizes an energy function of the form

$$\mathcal{E}(\mathbf{x}) = \frac{1}{2} \|\mathbf{Ax} - \mathbf{b}\|_2^2 + \mu \cdot g(\mathbf{x}) . \quad (4.7)$$

where \mathbf{A} , \mathbf{b} and \mathbf{x} are as defined in Section 1.1, $g(\mathbf{x})$ is a function holding information on the discreteness of the reconstruction, and μ is the weight of the discreteness prior. Here, the first $\|\mathbf{Ax} - \mathbf{b}\|_2^2$ term is a data fidelity, or projection correctness term, which takes its minima where the solution satisfies the projections, i.e., at the $(\mathcal{H} \cap \mathcal{B})$ intersections.

The $g(\mathbf{x})$ is a term representing some information on the discreteness of the

problem. In similar optimization based reconstruction methods (like the ones in [55, 63], and the MLEM algorithm of Chapter 3), this is a discretizing term taking its minimal values in discrete points. Here, we would rather call this term a discreteness prior and emphasize, that it is not necessary to propagate discrete solutions with it. In fact, with the different choice of $g(\mathbf{x})$ one can reach different effects on the result, and gain different kinds of extra information from the reconstructions. The formal description of the modified optimization process is given in Algorithm 7.

Algorithm 7 Energy-Minimization Algorithm for Discrete Tomography

Input: \mathbf{A} projection matrix; \mathbf{b} expected projection values; \mathbf{x}^0 initial state; $\mu, \sigma \geq 0$ predefined constants; ϵ step size bound; k_{max} maximal iteration count.

- 1: $\lambda \leftarrow$ an upper bound for the largest eigenvalue of the $(\mathbf{A}^T \mathbf{A})$ matrix.
 - 2: $\lambda \leftarrow \lambda_{max}(\mathbf{A}^T \mathbf{A})$ {calculate an upper bound for the eigenvalues of $(\mathbf{A}^T \mathbf{A})$ }
 - 3: $k \leftarrow 0$
 - 4: **repeat**
 - 5: $\mathbf{v} \leftarrow \mathbf{A}^T(\mathbf{A}\mathbf{x}^{(k)} - \mathbf{b})$
 {calculate the gradient of the projection correctness term}
 - 6: **for** each $i \in \{1, 2, \dots, n^2\}$ **do**
 - 7: $y_i^{(k+1)} \leftarrow x_i^{(k)} - \frac{v_i + \mu \cdot G_{0,\sigma}(v_i) \cdot \frac{\partial g}{\partial x_i} \big|_{\mathbf{x}=\mathbf{x}^{(k)}}}{\lambda + \mu}$
 - 8: $x_i^{k+1} \leftarrow \begin{cases} 0, & \text{if } y_i^{(k+1)} < 0, \\ y_i^{(k+1)}, & \text{if } 0 \leq y_i^{(k+1)} \leq 1, \\ 1, & \text{if } 1 < y_i^{(k+1)}. \end{cases}$
 - 9: **end for**
 - 10: $k \leftarrow k + 1$
 - 11: **until** $\|\mathbf{x}^{(k+1)} - \mathbf{x}^{(k)}\|_2^2 < \epsilon$ or $k > k_{max}$
-

The optimization process of this algorithm is based on a gradient method with an automatic weighting between the projection correctness term, and the discreteness prior. In each iteration step, the current state is moved towards the gradient descent of $\mathcal{E}(\mathbf{x})$ while weighting the $\frac{\partial g}{\partial x_i} \big|_{\mathbf{x}=\mathbf{x}^{(k)}}$ gradient step of the discretizing term based on the projection correctness. If a pixel lies on projection lines with correct projection values, then we give a bigger strength to the discreteness prior of that specific pixel. If a pixel lies on projection rays with incorrect values then its discreteness prior is weakened, or even disabled. As a consequence, we get an algorithm that aims to find a solution that satisfies the discreteness prior, but above all aims for maintaining the projection correctness. The basic concept of this algorithm is the same as of Algorithm 6, but the smoothness prior was omitted here, and we changed the discreteness prior as well.

Using the probabilistic concept of Section 4.2 and Algorithm 7, we define a method for approximating the pixel uncertainties in binary tomography. In case of binary tomography, we are looking for results satisfying the given projections

such that the result should be taken from the binary domain. Trying to find a reconstruction that has the correct projections, but in which the pixel values are the farthest away from the $\{0, 1\}$ set, we can measure how easy it is to change the pixel values. If a pixel value can easily be changed, then that pixel is evenly likely to be 0 or 1 in the final result. With this concept, we can measure the variability of pixels from only the projections, even without any prior knowledge of the original object.

By the framework of Algorithm 7 this can be done by setting a discreteness prior that discourages close-to-binary results. One such prior can be given by the function

$$g(\mathbf{x}) = \frac{1}{2} \cdot \left\| \mathbf{x} - \frac{1}{2} \mathbf{e} \right\|_2^2, \quad (4.8)$$

where \mathbf{e} stands for a vector with all n^2 positions having a value of 1.

When the least binary result \mathbf{x} is available, calculating the entropy

$$H(x_i) = -(x_i \cdot \log_2(x_i) + (1 - x_i) \cdot \log_2(1 - x_i)), \quad (4.9)$$

for each pixel value, should approximate the values of the uncertainty map.

Finally, note that – although the projection correctness term has a higher priority in the algorithm than the discreteness prior – the process uses a weighting between the two terms of the energy function, and in the end, the acquired solution is not guaranteed to strictly satisfy the projections, it rather just approximates them.

4.4 Validation of the results

For the validation of the proposed method, we performed a set of simulation experiments. We produced projection sets of the binary phantom images of Appendix C and calculated the local uncertainties belonging to the generated projection data.

We also needed another method for measuring the local uncertainties of the reconstructions to compare the proposed algorithm with. Unfortunately, we could not find any reference to such algorithms in the literature. Therefore, we have chosen to perform a random sampling of the set of possible solutions, and statistically approximate the probabilities given in (4.2).

4.4.1 Stochastic approximation of pixel uncertainties

For the random sampling of the search space, we made several reconstructions from the same projection data with a randomized reconstruction algorithm. That way

we could get random elements of the space of possible reconstructions and gain statistics on the pixel intensities.

The randomized reconstructions were performed by a Simulated Annealing based method that is the slightly modified version of the algorithm described in [68]. It performs the reconstruction by minimizing an energy function of the form

$$\mathcal{C}(\mathbf{x}) = \|\mathbf{Ax} - \mathbf{b}\|, \quad \mathbf{x} \in \{0, 1\}^{n^2} \quad (4.10)$$

with Simulated Annealing [50]. The pseudo code of this method is given in Algorithm 8.

Algorithm 8 Reconstruction algorithm based on Simulated Annealing

Input: \mathbf{A} projection matrix; \mathbf{b} expected projection values; $T_{\text{start}}, T_{\text{min}}$ starting and minimum temperatures; T_{factor} multiplicative constant for reducing temperature; $R_{\text{objective}}$ bound for stopping criteria based on the ratio of the final and starting energy function values

```

1:  $\mathbf{x} \leftarrow (0, \dots, 0)^T$  {set an initial state}
2:  $T \leftarrow T_{\text{start}}$  {set the starting temperature}
3:  $C_{\text{start}} \leftarrow C_{\text{old}} \leftarrow \|\mathbf{Ax} - \mathbf{b}\|_2^2$  {calculate the energy of the starting state}
4: repeat
5:   for  $i = 0$  to  $n^2$  do
6:      $j \leftarrow \text{Random}(\{1, \dots, n^2\})$  {choose a random position  $j$  in the vector  $\mathbf{x}$ }
7:      $\tilde{\mathbf{x}} \leftarrow \mathbf{x}$  {make a copy of the current state}
8:      $\tilde{x}_j \leftarrow (1 - x_j)$  {alter the intensity of the randomly chosen pixel}
9:      $C_{\text{new}} \leftarrow \|\mathbf{A}\tilde{\mathbf{x}} - \mathbf{b}\|_2^2$  {calculate the energy after the modification}
10:     $z \leftarrow \text{Random}([0, 1])$  {generate a random number from the  $[0, 1]$  interval with uniform distribution}
11:     $\Delta C \leftarrow (C_{\text{new}} - C_{\text{old}})$  {calculate the change of the energy}
12:    if  $\Delta C < 0$  or  $\exp(-\Delta C/T) > z$  then
13:       $\mathbf{x} \leftarrow \tilde{\mathbf{x}}$  {accept the new state with a probability based on the energy change and temperature}
14:       $C_{\text{old}} = C_{\text{new}}$ 
15:    end if
16:  end for
17:   $T \leftarrow T \cdot T_{\text{factor}}$  {lower the temperature}
18: until  $T \leq T_{\text{min}}$  or  $(C_{\text{new}}/C_{\text{start}}) \leq R_{\text{objective}}$ 

```

Due to the stochastic nature of this process, each output of Algorithm 8 is a random element of the solution space. Reconstructions better satisfying the projections will have a higher probability to be found and these probabilities should correspond to (4.2). Therefore, running this algorithm many times gives a faithful sampling of the search space, and averaging the pixel values would approximate the desired probabilities.

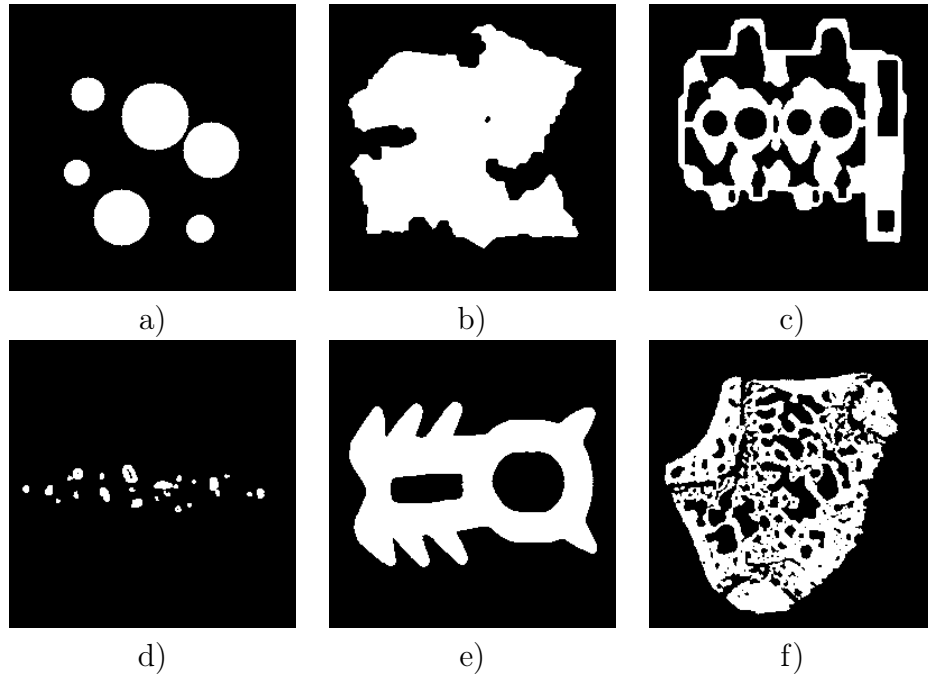


Figure 4.1: Highlighted software phantoms used for testing the uncertainty measure.

4.4.2 Test environment

In the evaluation our uncertainty measure we took 22 binary phantom images from Appendix C, produced their projection sets with different numbers of projections, and computed the pixel uncertainties with Algorithms 7 and 8. Some highlighted images can be seen in Figure 4.1.

For performing the computation, the parameters of Algorithm 7 were set empirically. We used the initial $\mathbf{x}^0 = (0.5, \dots, 0.5)^T$ vector in the beginning of the optimization, and chose the values $\mu = 1$, $\sigma = 0.25$, $\epsilon = 0.001$, and $k_{\max} = 500$. For the Simulated Annealing based method, we used the parameter settings as described in [68], except that we did not apply a smoothness regularization term in the process. More exactly, the parameter values were $T_{\text{start}} = 4.0$, $T_{\text{min}} = 10^{-14}$, $T_{\text{factor}} = 0.97$, $R_{\text{objective}} = 10^{-5}$. Moreover, for each given projection set we averaged the outputs of a 100 runs of the optimization process to approximate the probability maps explained in Section 4.2.

The implementation of Algorithm 7 was coded in C++ with GPU acceleration with the Nvidia CUDA SDK. Algorithm 8 on the other hand was not suited for parallel implementation and GPU acceleration, and it was coded in MATLAB.

For comparing the outputs of Algorithms 7 and 8, the average pixel difference was used

$$\mathcal{P}(\mathbf{x}, \mathbf{y}) = \frac{1}{n^2} \sum_{i=1}^{n^2} |x_i - y_i|, \quad (4.11)$$

that is a measure for the difference of two images \mathbf{x} and \mathbf{y} , and takes values between 0 and 1. If the two images are identical, then $\mathcal{P}(\mathbf{x}, \mathbf{y})$ takes a value of 0, and this value increases as the difference between the two images is getting more and more significant.

4.5 Results for local uncertainties

At the end of the optimization process of Algorithm 7, and after averaging 100 results of Algorithm 8, we got continuous reconstructions approximating the probability maps. A representative sample of these images is given in Figure 4.2. Second, when applying (4.9) to the pixels of the approximated probability maps, we got uncertainty maps of the reconstructions, showing for each pixel its vagueness with the given projection data. Samples of the uncertainty maps are shown in Figure 4.3.

We used the average pixel difference (4.11) to compare each probability map provided by Algorithm 7 to the corresponding probability map of Algorithm 8, and likewise for the uncertainty maps of the two methods. Some of these evaluations can be seen in Table 4.1.

The results show that there is a strong correspondence between the two types of uncertainty measures. For the pairs of probability and uncertainty maps the $\mathcal{P}(\mathbf{x}, \mathbf{y})$ values consistently showed small difference between the results of the two algorithms and took values close to 0. This is in accordance with the samples of Figure 4.2 and Figure 4.3 as the corresponding image pairs show no significant differences. Although we only showed a sample of the results, the same tendency could be observed for the rest of the test images as well.

Regarding the time requirements of the methods, the proposed algorithm took about 10-20 seconds for measuring each uncertainty map on a PC with an Intel Q9500 CPU, accelerated by an Nvidia GTX250 GPU. On the other hand, the simulated annealing based algorithm was not suitable for GPU acceleration and running it 100 times (with the same configuration) for measuring probabilities took about 2 days for each image and projection number. Thus, the entire evaluation process took several months on a cluster of computers.

As a conclusion we stress, that the proposed method is capable of acceptably approximating the local uncertainties of reconstructions in a reasonable time. One could also use the Simulated Annealing based random sampling of the space of reconstructions, but the high computation time requirement of this method makes it impractical in real applications and we also used it for validation purposes only.

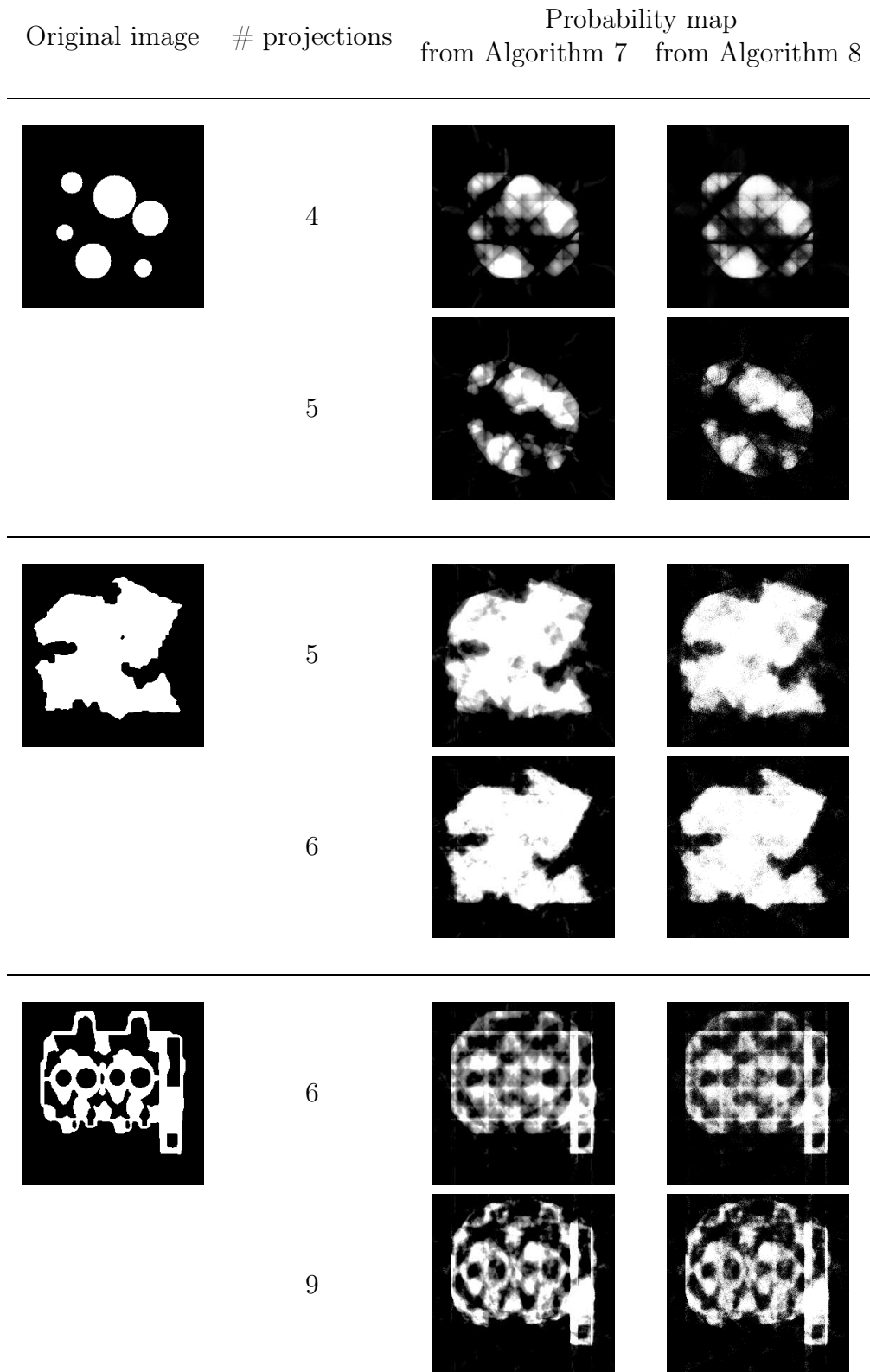


Figure 4.2: Reconstruction of images, containing pixel probabilities. White areas should with high probability take the intensity value 1, black areas are with high probability 0 in the reconstructions, while intensity values belonging to grey areas are not determined by the projections.

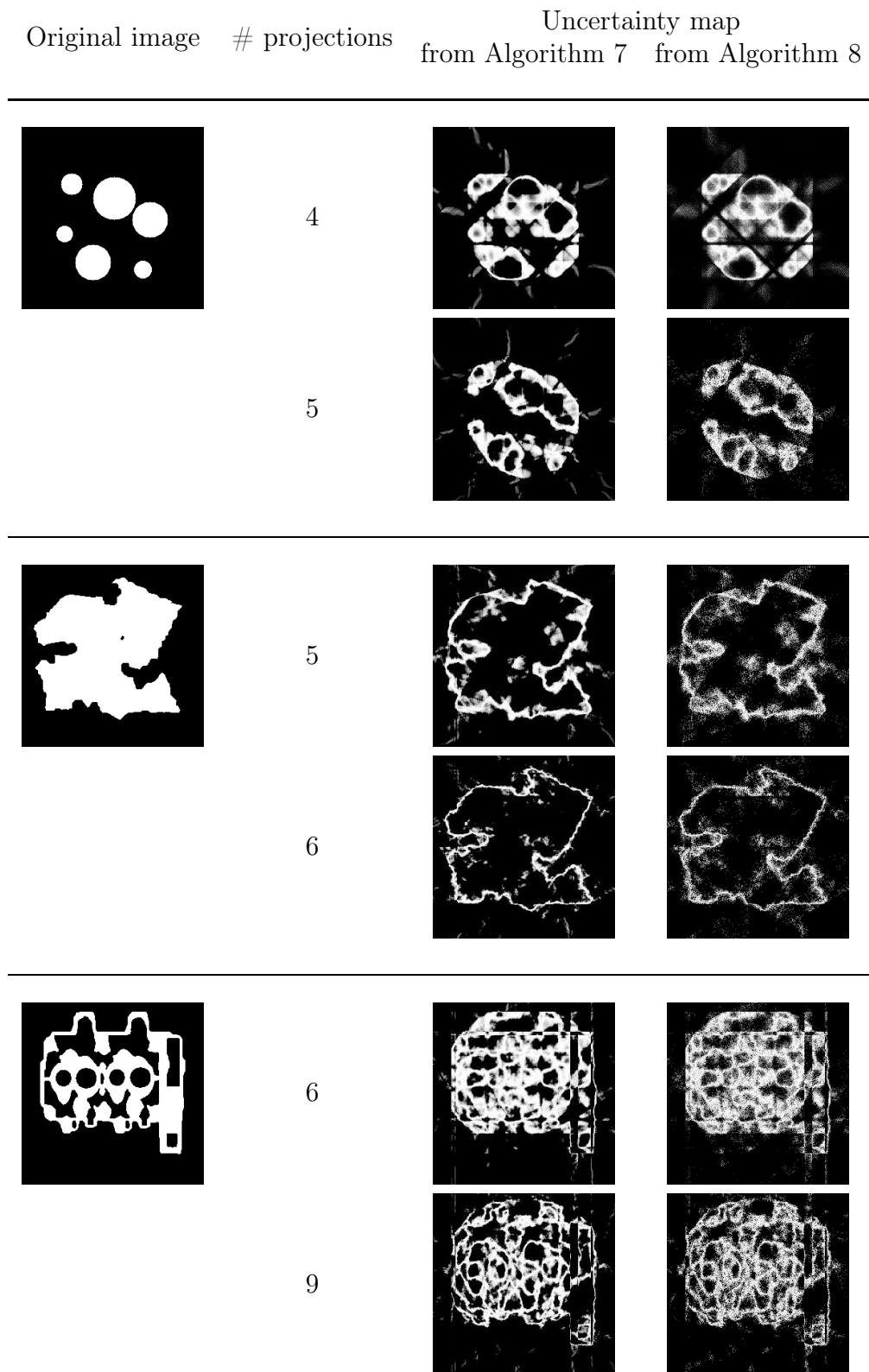


Figure 4.3: Uncertainty maps of projection sets. Dark areas are determined by the projections, while brighter areas are not, and hold uncertainty.

Table 4.1: Average pixel difference between the probability- and uncertainty- maps given by the two uncertainty measurement methods.

Difference between the probability maps						
# projs.	Fig. 4.1a	Fig. 4.1b	Fig. 4.1c	Fig. 4.1d	Fig. 4.1e	Fig. 4.1f
2	0.021	0.033	0.034	0.005	0.026	0.035
3	0.020	0.038	0.040	0.007	0.030	0.035
4	0.016	0.022	0.032	0.005	0.024	0.033
5	0.018	0.026	0.035	0.005	0.024	0.035
6	0.014	0.019	0.033	0.004	0.018	0.034
9	0.007	0.013	0.033	0.003	0.015	0.032
12	0.005	0.008	0.025	0.003	0.007	0.029
15	0.004	0.006	0.027	0.002	0.006	0.029
18	0.003	0.005	0.021	0.001	0.005	0.029

Difference between the uncertainty maps						
# projs.	Fig. 4.1a	Fig. 4.1b	Fig. 4.1c	Fig. 4.1d	Fig. 4.1e	Fig. 4.1f
2	0.038	0.088	0.069	0.017	0.047	0.057
3	0.053	0.095	0.084	0.030	0.072	0.059
4	0.046	0.065	0.073	0.017	0.059	0.064
5	0.049	0.078	0.076	0.019	0.067	0.066
6	0.046	0.066	0.082	0.015	0.061	0.069
9	0.030	0.051	0.088	0.012	0.053	0.070
12	0.022	0.040	0.080	0.013	0.033	0.071
15	0.016	0.030	0.088	0.009	0.026	0.074
18	0.013	0.021	0.076	0.007	0.020	0.077

4.6 Measuring global uncertainty of binary reconstructions

With the summation of the pixel values of the local uncertainty maps, one can also get a global description of the uncertainty of the whole reconstruction. For this purpose, we defined a formula with the normalized sum of the pixels of the uncertainty map

$$\mathcal{U}(\mathbf{x}) = \frac{\sum_{i=1}^n H(x_i)}{\frac{1}{p} \sum_{j=1}^m b_j} , \quad (4.12)$$

where p is the number of projections, and $H(x_i)$ is the uncertainty of the i -th pixel, and b_j is the j -th projection value.

This measurement takes the pixel uncertainties, adds them up, and normalizes the sum with the approximated number of non-zero values on the original image. In the ideal case the sum of the projection values for each projection would contain the number of ones in the original image. Due to the pixel-based representation

of the image, the projection data can hold rounding and representation errors, therefore we took the average of the projection value sums for the normalization.

For the validation of the global measurement we performed an experimental test by reconstructing the binary software phantoms in Appendix C from their different projection sets, and compared the accuracy of the resulted reconstructions with the global uncertainty measurement. If the global uncertainty measurement is correct, then projection sets with smaller uncertainty should lead to smaller error when an actual reconstruction is performed, and there is a connection between the uncertainty of a projection set and the actual reconstruction.

4.6.1 Compared reconstruction algorithms

In the experiments we used the TSIRT, DC, and DART algorithms to compare the global uncertainty measure with. The parameters of the reconstruction algorithms were set empirically to similar values as in the previous chapters.

In case of the TSIRT algorithm, we used the $\epsilon = 0.01$, and $k_{max} = 1000$ stopping parameters. With the DART algorithm, the continuous reconstruction were performed by 10 iterations of the SIRT, and the smoothing operation between the steps were calculated with a convolution with the kernel

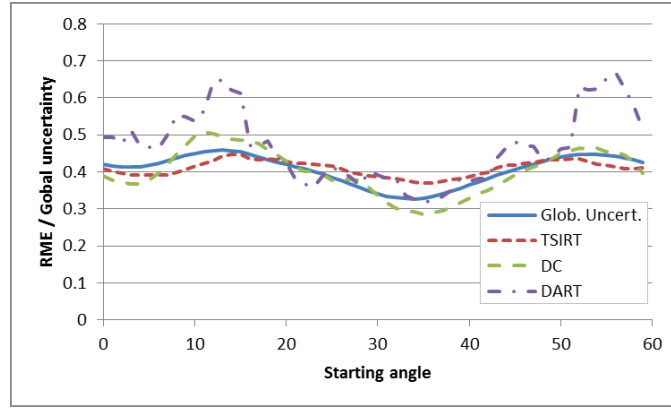
$$K = \begin{bmatrix} 1/16 & 1/16 & 1/16 \\ 1/16 & 1/2 & 1/16 \\ 1/16 & 1/16 & 1/16 \end{bmatrix},$$

and we applied the parameter values $k_{\Delta} = 10$ and $k_{max} = 500$. In case of the DC algorithm, we used the parameters $\mu_{\Delta} = 0.1$, $\gamma = 0.25$, $\epsilon_{in} = 0.1$ and $\epsilon_{out} = 0.01$.

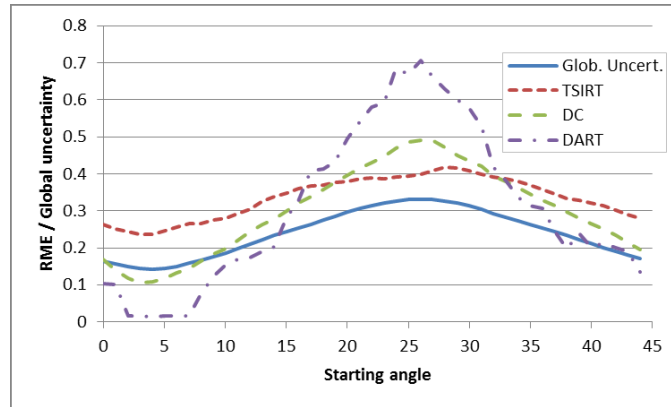
4.6.2 Test data

For each phantom image, we produced equiangular projection sets with projection numbers ranging from 2 to 18, and for each projection number we used integer starting angles between 0° and $\lceil 180^\circ/p - 1^\circ \rceil$. Similar experiments were performed in Chapter 2 to test the direction-dependency of binary tomographic reconstruction algorithms. We used these projection sets, because previous results indicated that their information content varies on a wide interval, that can be used for checking the uncertainty measure. Also, the previous works (see, Chapter 2 and [5]) showed that there is a strong correspondence between the accuracy of the reconstructed results and the information content of projections, that made this type of tests justifiable.

After performing the reconstructions with the three algorithms described above,



Results from 3 projections



Results from 4 projections

Figure 4.4: RME value, and uncertainty plots of the reconstructions of the phantom in Figure 4.1d. Each curve shows measurements for a specific algorithm, computed from projection sets with the same number of projections, but different starting angles.

we needed to measure the accuracy of the results. For this purpose, we used the Relative Mean Error (RME) measurement (1.13).

4.6.3 Results

We compared the results in different ways. First, for each projection set of the same phantom image having the same number of projections but different starting angles, we plotted diagrams that showed the reconstruction errors and uncertainty measures with respect to the change of the starting angle. The same approach was used in Chapter 2 to examine if there is a correlation between the results of different reconstruction algorithms. Some of the plots can be seen in Figure 4.4.

If there is a correspondence between the global uncertainty measure and the reconstructions, then the curves of the diagrams of Figure 4.4 should have similar slopes. The curves show that, indeed, this is the case which indicates that the

uncertainty measure is in accordance with the accuracy of the results.

With the interpretation of the results, we should also note, that the global uncertainty measure and the reconstructions provide different types of information about the projection data. The global uncertainty measure, on one hand, is an overall description of the information content of the projections which is independent of the reconstruction of the object, and can be calculated without any knowledge about the original object. Reconstruction algorithms, on the other hand, choose only one possible image among the ones satisfying the projections. This can be the original image but images differing from the original one to a high degree are also possible to be chosen, with a probability depending on the parameters of the algorithm. Therefore, a large number of reconstructions is necessary to draw a connection between the global uncertainty measure, and the *RME* value.

We also evaluated the correspondence between the results by numerical tools. We took the global uncertainty measures given for the projection sets of each phantom image, paired them up with the *RME* values of the reconstructions from the different algorithms, and calculated the $r_{\mathbf{x},\mathbf{y}}$ correlation coefficients (1.14) for the given data vector pairs. The results are summarized in Table 4.2.

Most of the entries in Table 4.2 are close to 1, which indicates that the global uncertainty measure was correct in the test cases, and describes the information content of the projections. The only outlier is Phantom 15 that the SIRT algorithm was not able to reconstruct in most cases, therefore we could not get enough data for a proper statistical analysis.

4.7 Possible applications

With the uncertainty maps, one can gain useful additional information on the projection set and the reliability of the reconstructions. This information can be used in several ways for aiding the reconstructions in practical applications of binary tomography.

4.7.1 Using the local uncertainty map in DART reconstructions

The uncertainty map and the probability map together give prior knowledge of the pixels. Pixels with a low uncertainty are well determined and their values can easily be read from the probability maps. Pixels with high uncertainty, on the other hand, are not well determined and some additional information or prior knowledge about the object is needed to reconstruct them. With this idea in mind, the uncertainty maps can be used to highlight the areas of the image that need more consideration

Table 4.2: Correlation between our Global Uncertainty (GU) measure and the accuracies of reconstruction algorithms (TSIRT, DC, DART), tested on the 22 binary phantom images of Appendix C. Each column shows correlation between the Global Uncertainty and one algorithm.

	GU↔TSIRT	GU↔DC	GU↔DART
Phantom 1	0.93	0.99	0.96
Phantom 2	0.82	0.99	0.99
Phantom 3	0.93	0.98	0.99
Phantom 4	0.89	0.99	0.98
Phantom 5	0.89	0.97	0.97
Phantom 6	0.88	0.94	0.89
Phantom 7	0.89	0.99	0.98
Phantom 8	0.93	0.98	0.95
Phantom 9	0.94	0.99	0.99
Phantom 10	0.98	0.99	0.98
Phantom 11	0.95	0.97	0.98
Phantom 12	0.98	0.91	0.88
Phantom 13	0.90	0.99	0.96
Phantom 14	0.87	0.91	0.90
Phantom 15	0.35	0.96	1.00
Phantom 16	0.96	0.94	0.90
Phantom 17	0.90	0.91	0.84
Phantom 18	0.91	0.98	0.98
Phantom 19	0.93	0.98	0.96
Phantom 20	0.89	0.95	0.94
Phantom 21	0.94	0.97	0.96
Phantom 22	0.82	0.95	0.97

in the reconstruction, and neglect parts which are precisely determined. This might be used to improve both the accuracy and speed of reconstruction algorithms.

For example, the DART algorithm (defined in Section 1.2.1) uses an iterated thresholding of continuous reconstructions, by fixing the inner pixels of the objects, and adjusting the boundaries. Coming from the concept of the algorithm, the DART has difficulties in finding small holes in large homogeneous areas of objects, or small objects in large empty areas. An improved version of the DART tries to overcome this problem by stochastic modifications [12], but the uncertainty map could also be used to highlight the problematic areas of the image, and improve the results.

Based on this argument, we implemented an uncertainty aided binary version of the DART algorithm, which also takes the local uncertainty map into account. We simply defined an extra parameter ν that will refer to a number of DART iterations. Then, in every k -th iteration of the process, we determine the set of pixel indices which have an uncertainty greater than a bound $\mathcal{U}(x_i^k) > \frac{k}{\nu}$ and do not threshold

these pixels. As a consequence, we get a method that postpones the thresholding of pixels having higher uncertainties, and as the process advances, it increases the limit on the uncertainty. Finally, after the iteration count reaches ν , the process will be equivalent with the original DART algorithm, but the previous process is likely to have found the small areas which caused difficulties. This modification itself is sufficient to gain an improved DART algorithm that does not have the weakness of the original one and can cope with small areas in the reconstruction. The detailed description of this method is given in Algorithm 9.

Algorithm 9 Binary Uncertainty aided Discrete Algebraic Reconstruction Technique (BU-DART)

Input: \mathbf{A} projection matrix; \mathbf{b} expected projection values; $\mathbf{x}^{(0)}$ initial solution; k_Δ iteration window size of the stopping criteria; k_{max} maximal iteration count; ν uncertainty threshold

- 1: Compute a starting reconstruction $\mathbf{x}^{(0)}$ using an algebraic reconstruction method
 - 2: Compute the uncertainty $H(x_i)$ of each x_i pixel based on the \mathbf{b} projection data
 - 3: $k \leftarrow 0$
 - 4: **repeat**
 - 5: $k \leftarrow k + 1$
 - 6: Compute a thresholded image $s^{(k)} = \mathcal{T}_\Phi(\mathbf{x}^{(k-1)})$
 - 7: Compute $I^{(k)}$ set of non-boundary pixels of $s^{(k)}$
 - 8: Compute $J^{(k)} = \{i \mid \mathcal{U}(x_i) > 1 - \frac{k}{\nu}\}$ index set of uncertain pixels
 - 9: **for all** $i \in \{1, \dots, n^2\}$ **do**
 - 10: $y_i^{(k)} \leftarrow \begin{cases} s_i^{(k)}, & \text{if } i \in (I^{(k)} \setminus J^{(k)}), \\ x_i^{(k-1)}, & \text{otherwise.} \end{cases}$
 - 11: **end for**
 - 12: Using $\mathbf{y}^{(k)}$ as a starting solution, compute a continuous reconstruction $\mathbf{x}^{(k)}$ while keeping the pixels in $(I^{(k)} \setminus J^{(k)})$ fixed
 - 13: Apply a smoothing operation to the pixels that are not in $(I^{(k)} \setminus J^{(k)})$
 - 14: **until** $\mathbf{s}^{(k)} = \mathbf{s}^{(k-k_\Delta)}$ or $k > k_{max}$
 - 15: **return** the segmented image $\mathcal{T}_\Phi(\mathbf{x}^{(k-1)})$
-

Some examples with this modified DART algorithm can be found in Figure 4.5, showing that using the uncertainty map really did improve the performance of the DART algorithm in the binary case.

4.7.2 Verifying the results of reconstructions

Another possible application arises from the field of non-destructive testing of objects. Here, discrete (or binary) tomography is used to determine the inner structure of industrial objects looking for defects in the material (e.g., fractures and bubbles). In this case, the uncertainty maps can be used together with the results of a binary reconstruction algorithm to check the accuracy at the critical parts

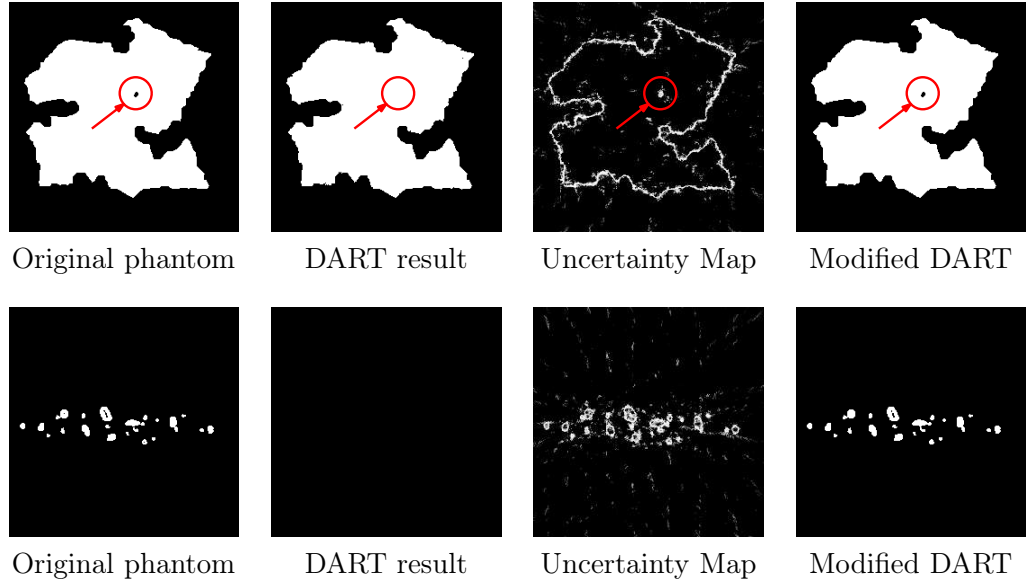


Figure 4.5: Results of the Binary Uncertainty aided DART preformed on the phantom of Figure 4.1

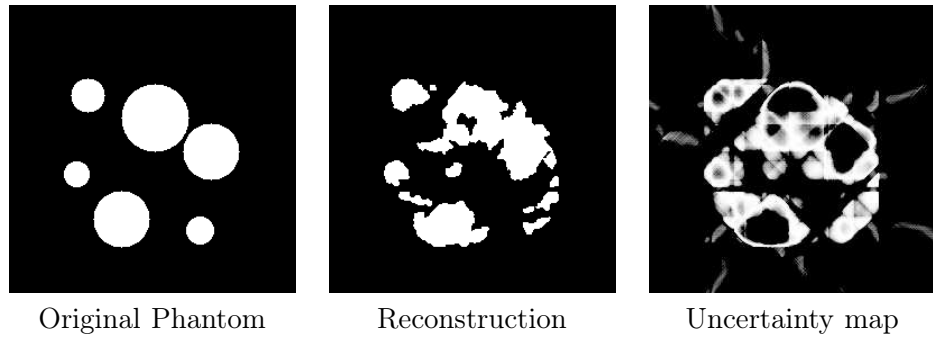


Figure 4.6: Example of a highly inaccurate reconstruction and its uncertainty map. Results indicate, that further projections are needed for the reconstruction to make a decision about the object.

of the object and rule out false detections. Also, if taking further projections is possible, the uncertainty map can show that further information is needed for the proper evaluation of the object. An example can be found in Figure 4.6.

4.7.3 Blueprint-based projection selection

In Chapter 2 we showed, that the choice of projection directions can greatly influence the accuracy of the reconstructed results. Some projection sets contain more information than others, thus one can assure more precise results by using better projection angles.

In section Section 2.5 we also proposed, that if a blueprint of the object is available, it can be used to choose the best projection directions to improve the accuracy of the results. One only has to simulate the possible projection set of the blueprint, perform reconstructions and choose the directions that lead to the best

result.

In Section 4.6 we showed, that the global uncertainty measure describes the information content of the projections, that correlates with the accuracy of the reconstructions. We also argue, that the global uncertainty measure gives a more reliable description of the set of possible reconstructions, since it gives us information on the whole search space, not only one of its elements. Therefore, it could be used for choosing the projection angles in binary tomography.

In addition, the local uncertainty measures can be summarized not only for all the pixels, but for a smaller area of the reconstructed image as well. In this way, one can get a measure of the reliability of the reconstruction at specific parts of the object of study, and maximize the accuracy at specific regions of interest.

4.8 Summary

We gave a practical description of the data uncertainty problem of binary tomography, and provided a measure, that can approximate the local and global uncertainties of the reconstructed image. Given the projections of homogeneous objects, we described a method to approximate the likelihood of each pixel of the reconstructed image to take a value of 0 or 1. With this method, one can approximate the uncertainty at each pixel, get a picture of the information content of a projection set, and measure how it determines each part of a reconstructed image.

We also provided a formula for summarizing the local, pixel-based uncertainties into a global measure, that can determine the overall quality of a given set of projections. For the evaluation of the proposed methods, we performed computed experiments on a set of phantom images.

The information on the uncertainty in a projection set can be useful in practical applications to measure the accuracy and reliability of the reconstructed results, and also to improve reconstruction methods. We also explained how this information can improve the DART reconstruction algorithm in the binary case.

The findings of this thesis were in part published in a conference proceedings [65], and are submitted as a journal paper [66].

Chapter 5

Final Conclusions

This dissertation gives a summary of the Author's research in the field of discrete tomography. The results are gathered around the examination of the information content of projections, and aim to describe different aspects of how the projection data connects to the accuracy of reconstructions.

First we have shown, that the quality of binary reconstructions can strongly rely on the choice of directions used in the projection acquisitions. We found that some projection sets have higher information content which leads to better reconstructions. We have also shown that this direction-dependency phenomenon comes from the information content of the projections and it is only slightly influenced by the applied reconstruction algorithm, or distortions of the data. Thus, it is predictable and can be exploited in the discrete reconstruction of objects for improving the accuracy of the results.

We also proposed the MLEM reconstruction algorithm for the general case of discrete tomography that solves the reconstruction problem by minimizing an energy function. We defined a function that has its minima corresponding to accurate discrete reconstructions, and designed an optimization scheme for minimizing this energy function. For the validation of the results we performed experimental tests and compared the MLEM method to other state-of-the-art reconstruction algorithms. We found that the proposed method could compete with other algorithms in both the speed of the computation, and the accuracy of the results. Furthermore, we found that it is highly robust when the projection data is affected by random noise.

Finally, with the modification of the MLEM reconstruction algorithm, we proposed a method that can approximate the local uncertainties in binary reconstructions caused by the lack of information in the projection data. With this method, one can reveal which parts of the object can be reliably reconstructed based on the given projection data, and assess the reconstructions. We also defined a formula that combines the local uncertainties of the reconstructions into one global measure

that can describe the information content of the projections. With the aid of this measure, it is possible to predict the expected error of a reconstruction from only the projection data. Finally, we validated the local, and global uncertainty measures in a variety of software tests, and proposed some of their possible applications as well.

Appendix A

Summary in English

Transmission tomography is a tool-set for reconstructing the inner structure of objects from so-called projections, which are data that can be gathered from the outside, without any destruction of the objects themselves. In transmission tomography the projection acquisition process consists of exposing the object of study to some electromagnetic or particle radiation at one side, and measuring the energy loss of the beams at different points on the other side. This data provides information on the absorption property of the object at the paths of the beams. If the projections are gathered from enough directions, one can reconstruct the material properties at different regions of the object.

In case of discrete tomography we assume, that the examined object consists of only a few materials with known absorption properties. This extra information can be used to drastically reduce the number of projections required for the reconstructions, and by this to minimize the cost or unwanted affects of the projection acquisition process. Still, there might be serious limitations in the number of projections which do not allow the acquisition of a sufficiently large projection set. In this case, the incomplete projection data can make an accurate reconstruction extremely hard to carry out.

The dissertation is a summary of the Author's research in the field of discrete tomography. The central concept of the work was to examine the information content of projections, and try to understand different aspects, of what kind of information the projection data holds, and how this information determines the discrete reconstruction of objects. This better understanding of the information content of projections is essential for developing more reliable and robust methods for discrete tomography, and can lead to entirely new approaches of the problem.

Key points of the thesis

The findings of the research can be divided into three thesis groups. Table A.1 gives the connection between the results and the publications of the Author.

In the first thesis group, I examine the direction-dependency in binary tomographic reconstructions. The results were published in two conference proceedings [59, 60], and two journal papers [61, 62].

- I/1. I designed an experimental test environment for examining the correspondence between the quality of a binary reconstruction and the choice of directions to take projections with. I have shown, that the quality of binary reconstructions strongly rely on the choice of directions used in the projection acquisitions. I found that some projection sets have higher information content leading to better reconstructions.
- I/2. I gave various projection selection strategies for improving the projection angles, and thus enhance the accuracy of the reconstruction, when a blueprint of the object is available.
- I/3. I have also shown that the direction-dependency phenomenon is caused by the different information content of the different projections and it is only slightly influenced by the choice of the reconstruction algorithm, or the distortions of the data. Based on this observation, I concluded that the direction-dependency is a predictable phenomenon that can be exploited in the non-destructive testing of objects.

In the second thesis group I give a new reconstruction algorithm for the general case of discrete tomography. The results were published in two conference proceedings [63, 64].

- II/1. I developed a new reconstruction algorithm for the general case of discrete tomography. This algorithm reformulates the reconstruction problem into the minimization of an energy function. I defined a function that has its minima corresponding to accurate discrete reconstructions, and designed a novel optimization scheme for minimizing this energy function. I validated the performance of the proposed method in experimental tests and compared it to other state-of-the-art reconstruction algorithms. I found that the proposed method could compete with other algorithms in both the speed of the computation, and the accuracy of the results. Moreover, I found that it is highly robust when the projection data is affected by random noise.

In the third thesis group, I gave measures for the local and global uncertainty in binary reconstructions. The results of this thesis were in part published in a conference proceedings [65], and are submitted as a journal paper [66].

- III/1. I provided a probability based formulation of the uncertainty of pixels in binary reconstructions, i.e., which ascertains how the projection data determines each pixel of a reconstructed image. I gave a method that is capable of approximating the local uncertainty maps of the reconstructions on an acceptable level, and validated the results in experimental studies.
- III/2. I gave a formula that can summarize the local uncertainties into a global measure, that describes the overall uncertainty in the projections and predicts the expected error of a reconstruction.
- III/3. I also described how the uncertainty measure can be used to improve the performance of the DART reconstruction algorithm, and to aid the examination processes using binary tomography.

	[59]	[60]	[61]	[62]	[63]	[64]	[65]	[66]
I/1.	•							
I/2.		•						
I/3.			•	•				
II/1.					•	•		
III/1.							•	•
III/2.								•
III/3.								•

Table A.1: The connection between the thesis points and the Author's publications.

Appendix B

Summary in Hungarian

A tomográfia egy széleskörű eszköztár tárgyak belső szerkezetének vetületekből történő nem-roncsoló vizsgálatához. A transzmissziós tomográfiában a vetületképzéshez általában a vizsgált tárgyat egy oldalról valamilyen áthatoló sugárzásnak teszik ki, és mérik a különböző irányokban áthaladó sugarak gyengülését. Az így begyűjtött adatokból következtetni lehet a tárgy adott belső pontjain elhelyezkedő anyagok elnyelődési együtthatóira, és így az anyagi jellemzőkre.

A diszkrét tomográfia területén feltesszük továbbá, hogy a vizsgált tárgy csak néhány ismert anyagból állhat. Ezzel ez előzetes információval elérhető, hogy a rekonstrukcióhoz csekély számú vetület is elegendő legyen. Bizonyos esetekben viszont így is előfordulhat, hogy a kinyerhető vetületekre vonatkozó korlátozások nem teszik lehetővé a rekonstrukcióhoz elegendő vetületi adat begyűjtését. Ilyen esetekben szükség lehet a vetületi adatok új megközelítéssel történő vizsgálatára.

Jelen értekezés a Szerző diszkrét tomográfiában végzett munkásságát foglalja össze. A kutatás fő célja a vetületi adatok információtartalmának és az adatok szerkezetének vizsgálata volt, amely véleményem szerint elengedhetetlen a rekonstrukcióban használható hatékony új technikák kifejlesztéséhez, és új területeket nyithat a kutatásban.

Az eredmények tézisszerű összefoglalása

Az értekezés eredményei három csoportba sorolhatók. Az eredmények és a kapcsolódó publikációk viszonyát a B.1 táblázat foglalja össze.

Az első téziscsoport a vetületi irányfüggőség problémájával foglalkozik a bináris rekonstrukciókban. A téziscsoport eredményei két konferencia kiadványban [59, 60], illetve két folyóirat publikációban [61, 62] jelentek meg.

I/1. Megterveztem egy keretrendszert, amellyel különböző szempontok alapján vizsgálható a kapcsolat a diszkrét rekonstrukció minősége és a rekonstruk-

cióhoz felhasznált vetületek irányai között. Megmutattam, hogy a vetületek képzéséhez felhasznált irányok megválasztása nagyban befolyásolja a rekonstrukció eredményét. Azt találtam, hogy egyes vetületek jobban rekonstruáltak eredményekhez vezetnek, mint mások.

- I/2. Több új vetületi irányválasztó stratégiát javasoltam, amelyek képesek javítani a rekonstrukcióban felhasznált vetületek irányain, amennyiben rendelkezésre áll a vizsgált tárgy egy tervrajza.
- I/3. Ugyancsak megmutattam, hogy a vetületi irányfüggőség a különböző vetületek eltérő információtartalmából fakad, és független a rekonstrukcióhoz használt algoritmus megválasztásától, illetve a vetületi adatok torzulásától, így egy kiszámítható és következetes jelenség, ami kihasználható a rekonstrukciós módszerek pontosságának javításában.

A második téziscsoportban egy új rekonstrukciós algoritmust javaslok a diszkrét tomográfia többszintű esetére. A téziscsoport eredményei két konferencia kiadványban [63, 64] jelentek meg.

- II/1. Kifejlesztettem egy rekonstrukciós algoritmust a diszkrét rekonstrukció általános esetére, amely egy energiafüggvény minimalizálásával képes tárgyak szerkezetének rekonstrukcióját elvégezni. Az algoritmus helyességét tesztekkel igazoltam azáltal, hogy a működését a szakirodalomban fellelhető rekonstrukciós módszerekkel hasonlítottam össze. A vizsgálatok alapján a javasolt algoritmus mind sebességben, mind pedig az eredmény pontosságában felveszi a versenyt a jelenleg használatos más rekonstrukciós algoritmusokkal. Az eredmények alapján ugyancsak igazolást nyert, hogy a javasolt módszer rendkívül jól viselkedik zajos vetületi adatok használata esetén.

A harmadik téziscsoport a bináris rekonstrukciók lokális és globális bizonytalanságait taglalja. Az eredmények egy része egy konferencia kiadványban [65] került publikálásra, továbbá benyújtásra került egy folyóirat cikk [66] is.

- III/1. Bevezettem egy valószínűségen alapuló módszert a bináris rekonstrukciókban eredményül kapott képpontok bizonytalanságának jellemzésére, amely megadja, hogy az egyes pixelek milyen mértékig vannak meghatározva a vetületi adatok által. Ugyancsak adtam egy módszert, amellyel a gyakorlatban is közelíteni lehet a képpont bizonytalanságokat.
- III/2. Megadtam egy formulát, amellyel a képpontokra felírt lokális bizonytalanságok összegezhetőek egy globális mértékké, amely képes előre vetíteni a rekonstrukciók várható hibáját.

III/3. Végül leírtam, hogy a bizonytalansági mértékek miképpen használhatóak fel a DART rekonstrukciós algoritmus működésének javítására, illetve a bináris tomográfiát alkalmazó vizsgálati technikák fejlesztésére.

	[59]	[60]	[61]	[62]	[63]	[64]	[65]	[66]
I/1.	•							
I/2.		•						
I/3.			•	•				
II/1.					•	•		
III/1.							•	•
III/2.								•
III/3.								•

B.1. táblázat. A tézispontok és a Szerző publikációinak kapcsolata.

Appendix C

Full database of the phantom images

The test images were gathered from different sources, and characterized different shapes. Some phantoms were used for testing reconstruction algorithms in previous studies [11, 68], and some come from the TC18 2-D image database [73]. All of the images had the same size of 256 by 256 pixels.

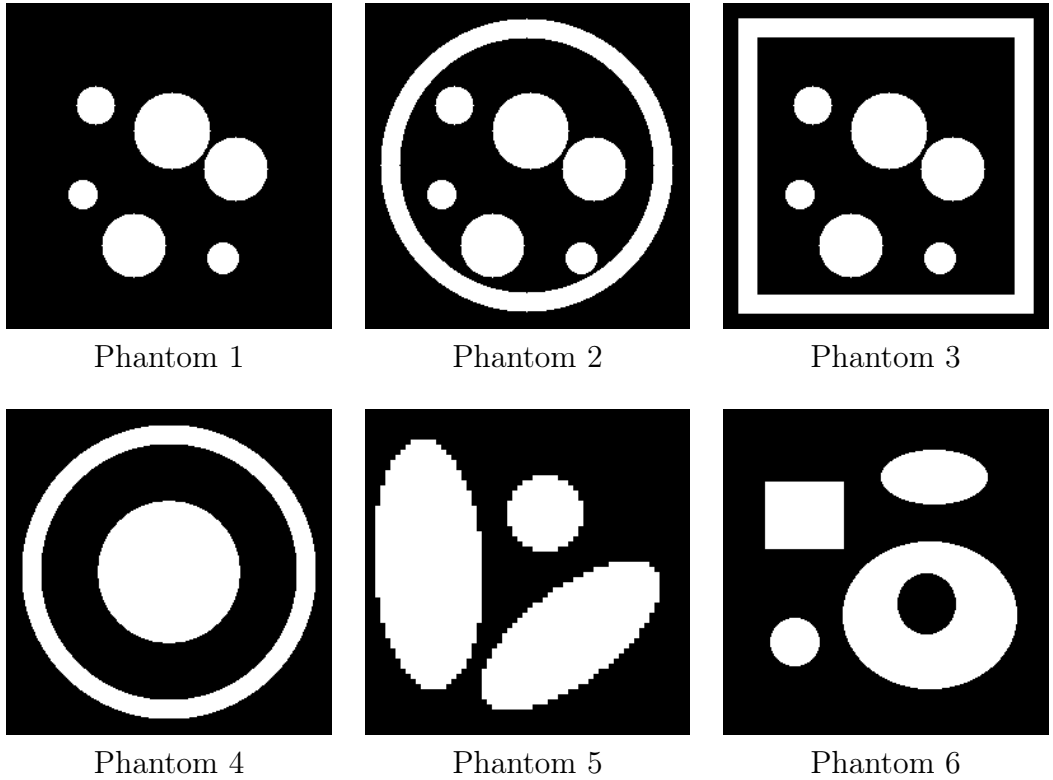


Figure C.1: Binary phantom images (part 1).



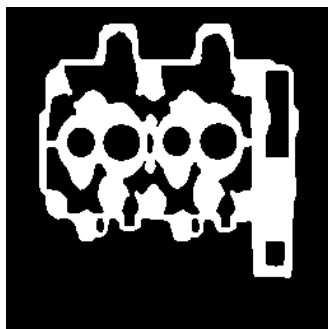
Phantom 7



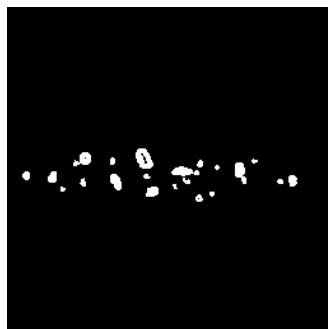
Phantom 8



Phantom 9



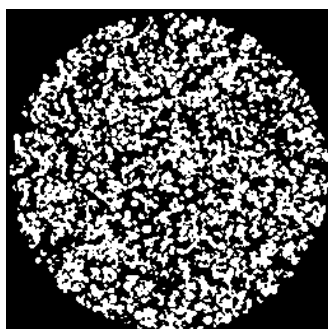
Phantom 10



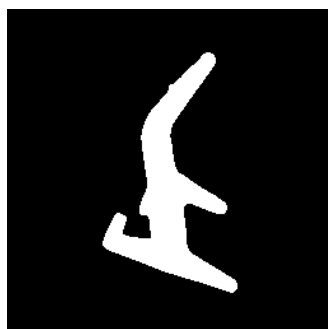
Phantom 11



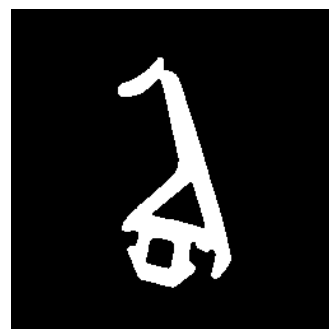
Phantom 12



Phantom 13



Phantom 14



Phantom 15



Phantom 16



Phantom 17



Phantom 18

Figure C.2: Binary phantom images (part 2).

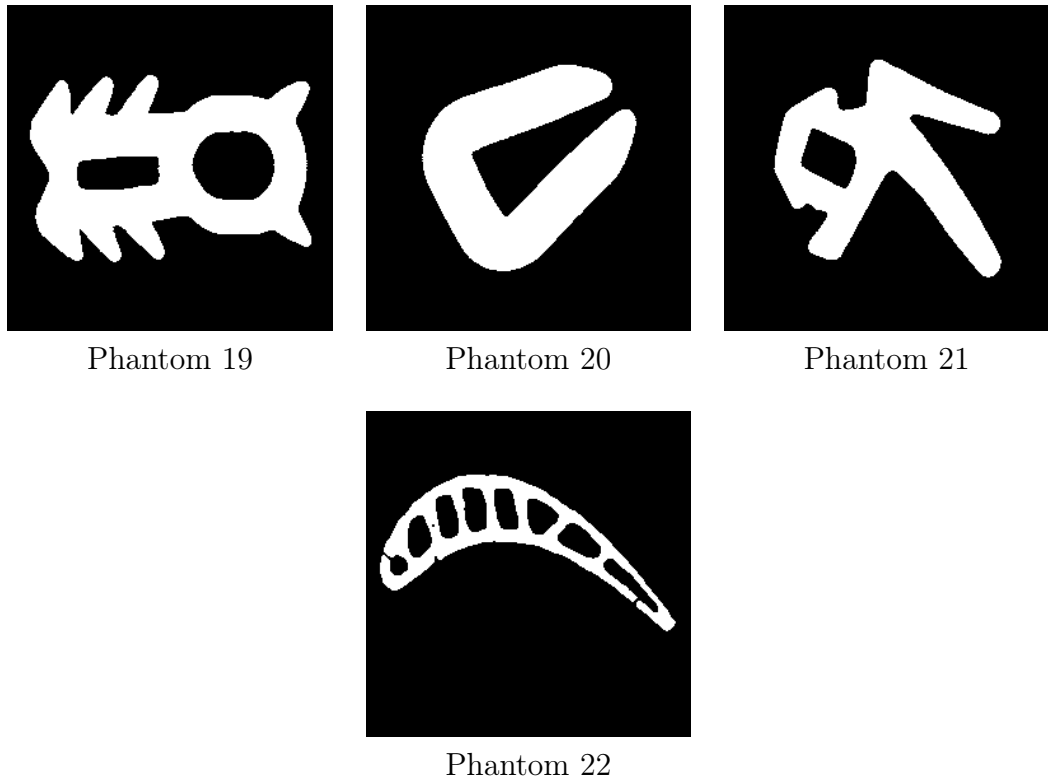


Figure C.3: Binary phantom images (part 3).

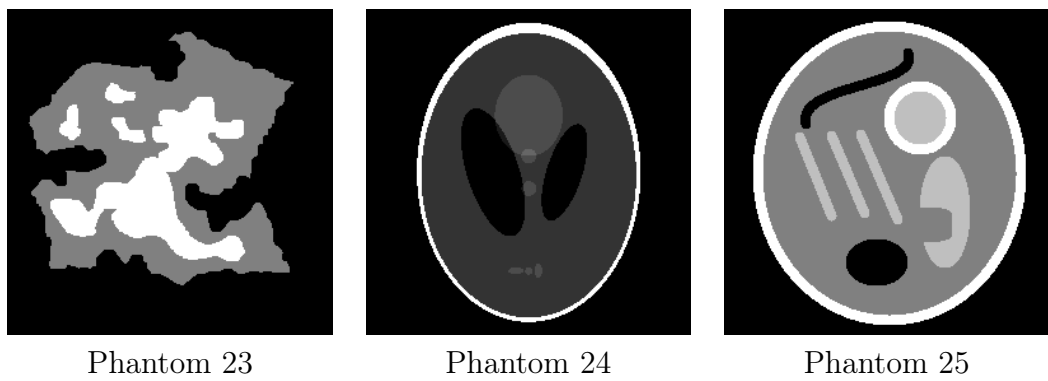


Figure C.4: Multivalued phantom images.

Bibliography

- [1] S. van Aert, K.J. Batenburg, M.D. Rossell, R. Erni, G. Van Tendeloo. *Three-dimensional atomic imaging of crystalline nanoparticles*, Nature 470, 374–377 (2011).
- [2] A. Alpers, *Instability and stability in discrete tomography*, Ph.D. thesis, Technische Universität München, Shaker Verlag, Aachen, (2003).
- [3] A.H. Andersen, A.C. Kak, *Simultaneous Algebraic Reconstruction Technique (SART): a superior implementation of the ART algorithm*, Ultrasonic Imaging, 6, 81–94 (1984).
- [4] P. Balázs, *Binary Tomography Using Geometrical Priors: Uniqueness and Reconstruction Results*, Ph.D. Thesis, University of Szeged, 2007.
- [5] P. Balázs, K.J. Batenburg, *A central reconstruction based strategy for selecting projection angles in binary tomography*, Lecture Notes in Computer Science, 7324, 382–391 (2012).
- [6] P. Balázs, M. Gara, *An evolutionary approach for object-based image reconstruction using learnt priors*, Lecture Notes in Computer Science, 5575, 520–529 (2009).
- [7] K.J. Batenburg, *An evolutionary algorithm for discrete tomography*, Disc. Appl. Math. 151, 36–54 (2005).
- [8] K.J. Batenburg, *A Network Flow Algorithm for Reconstructing Binary Images from Continuous X-rays*, Journal of Mathematical Imaging and Vision, 30(3), 231–248, (2008).
- [9] K.J. Batenburg, W. Fortes, L. Hajdu, R. Tijdeman, *Bounds on the difference between reconstructions in binary tomography*, Discrete Geometry and Computer Imaginary, LNCS 6607, 369–380 (2011).
- [10] K.J. Batenburg, W.J. Palenstijn, P. Balazs, J. Sijbers, *Dynamic angle selection in binary tomography*, Computer Vision and Image Understanding, 117(4), 306–318 (2013).

- [11] K.J. Batenburg, J. Sijbers, *DART: a fast heuristic algebraic reconstruction algorithm for discrete tomography*, IEEE Conference on Image Processing IV, 133–136 (2007).
- [12] K.J. Batenburg, J. Sijbers, *DART: a practical reconstruction algorithm for discrete tomography*, IEEE Transactions on Image Processing 20(9), 2542–2553 (2011).
- [13] K.J. Batenburg, J. Sijbers, *Optimal Threshold Selection for Tomogram Segmentation by Reprojection of the Reconstructed Image*, Computer Analysis of Images and Patterns, 12th International Conference, CAIP 2007, Proceedings (Springer-Verlag Berlin, Heidelberg), 563–570 (2007).
- [14] K.J. Batenburg, J. Sijbers, *Selection of local thresholds for tomogram segmentation by projection distance minimization*, 14th IAPR international conference on Discrete geometry for computer imagery, DGCI 2008, Proceedings (Springer-Verlag Berlin, Heidelberg), 380–391 (2008).
- [15] K.J. Batenburg, J. Sijbers, *Adaptive thresholding of tomograms by projection distance minimization*, Pattern Recognition, 42(10), 2297–2305 (2009).
- [16] J. Baumann, Z. Kiss, S. Krimmel, A. Kuba, A. Nagy, L. Rodek, B. Schillinger, J. Stephan, *Discrete Tomography Methods for Nondestructive Testing*, Chapter 14 of [35], 303–331 (2007).
- [17] S. Boyd, L. Xiao, A. Mutapcic, *Subgradient Methods*, Notes for EE392o, Stanford University, Autumn, 2003.
- [18] S. Brunetti, A. Del Lungo, F. Del Ristoro, A. Kuba, M. Nivat, *Reconstruction of 4- and 8-connected convex discrete sets from row and column projections*, Lin. Alg. Appl. 339, 37–57 (2001).
- [19] Y. Censor, *Binary steering in discrete tomography reconstruction with sequential and simultaneous iterative algorithms*, Linear Algebra and its Applications, 339(1-3), 111–124 (2001).
- [20] B. Chalmond, F. Coldefy, B. Lavayssière, *Tomographic reconstruction from non-calibrated noisy projections in non-destructive evaluation*, Inverse Problems vol. 15, 399–411 (1999).
- [21] J. Chen, A. Gao, C. Zhang, *An efficient algorithm for reconstruction of discrete sets from horizontal projections with absorption*, Communications in Computer and Information Science CCIS 307:(PART 1), 762–772 (2012).

- [22] E.K.P. Chong, S.H. Zak, *An Introduction to Optimization*, John Wiley & Sons, 2008.
- [23] M. Chrobak, C. Dürr, *Reconstructing hv-convex polyominoes from orthogonal projections*, Information Processing Letters 69(6), 283–289 (1999).
- [24] A. Daurat, *Determination of Q-Convex Sets by X-rays*, Theoretical Computer Science, 332(1-3), 19–45 (2005).
- [25] B.E. van Dalen, *Stability results for two directions in discrete tomography*, arXiv:0804.0316 [math.CO] (2008).
- [26] Y. Deng, P. Kuppusamy, J.L. Zweier, *Progressive EPR imaging with adaptive projection acquisition*, Journal of Magnetic Resonance 174, 177–187 (2005).
- [27] P. Duvauchelle, N. Freud, V. Kaftandjian, D. Babot, *A computer code to simulate X-ray imaging techniques*, Nuclear Instruments and Methods in Physics Research B 170, 245–258 (2000).
- [28] A. Frost, E. Renners, M. Hotter, J. Ostermann, *Probabilistic Evaluation of Three-Dimensional Reconstructions from X-Ray Images Spanning a Limited Angle*, SENSORS 13:(1), 137–151, (2013).
- [29] R. J. Gardner, P. Gritzmann, *Discrete tomography: Determination of finite sets by X-rays*, Trans. Amer. Math. Soc. 349(6), 2271–2295 (1997).
- [30] V. Di Gesu, G. Lo Bosco, F. Millonzi, C. Valenti, *A memetic algorithm for binary image reconstruction*, Lecture Notes in Computer Science, 4958, 384–395 (2008).
- [31] R.C. Gonzales, R.E. Woods, *Digital Image Processing, 3rd edition*, Prentice-Hall, Inc., 2008.
- [32] N. Hantos, P. Balázs, *Image Enhancement by Median Filters in Algebraic Reconstruction Methods: An Experimental Study*, Lecture Notes in Computer Science 6455, 339–348 (2010).
- [33] G.T. Herman, *Fundamentals of Computerized Tomography, Image Reconstruction from Projections*, 2nd edition, Springer-Verlag, London, 2009.
- [34] G.T. Herman, A. Kuba (Eds.), *Discrete Tomography: Foundations, Algorithms and Applications*, Birkhäuser, Boston, 1999.
- [35] G.T. Herman, A. Kuba (Eds.), *Advances in Discrete Tomography and Its Applications*, Birkhäuser, Boston, 2007.

- [36] G.T. Herman, A. Kuba., *Discrete tomography in medical imaging*, Proceedings of the IEEE, 91(2), 1612–1626 (2003).
- [37] G.T. Herman, A. Lent, P.H. Lutz, *Relaxation methods for image reconstruction*, Communications of the ACM, 21(2), 152–158 (1978).
- [38] R. Horst, N.V. Thoai, *DC Programming: Overview*, Journal of Optimization Theory and Applications, 103(1), 1–43 (1999).
- [39] A. C. Kak, M. Slaney, *Principles of Computerized Tomographic Imaging*, IEEE Press, New York, 1999.
- [40] S. Kimmel, J. Baumann, Z. Kiss, A. Kuba, A. Nagy, J. Stephan, *Discrete tomography for reconstruction from limited view angles in non-destructive testing*, Electronic Notes in Discrete Mathematics, 20 455–474 (2005).
- [41] Z. Kiss, *A Pixel-based Discrete Tomographic Technique and Its Applications*, Ph.D. Thesis, University of Szeged, 2003.
- [42] A. Kuba, *The reconstruction of two-directionally connected binary patterns from their two orthogonal projections*, Computer Vision, Graphics, and Image Processing, 27(3), 249–265 (1984).
- [43] A. Kuba, G.T. Herman, S. Matej, A. Todd-Pokropek: *Medical applications of discrete tomography*, Discrete Mathematical Problems with Medical Applications, DIMACS Series in Discrete Mathematics and Theoretical Computer Science, AMS, 55, 195–208 (2000).
- [44] T. Lukić, *Discrete tomography reconstruction based on the multi-well potential*, Lecture Notes in Computer Science 6636, 335–345 (2011).
- [45] T. Lukić, A. Lukity, L. Gogolák, *Binary Tomography Reconstruction Method with Perimeter Preserving Regularization*, 8th Conference of the Hungarian Association for Image Processing and Pattern Recognition, proceedings 83–91 (2011).
- [46] T. Lukić, B. Nagy, *Energy-minimization based discrete tomography reconstruction method for images on triangular grid*, Lecture Notes in Computer Science vol. 7655, pp. 274–284 (2012).
- [47] S. Maar, K.J. Batenburg, J. Sijbers *Experiences with Cell-BE and GPU for Tomography*, 9th International Workshop on Embedded Computer Systems: Architectures, Modelling, and Simulation, Proceedings (Springer-Verlag Berlin, Heidelberg) 298–307 (2009).

- [48] F.J. Maestre-Deusto, G. Scavello, J. Pizarro, P.L. Galindo, *ADART: an adaptive algebraic reconstruction algorithm for discrete tomography*, IEEE Transactions on Image Processing 20(8), 2146–2152 (2011).
- [49] N.D.A. Mascarenhas, C.A.N. Santos, P.E. Cruvinel, *Transmission tomography under Poisson noise using the Anscombe transformation and Wiener filtering of the projections*, Nuclear Instruments and Methods in Physics Research A 423 265–271 (1999).
- [50] N. Metropolis, A. Rosenbluth, M. Rosenbluth, A. Teller, E. Teller, *Equation of state calculation by fast computing machines*, J. Chem. Phys. 21, 1087–1092 (1953).
- [51] P. Balázs, *Diszkrét tomográfiai és PACS képfeldolgozó rendszerek*, Ph.D. Thesis, University of Szeged, 2006.
- [52] A. Nagy, A. Kuba, *Reconstruction of binary matrices from fan-beam projections*, Acta Cybernetica, 17(2), 359–385 (2005).
- [53] L. Plantagie, W. J. Palenstijn, J. Sijbers, K.J. Batenburg, *Spatial Variations in Reconstruction Methods for CT*, The Second International Conference on Image Formation in X-Ray Computed Tomography (CT Meeting), 170–173 (2012).
- [54] J.L. Rodgers, W.A. Nicewander, *Thirteen ways to look at the correlation coefficient*, The American Statistician, 42(1), 59–60 (1988).
- [55] T. Schüle, C. Schnörr, S. Weber, J. Hornegger, *Discrete tomography by convex-concave regularization and D.C. programming*, Discrete Applied Mathematics 151, 229–243 (2005).
- [56] T. Schüle, S. Weber, C. Schnörr, *Adaptive reconstruction of discrete-valued objects from few projections*, Electronic Notes in Discrete Mathematics 20, 365–384 (2005).
- [57] J. Ramperta, J.J. Veque, *Simultaneous Iterative Reconstruction Technique: Physical Interpretation Based on the Generalized Least Squares Solution*, Journal of Geophysical Research 95.(B8), 12,553–12,559 (1990).
- [58] T. Strohmer, R. Vershynin, *A randomized Kaczmarz algorithm with exponential convergence*, arXiv:math/0702226v1 [math.NA] 8 Feb 2007.
- [59] L. Varga, P. Balázs, A. Nagy, *Direction-Dependency of a Binary Tomographic Reconstruction Algorithm*, Lecture Notes in Computer Science 6026, 242–253 (2010).

- [60] L. Varga, P. Balázs, A. Nagy, *Projection Selection Algorithms for Discrete Tomography*, Lecture Notes in Computer Science 6474, 390–401 (2010).
- [61] L. Varga, P. Balázs, A. Nagy, *Projection Selection Dependency in Binary Tomography*, Acta Cybernetica, 20:167-187 (2011).
- [62] L. Varga, P. Balázs, A. Nagy, *Direction-Dependency of Binary Tomographic Reconstruction Algorithms*, Graphical Models 73(6), 365–375 (2011).
- [63] L. Varga, P. Balázs, A. Nagy, *An energy minimization reconstruction algorithm for multivalued discrete tomography*, 3rd International Symposium on Computational Modelling of Objects Represented in Images, Rome, Italy, Proceedings (Taylor & Francis) 179–185 (2012).
- [64] L. Varga, P. Balázs, A. Nagy, *Gradiens módszerek automatikus súlyozásán alapuló diszkrét tomográfiai eljárás*, A Képfeldolgozók és Alakfelismerők Társaságának 9. országos konferenciája - KÉPAF 2013, 210–223, (2013).
- [65] L. Varga, L.G. Nyúl, A. Nagy, P. Balázs, *Local uncertainty in binary tomographic reconstruction*, Proceedings of the 10th IASTED International Conference on Signal Processing, Pattern Recognition and Applications (2013).
- [66] L. Varga, L.G. Nyúl, A. Nagy, P. Balázs, *Local and global uncertainty in binary tomographic reconstruction*, Submitted to IEEE Transactions on Image Processing.
- [67] S. Weber, *Discrete tomography by convex concave regularization using linear and quadratic optimization*, PhD thesis, Heidelberg University, 2009.
- [68] S. Weber, A. Nagy, T. Schüle, C. Schnörr, A. Kuba, *A Benchmark Evaluation of Large-Scale Optimization Approaches to Binary Tomography*, Lecture Notes in Computer Science, vol. 4245, (2006), 146–156.
- [69] *Algorithms for Reconstruction with Nondiffracting Sources*, Chapter 3 of [39].
- [70] *Algebraic reconstruction algorithms*, Chapter 7 of [39].
- [71] *Algebraic Reconstruction Techniques*, Chapter 11 of [33].
- [72] NVIDIA CUDA technology, web page (May 2013)
<https://developer.nvidia.com/category/zone/cuda-zone>
- [73] IAPR Technical Committee on DISCRETE GEOMETRY (TC18), 2-D image database, (May 2013)
http://www.tc18.org/code_data_set/2D_images.html

Index

- Algebraic Reconstruction Method, 11
- ARM, 11
- correlation coefficient, 15
- direction-dependency, 17
- map
 - probability, 60
 - uncertainty, 60
- NDT, 41
- non-destructive testing, 41
- Pearson's correlation coefficient, 15
- projection, 1
- projection correctness term, 12
- projection selection strategy
 - AltAng, 21
 - EquiAng-B, 19
 - EquiAng-W, 19
 - Greedy, 19
- Radon-transform, 5
- reconstruction, 5
 - binary, 9
 - continuous, 8
 - discrete, 8
- reconstruction algorithm
 - DART, 10
 - DC, 13
 - MLEM, 48
 - SIRT, 11
 - TSIRT, 11
- relative mean error, 14
- RME, 14
- SA, 20
- Simulated Annealing, 20
- thresholding, 10
- tomography, 1
 - binary, 1, 8
 - discrete, 1, 8
 - In-Situ, 43
 - transmission, 1